SECONDA UNIVERSITÀ DEGLI STUDI DI NAPOLI

DOTTORATO DI RICERCA REGIONALE

IN

INGEGNERIA GEOTECNICA

XXVI CICLO

ANALYSIS OF INSTALLATION AND LOADING PROCESS FOR DISPLACEMENT PILES BY DISCRETE ELEMENT MODEL

Francesca Valentino

Tutor: prof. ing. **Alessandro Mandolini**
Co-Tutor: prof. ing. **Francesco Calvetti**

Marzo 2014

To Luigi and Marina

CONTENTS

LIST OF SYMBOLS

Latin

A_b	*pile cross sectional area*
A_f	*auger flight area*
d_{min}, d_{max}, d_{av}, d_{av}^*	*minimum, maximum, mean, scaled particle diameter*
d_c	*cone diameter*
d_p	*pile diameter*
D_c	*chamber diameter*
D_{MS}	*measurement sphere diameter*
D_R, D_{Rop}	*relative density, operative relative density*
e_{min}, e_{max}	*minimum and maximum void index*
E_{INS}, E_{EX}	*insertion, extraction energy*
F_{INS}, F_{EX}	*insertion, extraction force*
G	*amplification factor for penetration rate*
h	*distance of pile section from the base*
H_c	*chamber height*
K_L	*earth pressure coefficient after loading*
$K_{L,av}$	*average earth pressure coefficient after loading*
$k_{0,p}$	*earth pressure coefficient at rest*
k_N, k_S	*normal and tangential contact stiffness*
L_p	*pile length*
L	*FDP tool length*
n, n_{min}, n_{max}, n_0, n_{input}	*generic, minimum, maximum, initial porosity*
$n_{0,MS}$, n_{input}	*initial measured, input porosity*
n_H	*influence distance from chamber bottom on pile diameter*
n_p	*pile diameter on particle diameter*

N	*normal force*
$N_{q,INS}$	*end-bearing capacity factor during insertion*
$N_{q,L}$	*end-bearing capacity factor after loading*
p, p_0	*mean stress, initial mean stress*
p_{INS}, $p_{x,INS}$, $p_{y,INS}$	*generic, in plane (x,z), in plane (y,z) insertion mean stress*
p_{EC}, $p_{x,EC}$, $p_{y,EC}$	*generic, in plane (x,z), in plane (y,z) end of construction mean stress*
p_{atm}	*atmospheric pressure*
q	*deviatoric stress*
q_b	*unit base resistance*
$q_{b,d}$	*unit base resistance of disk shaped pile*
$q_{b,c}$	*unit base resistance of conical shaped pile*
$q_{b,INS}$, $q_{b,L}$	*unit base resistance during insertion and loading*
q_c	*cone resistance*
$q_{c,av}$, q_c^*, $q_{c,UNCOR}$	*average, calculated, uncorrected cone resistance*
Q_{lim}	*pile bearing capacity*
R	*pile radius*
r	*radial distance from pile axis*
R_c	*chamber radius*
R_{dMIN}, R_d	*minimum, chamber diameter on pile diameter*
T_{INS}, T_{EX}	*insertion, extraction torque*
v	*cone penetration rate*
v_{INS}, v_{EX}	*insertion, extraction pile rate*
z_G	*depth of pile sections barycentre*
z_{max}	*maximum height of assembly*

Greek

α_b	*pile unit base resistance on cone unit resistance*
α_c	*correction factor of base shape*
ε_v, ε_z	*volumetric, deviatoric strain*

μ, μ_w	*interparticle, wall/particle friction coefficient*
σ_{conc}	*concrete pressure*
σ'_1, σ'_3	*maximum, minimum principal stress*
σ_{v0}, σ_{h0}	*geostatic vertical, horizontal stress*
$\sigma_{v0,t}$, $\sigma_{h0,t}$	*theoretical geostatic vertical, horizontal stress*
$\sigma_{v0,MS}$, $\sigma_{h0,MS}$	*measured geostatic vertical, horizontal stress*
$\sigma_{h,INS}$	*horizontal stress during insertion*
$\sigma_{h,L}$	*horizontal stress after loading*
τ, τ_{max}	*shaft, maximum shaft stress*
φ_{cv}	*constant volume friction angle*
φ_{μ}	*interparticle friction angle*
ω_{INS}, ω_{EX}	*insertion, extraction angular velocity*

INTRODUCTION

Background and motivations

In spite of significant advances in understanding mechanisms that determine the shaft friction and end-bearing capacity of different types of pile, design methods still heavily rely on empirical correlations.

The development of new piling equipments and perforation tools undoubtedly takes place at a speed higher than the capability of implementing rational approaches to understand what really happens into the soil during the construction of a pile. It follows that the most challenging aspect of pile design is, therefore, the need to select proper values for design parameters from an experimental database, which is often limited and not necessarily including the specific type of pile under consideration.

This viewpoint is valid if referring to either replacement (bored, CFA) piles or displacement (driven, jacked, screwed) piles, and again when installed either in fine grained (clay, silt) soils or coarse grained (sand, gravel) soils.

Over the last decades, a massive number of researches was carried out on the topic. Reference can be made to a number of relatively recent authoritative and comprehensive reports (Randolph, 1994, 2003; Poulos *et al*., 2001; Mandolini, 2003; Mandolini *et al*., 2005; Randolph *et al*., 2005). In all these reports is strongly marked that static load tests on piles is still the most reliable design method of a pile, revealing so, indirectly, that the rational ones are far to be exhaustive.

As a matter of fact, most of the present insights into the behaviour of piles and the most significant progresses in analysis and design have been obtained by collecting and interpreting load tests data.

Experimental results, like those reported by Holeyman and Charue (2003), Jardine *et al*. (2005) and Viana da Fonseca and Santos (2008), help understand the different pile response to axial loading. The same contribute is given by the systematic collection of experimental data, like those initially provided by Bustamante and Gianeselli (1982) or, more recently, by Mandolini *et al*. (2005) to the technical and scientific community.

As for the latter, they report the results, in term of the ultimate axial load capacity Q_{ult}, as measured by 20 static load tests to failure (conventionally evaluated at a pile head settlement w = 10%d_p, where d_p is pile diameter) carried out on different piles in relatively uniform subsoil conditions, like those encountered in the eastern Naples area. The results are summarised in Table 1 in terms of the ratio Q_{ult}/W_p, where W_p is the weight of the pile.

As it can be noticed, replacement (bored) piles gave the smallest value of Q_{ult}/W_p (about 12) and the largest scatter (COV = 26%); on the contrary, displacement (driven) piles gave the largest value of Q_{ult}/W_p (about 73) and the smaller scatter (COV = 8%); as expected, replacement (CFA) piles exhibited an intermediate behaviour.

Pile type	Q_{ult}/W_p [-]	COV(Q_{ult}/W_p) [%]
Replacement (bored)	12.1	26
Replacement (CFA)	37.5	25
Displacement (driven)	73.1	8

Table 1. Summary of static load tests reported by Mandolini *et al.* (2005)

These results are particularly useful for assessing, from a qualitatively point of view, the effects of pile technology for given subsoil conditions: for a pile with a given weight, the ultimate axial load capacity can vary on the average up to six times (73.1:12.1) when displacing instead of replacing soil during installation. There is no need to say that specific values can have some practical significance only for the eastern Naples area, but certainly cannot be used for different subsoil conditions.

The same does not apply to axial soil-pile stiffness. In the same paper, Mandolini *et al.* (2005) report the results of 125 axial load test results, demonstrating that pile technology has a less critical influence on pile response under axial loads far from failure.

According to Randolph (1994) and Mandolini (2003), it can be theoretically explained by considering that pile head settlement is due to the strains developing in a large soil mass extending over a distance of the order of the pile length or more. In details, the soil changes, induced by the specific installation procedure adopted for a pile, are essentially concentrated in a thin cylinder close to the pile shaft and at pile base, thus strongly affecting the response in terms of unit shaft friction and unit base resistance. Then, these are integrated over the respective areas, in order to give the ultimate axial load capacity of the pile. The incidence of these “disturbed” volume of soil, extending no more than 2-3 pile diameter for the pile shaft (Van Weele, 1988; Viggiani,

1993), is negligible if compared with that contributing to pile head settlement (as already stated, of the order of the pile length or more). It follows that pile head settlement under axial load far from failure can be reasonably evaluated by adopting approaches (linear elastic, based on the small strain stiffness of the soil; equivalent or secant linear elastic, based on an "operative" soil stiffness) not taking into account pile technology.

Under these premises, it seems quite clear that advances are needed, in order to rationally understand how much resistance (and not stiffness) the soil makes available at soil-pile interface (along the shaft an at the base) after the installation of a pile.

Objectives

Within the framework of a research agreement among the Department of Civil Engineering, Design, Building and Environment at the Second University of Naples, from one side, and Icotekne s.p.a. (Italian piling company) and Bauer-Italia s.r.l (Italian branch of the Bauer Maschinen Group, one of the worldwide leading company for, among others, piling equipment), on the other side, it was established to improve knowledge about the soil state changes (porosity, stress) induced by the installation of screwed displacement piles and to possibly quantify related consequences in terms of pile response to axial loading.

The present work may be considered as only an initial step of a still in progress research, whose the main challenges are:

- Understanding the capability (either in terms of modelling or in terms of type and size of boundary value problem) of the Distinct Element Method (DEM) to study the installation of an object into a soil particulate system.

- Taking advantage of the similarities between the cone penetrometer and closed-end jacked piles, to validate the numerical tools and constitutive models against CPT data.

- Carrying out a parametric study regarding the installation and subsequent axial loading of closed-end jacked piles in different soils.

- Comparing these results with those obtained with reference to the installation and subsequent axial loading of screwed piles in the same soils.

- Sketching some overall index to directly compare the response of different piles in terms not only of load carrying capacity but also of power used to install them.

- The work is limited to dry sandy soil because of its capability to suffer important volumetric changes during the installation of the pile giving, thus, rise to the largest expected soil state changes after installation. Saturated soils have been excluded from the study, in order to not consider pore pressure changes during the installation of the piles.

Structure of the Thesis

The Thesis consists of five chapters.

Chapter 1 presents a review on the current understanding of pile behaviour in granular cohesion-less soils. Therefore, this literature review focuses on two main aspects: the current design methods both for displacement and non displacement piles; installation effects.

Chapter 2 describes the theoretical basis of the Distinct Element Method, with particular reference to the mechanics of the contacts among the particles and the available options in terms of constitutive models.

Chapter 3 summarizes all the studies carried out with the aim to get a reasonable compromise between computational efforts and reliability of the numerical solution. Some pioneering research works (dealing with problem like laboratory tests on soil specimens or calibration chamber tests) are recalled and used as starting point to confirm and to broad knowledge about the rules to follow for different boundary value problems (in geometry and size).

The core of this Thesis is presented in *Chapter 4*. Herein, the results of all the numerical analyses, carried out with reference to closed-end jacked piles and screwed piles, are reported. The most important findings obtained during and at the end of the pile installation process, as well as after the loading, are illustrated, commented and compared with the established knowledge on the subject.

Conclusions hailing from the present work and recommendations for future research are presented in *Chapter 5*.

CHAPTER 1. LITERATURE REVIEW

1.1. Introduction

The ultimate axial load capacity of a pile can be estimated by summation of the ultimate shaft capacity, Q_s, and the ultimate base capacity, Q_b. The weight W_p of the pile is subtracted for the compressive load capacity and added for the uplift load capacity. Depending on the case under examination:

$$Q = Q_b + Q_s \pm W_p = A_b q_b + A_s \bar{q_s} \pm W_p \quad (1.1.1)$$

where A_b and A_s are the base and the shaft area of the pile, respectively, while q_b and $\bar{q_s}$ are the unit base and average shaft resistance.

For conventional replacement piles in sands, if gross errors can be excluded during execution and high fluidity concrete is then placed, very often is supposed that concreting reinstates the effective stress state existing before drilling along shaft (Fleming *et al*., 2009). As well known, the pre-existing stress state into the soil is one of the major challenge in Soil Mechanics, since it is strictly related to all the uncertainties lying in a reliable estimation of the geostatic effective horizontal stresses, commonly related to the effective geostatic vertical stresses by the earth-pressure coefficient at rest $k_0 = \sigma'_{h0}/\sigma'_{v0}$.

For displacement piles in sands, more complexities arise from the inevitably significant changes in the soil state which occur during the installation. According to Randolph (2003), as the pile is inserted, the soil immediately adjacent to the pile will undergo severe distortion and changes to the fabric, with a certain degree of disturbance. The soil outside the immediate vicinity of the pile will be displaced outwards, with a strain field that resembles spherical cavity expansion ahead of the pile tip, merging to cylindrical cavity expansion along the pile shaft (Figure 1.1.1).

An incontrovertible evidence of such changes is reported in Figure 1.1.2, where the results of CPT tests performed before and after the installation of an Atlas screw pile into granular soil (De Cock and Imbo, 1994) are presented.

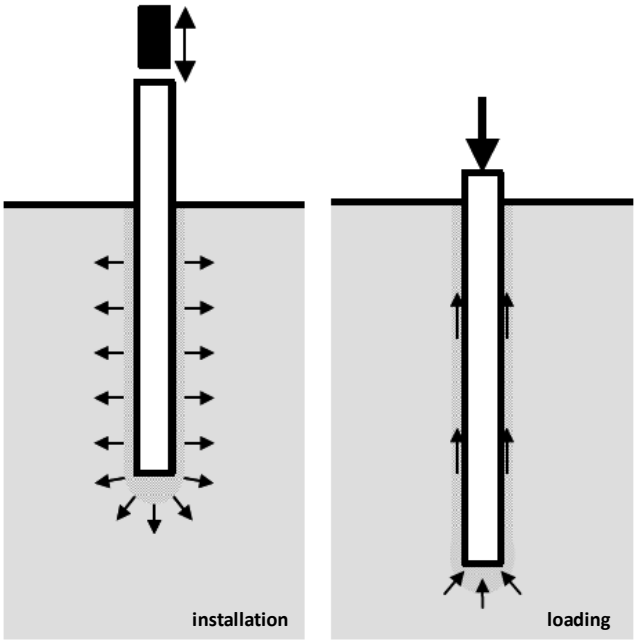

Figure 1.1.1. Main phases during history of a prefabricated displacement pile

It is evident that the q_c values measured by the CPT executed after the installation are larger than those measured before installation with the only exception for the upper 2 meters.

A detailed picture of the complex phenomena developing during the insertion of a jacked displacement pile is given by Basu *et al*. (2010).

Figure 1.1.3 shows schematically the different stages involved in the installation of a jacked pile. Stage 1 corresponds to the penetration of the pile in a virgin soil mass and is modelled as a combination of two distinct phases: the cavity expansion phase and the 'primary shearing' phase.

The first phase (i.e. cavity expansion) represents the creation of a cylindrical space (occupied by the pile) within the ground as the pile tip pushes the soil away from the path of the pile.

The base area is either a conical tip fit to the pile or the 'rigid' tapered cone predicted by bearing capacity theory in the case of a rough base. The soil in the 'rigid' tapered cone is in a nearly elastic state. A 'rigid' tapered wedge is also observed in the model pile tests by White and Bolton (2004).

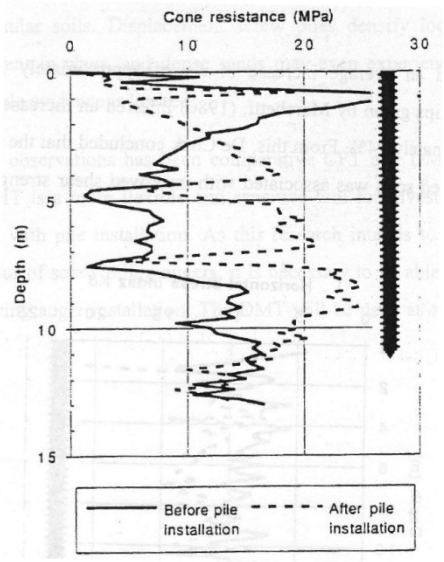

Figure 1.1.2. CPTs before and after screw pile installation (De Cock and Imbo, 1994)

The cylindrical cavity expansion stops when the cavity radius becomes equal to the pile radius, i.e. as the shoulder (base) of the cone clears element 'A' (Figure 1.1.3a). The cavity expansion phase is followed by vertical shearing along the shaft wall (primary shearing phase) until limit (critical-state) shear stress is reached along the pile shaft. Actually, a certain amount of vertical shearing may also be associated with the cavity expansion phase.

Stage 2 represents the removal of the jacking load. This occurs either after the maximum jacking-stroke length s of the hydraulic jack is reached or at the end of installation. During the unloading stage, the shear stress reduces until it reaches a residual value and the normal stress acting on the pile shaft reduces due to contraction of the soil elements in its vicinity (Figure 1.1.3b).

The magnitude and direction of the residual shear stress τ_{res}, acting on the shaft of a displacement pile installed in sand, vary with depth and depend on many factors, such as relative pile–soil stiffness, pile geometry and base-to-shaft load ratio (Briaud and Tucker, 1984; Darrag and Lovell, 1986). Field and laboratory test results on model jacked piles (Lehane *et al*., 1993; Colombi, 2005) show that τ_{res} is negative (acting downward) in the upper part of the pile and positive (acting upward) near the bottom of the pile, whereas in some portion of the pile it is equal to zero.

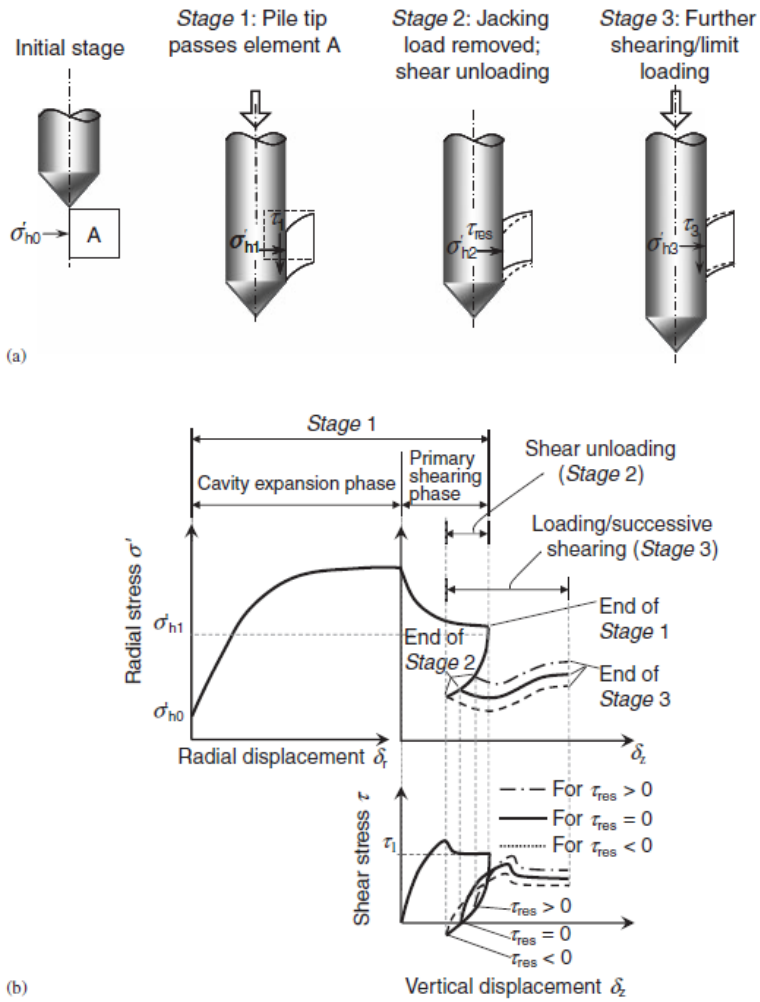

Figure 1.1.3. Installation of jacked piles: (a) analysis stages and (b) evolution of normal and shear stresses for an *uncoupled* analysis with negative, zero and positive residual shear stresses.

During Stage 3 the load is reapplied to the pile, until a limit condition is reached, once again. For a pile installed monotonically, Stage 3 represents the application of the structural load (or the performance of a static pile load test). For typical jacked piles, which are installed with multiple strokes, Stage 3 represents the second jacking stroke. Subsequent jacking strokes are represented by successive repetition of Stages 2 and 3 (multiple removals and

re-applications of the jacking load at the pile head). At each load increment reversal, there is a renewed phase of soil contraction in the vicinity of the pile, which results in a net loss of confining stress, and, consequently, reduction in unit limit shaft resistance (friction fatigue). The last reloading stage always corresponds to the application of the load from the superstructure (or the load applied during a field load test).

From all these considerations it is quite evident how the problem under study is very complex.

To overcome the difficulties, a massive number of researchers have suggested a number of rules for estimating end-bearing resistance and shaft resistance, depending on the combination of pile type and soil type. Reference can be done to a number of well known textbooks (e.g.: Poulos, 1980; Tomlison, 2004; Fleming *et al*., 2009; Viggiani *et al*. 2011) or comprehensive papers or manuals (e.g.: Poulos, 1989; Jardine *et al*., 2005; Mandolini *et al*., 2005; FHWA, 2010).

On the overall, it can be said that the design methods currently available can be divided into two broad categories: those based on fundamental soil parameters (friction angle, relative density and stiffness) or those based on the results of in situ tests (the most common are the cone penetration test CPT and the standard penetration test SPT). As for the latter, due to the similarities among cone penetrometer and pile the use of CPT results is largely preferred for the prediction of the ultimate axial capacity of displacement piles.

1.2. Review of current design methods for displacement piles in sand

For the sake of simplicity, in the following it has been preferred to separate the methods for the estimation of the end-bearing resistance q_b from those for the estimation of the shaft resistance q_s.

END-BEARING RESISTANCE IN SAND

The ultimate end-bearing resistance of a pile is generally expressed as:

$$q_b = N_q \cdot \sigma'_{vL} \tag{1.2.1}$$

where N_q is a bearing capacity factor, σ'_{vL} is the in situ effective overburden stress at a depth $z = L_p$ (L_p = pile length).

Values of N_q quoted in the literature vary considerably, but those derived by Berezantzev *et al*. (1961) are used most widely for the design of deep circular foundations (Figure 1.2.1).

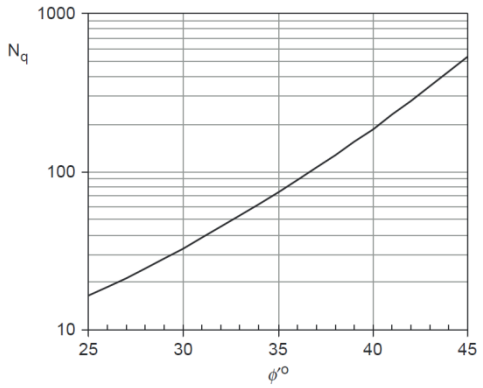

Figure 1.2.1. Variation of N_q with φ (Berezantzev *et al.*, 1961)

The assumption that end-bearing resistance increases linearly with depth up to some limiting value is an idealization that has little support nowadays and is difficult to explain in physical terms. A more widely held view is that, for a homogeneous sand deposit, the end-bearing resistance continues to increase with increasing depth, but at a gradually decreasing rate. This behaviour can be attributed to two effects.

- As the mean stress in the failure region increases (with depth), the friction angle of the soil will decrease (Bolton, 1986). Thus the bearing capacity factor N_q in equation (1.2.1) should be reduced as the overburden stress increases. This effect has been quantified by Randolph (1985) and Fleming *et al.* (1992); the resulting design charts are presented in Fig. 1.2.2, where φ'_{cv} is the (effective) critical state friction angle and I_d is the relative density of the soil.

- The failure beneath the pile tip is a confined failure (with no rupture extending to a free surface), which entails that the end-bearing resistance is affected by the stiffness of the soil, in addition to its strength. Essentially, the bearing capacity factor N_q is an increasing function of the rigidity index I_r (ratio of

stiffness to strength). Since the stiffness of non-cohesive soil increases with the mean stress level to some power less than unity (typically about 0.5), the rigidity index will reduce with depth, resulting in a decrease of N_q with depth.

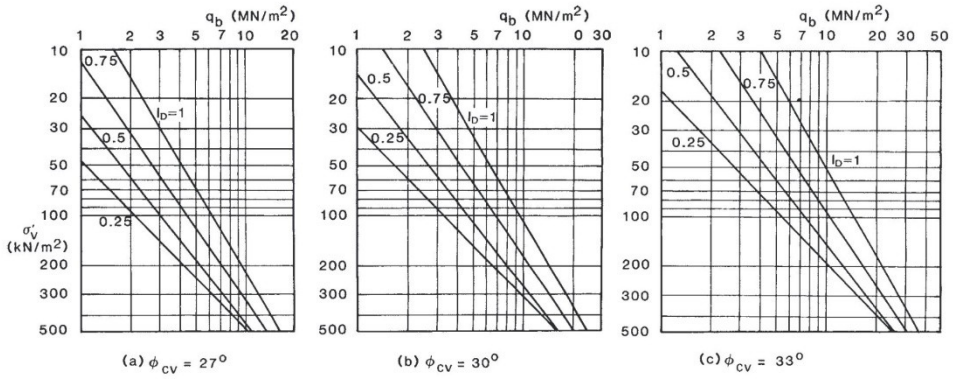

Figure 1.2.2. Base resistance for granular soils (Fleming *et al*., 1992)

Although it is convenient to express the end-bearing capacity of a pile in terms of a bearing capacity factor multiplied by the in situ vertical effective stress, as in equation (1.2.1), the bearing capacity factor will be a function of both the strength (or frictional angle) and the rigidity index (G/p', where G is the shear modulus and p' the mean effective stress) of the material. These quantities vary differently with the absolute effective stress level. In addition, the relative magnitude of the in situ horizontal and vertical stresses will affect the bearing capacity factor (Houlsby and Hitchman, 1988).

In principle, these effects can be quantified through detailed numerical analyses using an appropriate soil model. However, there is no generally accepted model for the stress-strain response of granular material over the enormous strain levels relevant to bearing failure, besides, the computational effort needed to conduct a full parametric study is considered daunting (Randolph *et al*., 1994).

Randolph *et al*. (1994) suggested as alternative to use the analogy between spherical cavity expansion and bearing failure (Gibson, 1950), as depicted in Fig. 1.2.3.

A rigid cone of soil is assumed beneath the pile tip, with the angle α determined by the friction angle of the soil.

Outside the conical region, there is a zone of soil, nominally under isotropic stress equal to the limit pressure for spherical cavity expansion.

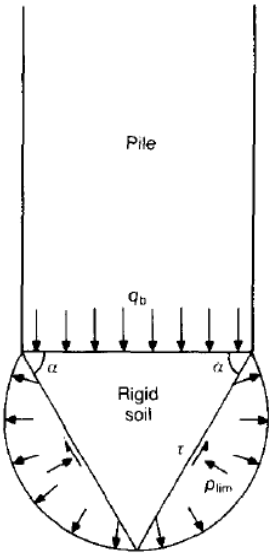

Figure 1.2.3. Relation of cavity expansion limit pressure and end-bearing resistance (from Randolph *et al*., 1994)

It can be shown that the relationship between end-bearing pressure q_b and the limit pressure p_{lim} is:

$$q_b = p_{lim} \cdot (1 + tan\varphi \cdot tan\alpha) \qquad (1.2.2)$$

Assuming that the soil immediately beneath the pile tip has been sheared to its ultimate state, the friction angle φ should be taken as φ_{cv} and the angle α may be taken as $(45 + \varphi_{cv}/2)$.

Equation (1.2.2) can also be used for the cone resistance q_c by taking α as 60° (the cone angle) and φ as δ, the interface friction angle between cone and soil.

The limit pressure for spherical cavity expansion can be evaluated through the closed-form expressions of Carter *et al.* (1986) or Yu and Houlsby (1991) (both solutions yield similar values). These solutions are based on an elastic perfectly plastic soil with a Mohr-Coulomb failure criterion and a constant rate of dilation, and require as input: (a) the in situ mean effective stress p'_0; (b) the friction angle for the soil φ'; (c) the dilation angle for the soil

ψ; (d) the shear modulus G (an equivalent value, allowing for the non-linear stress-strain response of sand); (e) Poisson's ratio ν (which has a relatively small effect).

The friction and dilation angles are assumed constant in the plastic region around the cavity. However, the numerical solutions for cavity expansion published by Collins *et al*. (1992), where the friction and dilation angles varied as the soil approached critical state conditions, show that the appropriate friction and dilation angles to use in these solutions are average values between the initial state ($\varphi = \varphi_{max}$, $\psi = \psi_{max}$) and ultimate state ($\varphi' = \varphi_{cv}$, $\psi = 0$). Thus $\varphi' = 0.5(\varphi_{max} + \varphi_{cv})$ and $\psi = 0.5\psi_{max}$

Following the work of Bolton (1986, 1987), the peak friction and dilation angles can be linked directly to the relative density I_d and the mean effective stress. These correlations (and the averaging process above) lead to effective friction and dilation angles for the cavity expansion solution of

$$\bar{\varphi}' = \varphi_{cv} + 1.5 \cdot I_r \tag{1.2.3}$$

$$\bar{\psi} = 1.875 \cdot I_r \tag{1.2.4}$$

where

$$I_r = 5 \cdot I_d - 1, \text{ for } p' \leq 150 \text{ kPa} \tag{1.2.5}$$

$$I_r = I_d \cdot \left[5.4 - ln\left(\frac{p'}{p_a}\right)\right] - 1, \text{ for } p' > 150 \text{ kPa} \tag{1.2.6}$$

and p_a is atmospheric pressure (100 kPa).

The shear modulus can be correlated with the mean effective stress level and either the void ratio e or the relative density I_r. Lo Presti (1987) has suggested a correlation with relative density of the form

$$\frac{G_0}{p_a} \approx S \cdot e^{c_1 \cdot I_d \cdot \left(\frac{p'}{p_a}\right)^n} \tag{1.2.7}$$

where S is about 600, c_1 is 0.7 and n is about 0.43. Since a number of correlations are available for relative density, it is suggested that equation (1.2.7) may prove more useful, with the coefficient S varied to reflect the silt content. In the first instance, it is suggested that constant values of S = 400, c_1 = 0.7 and n = 0.5 be adopted for a clean silica sand, with the value of S reduced for

more compressible materials (silts or calcareous sands). A preliminary correlation of S with silt content is suggested in Table 1.2.1.

% passing 0·2 mm sieve	0–5	5–10	10–15	15–30
Value of *S*	400	200	100	75

Table 1.2.1. Suggested variation of S with silt content (from Randolph *et al*., 1994)

Predictions of limiting end-bearing pressure, obtained from the cavity expansion approach, are compared with the design charts of Fleming *et al*. (1992) in Fig. 1.2.4, for three different values of relative density (φ_{cv} = 30° and S = 400).

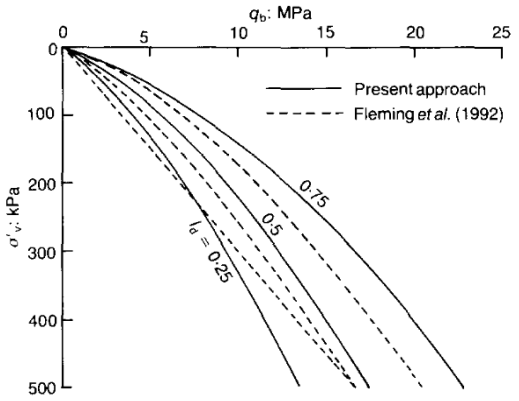

Figure 1.2.4. Comparison of end-bearing resistance profiles (from Randolph *et al*., 1994)

Overall, there is excellent agreement between the two sets of curves but, as expected, the cavity expansion approach leads to greater curvature of the end-bearing profiles. This is due to the effect of decreasing rigidity index with increasing depth. The agreement between the new cavity expansion approach, allowing for the ratio q_b/p_{lim} given by equation (1.2.2) and the design approach of Fleming *et al*. (1992), is encouraging, particularly in view of good correlations of the latter method with pile test data (e.g. Neely, 1991). However, the cavity expansion approach has much greater flexibility in use, since it can allow for the compressibility of different soils.

Figure 1.2.5 shows the effect of varying the shear modulus by a factor of 0.5 or 2, taking S = 200 and 800, rather than the suggested value of 400. It is clear that the stiffness of the soil has a significant effect on the calculated end-

bearing capacity. No limiting value of end-bearing should be stipulated: the tendency towards a limiting value is captured sufficiently by the cavity expansion approach.

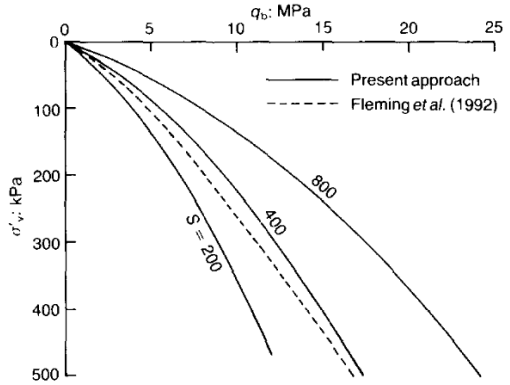

Figure 1.2.5. Effect of varying shear modulus on end-bearing resistance (from Randolph *et al*., 1994)

It must be emphasized that the cavity expansion solution is based on an idealized soil model, and the correlations already given for the shear modulus are limited by real behaviour, which shows that values of the elastic parameters and the correlation index n are all affected by strain level. However, in spite of these limitations, the approach appears to yield realistic estimates of bearing capacity, and to capture the significant effect of stress level on the traditional bearing capacity factor N_q.

With reference to CPT results, the end-bearing resistance is generally expressed as:

$$q_b = k_c \cdot q_c \qquad (1.2.8)$$

where k_c is the factor relating pile end-bearing to the cone resistance q_c.

The French Method (Bustamante and Gianeselli, 1982), based on the results of 71 load tests on instrumented piles, suggest to use the values listed in Table 1.2.2 and to apply them to the average value of the measured cone resistance q_c within depths ranging between 1.5 pile diameters below the base to 1.5 diameters above the base.

State of the sand	q_c (MPa)	Factor k_c Non-Displacement pile	Displacement pile
Loose	≤ 5	0.15	0.5
Medium dense	8 to 15	0.15	0.5
Dense to very dense	> 20	0.15	0.4

Table 1.2.2. k_c coefficient (Bustamante and Gianeselli, 1982)

Meyerhof (1983) prefers to split the coefficient K_c in two distinct coefficient C_1 and C_2:

$$q_b = C_1 C_2 \cdot q_c \tag{1.2.9}$$

in order to take into account the scale effect for the pile and the shallow penetration in dense soil layers.

In particular, $C_1 = C_2 = 1$ if the pile has a diameter $d_p \leq 0.50$ m and a slenderness ratio $L_p/d_p > 10$. If this is not the case ($d_p > 0.50$ m and/or $L_p/d_p < 10$), then $C_1 = [(d_p + 0.5)/2\ d_p]^n$ and $C_2 = L_p\ /10\ d_p$. The exponent n is assumed equal to 1 for loose sand, 2 for medium dense sand and 3 for dense sand. In other words, for medium diameter piles ($d_p = 0.50 – 0.80$ m) and/or short piles ($L_p/d_p < 10$), the end-bearing resistance is smaller than the cone resistance q_c (averaged within d_p above pile base and d_p below the pile base).

Based on piezocone CPTU results, Eslami and Fellenius (1997) suggest slight changes to Meyerhof's method. In particular, the Authors consider the unfiltered data gathered during CPTU test to derive the effective cone resistance q_E by subtracting the measured pore pressure u_2. Once obtained the effective cone resistance, pile base resistance can be calculated from the Eq. (1.2.9) with $C_1 = C_2 = 1$. The value of q_c is obtained in the same way as suggested by Meyerhof, if the sandy soil is rather uniform with depth. In different cases, q_c values have to be averaged within depths ranging between $4d_p$ below and $8d_p$ above pile base for weak into dense soils and from $4d_p$ below to $2d_p$ above for dense into weak soils. It should be then noted that, unlike the other methods presented so far, this method relates the extension of the influence zone not only to the pile geometry, but also to the soil heterogeneity.

Collected data from pile load tests give an apparent diameter effect for piles in sand (Fig. 1.2.6), and this led to the following relation proposed by Chow (1997):

$$\frac{q_b}{q_c} = 1 - 0.5 \log\left(\frac{d}{d_c}\right) \tag{1.2.10}$$

where d_c = 0.036 m is the cone diameter and q_c has to be averaged according to the French Method. It has to be highlighted that Chow (1997) assumes the full mobilization of the ultimate end-bearing resistance at a pile displacement w = 10% d_p.

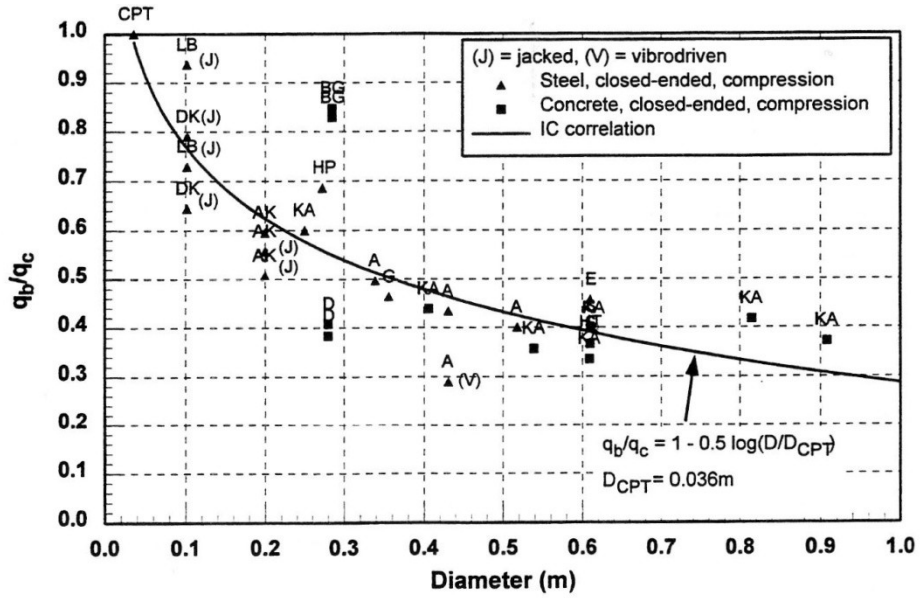

Figure 1.2.6. End-bearing resistance for different pile diameter (Chow, 1997)

SHAFT RESISTANCE IN SAND

The ultimate shaft resistance of a pile is generally expressed as:

$$q_s = k \cdot \sigma'_v \cdot tan\delta \qquad (1.2.11)$$

where k = σ'_{rf}/σ'_v is an earth pressure coefficient relating the normal effective stress acting around the pile at failure (σ'_{rf}) to the in situ effective overburden stress (σ'_v), tanδ is the interface friction coefficient between pile and soil.

In Table 1.2.3 some suggested values for δ (ISO, 2004) are reported: for a given soil type δ, increases for increasing soil relative density (for instance, δ = 25° for medium sand and 35° for very dense sand); for a given soil relative density, δ increases for increasing soil grain size distribution (for instance, δ = 20° for a medium dense sandy silt and 25° for a medium dense sand).

Soil type	Soil density	D_r (%)	δ (°)
Sand	Loose	15-35	20
	Medium	35-65	25
	Dense	65-85	30
	Very dense	85-100	35
Silty sand	Loose, Med	15-65	20
Clayey sand	Dense	65-85	25
	Very dense	85-100	30
Sandy silt	Loose	15-35	15
	Med. dense	35-85	20
	Very dense	85-100	25

Table 1.2.3. Values of δ for displacement piles in sand (ISO, 2004)

These empirical suggestions (like others not mentioned here) are not consistent with the physical processes that occur around a displacement pile. The interface friction angle, indeed, has been found to be most strongly affected by the ratio of grain size to pile roughness and therefore increases with decreasing grain size rather than the reverse trend indicated in Table 1.2.3 (Uesugi and Kishida, 1986; Jardine *et al*., 1992). There is also no evidence to suggest that δ should vary with the in situ relative density of the sand, as long as the major changes that occur during installation and the likelihood that critical state conditions are developed along the pile-soil interface.

In Table 1.2.4 are summarized the suggested values for k and $\mu = \tan\delta$ by AGI (1984). Looking at displacement piles, the values of k are ranging between 0.7 (for partial displacement piles like H piles are) and 1.0 (for all the other full displacement pile types) in loose sandy soils. Larger values are suggested in dense sandy soils.

For displacement piles in sand, API (1993) proposes values of q_s to not be exceeded (Table 1.2.5). These values are derived by assuming that the earth pressure coefficient k is constant with depth (= 1 for closed-end piles) and δ is the dominant variable.

Adoption of a constant k value with depth, together with a limiting value for q_s, is not consistent with data from field tests; even the original work of Vesic (1970) shows evidence of what is often referred as friction fatigue (Heerema, 1980), and a more quantitative picture was provided from the Imperial College instrumented model pile tests (Lehane *et al*., 1993; Chow, 1996).

Pile type	*Values of k for relative density*		*Values of μ*
	Loose	*Dense*	
Displacement: steel H section	0.7	1.0	tg20° = 0.36
closed end pipe	1.0	2.0	
precast concrete	1.0	2.0	tg3φ/4
cast in place concrete	1.0	3.0	tgφ
Intermediate presso drill	0.7	0.9	tgφ
Replacement drilled shaft	0.5	0.4	tgφ
CFA	0.6	0.6	tgφ

Table 1.2.4. AGI recommendations for k and μ = tanδ values for different pile types (Associazione Geotecnica Italiana, 1984)

	$API(1993)$		
Density	relative density (%)	δ	τ_s (kPa)
very loose	0 - 15	15	48
loose	15 - 35	20	67
medium dense	35 - 65	25	81
dense	65 - 85	30	95
very dense	85 - 100	35	115

Table 1.2.5. API recommendations for displacement pile design (API, 1993)

Formerly, Kulhawy (1984) argued that the experimental observation of limiting shaft friction arises from a combination of decreasing friction angle with depth (or stress level) and decreasing k values with depth, due to the natural tendency for the in situ stress ratio k_0 to decrease with depth.

The effect of a decreasing friction angle with an increasing stress level has been accounted for in the approach proposed by Fleming *et al*. (1992). They suggest taking k as a constant proportion of N_q ($k = 0.02 \cdot N_q$), together with an interface friction angle equal to critical state friction angle φ_{cv}, which leads to the following equation

$$q_s = 0.02 \cdot q_b \cdot tan\varphi_{cv} \tag{1.2.12}$$

This approach leads to ratio q_s/q_b in a rather good agreement with field measurements (e.g. Vesic, 1970), although tends to overestimate shaft capacity for long piles.

An important effect ignored in all the approaches presented so far, is the well-established observation that the local shaft resistance at any depths varies with pile penetration due to the so-called “friction fatigue” (Heerema, 1980).

Toolan *et al*. (1990) propose a design approach that allows for degradation of friction due to the length of the installed pile. They describe two approaches, both of which take into account the friction degradation, but in different ways.

The first approach is based on the experimental observation that the average shaft friction reaches a limiting value at quite shallow penetrations. Then they suggest empirical correlation of average measured shaft resistance with relative density (Table 1.2.6): the actual distribution of shaft resistance is assumed to be triangular, where the value at the pile base is two times the average value. For soils of intermediate relative densities a linear interpolation is used. The assumption of a triangular distribution of shaft friction leads to gradual reduction of shaft friction as the pile penetration is increased, thus accounting for the effects of friction degradation, although in simplistic way.

Soil description	Relative density	Shaft friction: kPa			
		Open-ended piles		Closed-ended piles	
		Average	Tip	Average	Tip
Loose	25	12	24	15	30
Medium dense	50	20	40	25	50
Dense	75	40	80	50	100
Very dense	90	80	160	100	200

Table 1.2.6. Design approach for average shaft resistance (Toolan *et al*., 1990)

The alternative approach adopts a fixed ratio $\beta = q_s/\sigma'_v$, which is a function of relative density and pile penetration and applies over the bottom 10 m of the piles. The proposed correlation is shown in Figure 1.2.7 for full displacement piles. For piles that are embedded beyond 10 m, the shaft resistance down to 10 m above the pile base is calculated using a value of β that is lower of 0.24 and the value from Figure 1.2.7. Once again, the value of β = 0.24 reflects degraded friction due to two-way plastic slip during installation.

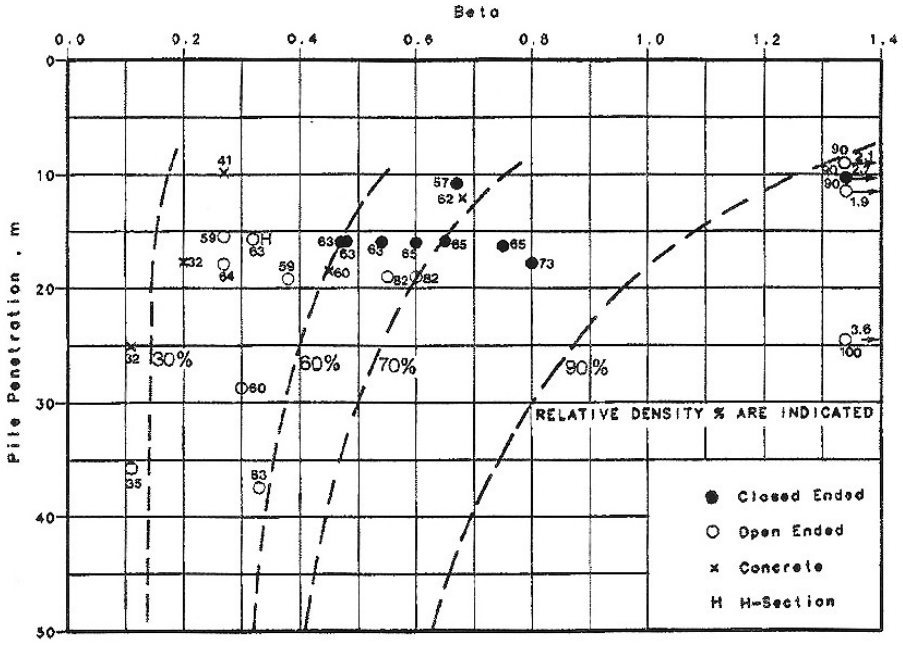

Figure 1.2.7. Variation of β with pile penetration (Toolan *et al*., 1990)

Randolph *et al*. (1994) and Randolph (2003) postulate that, at any given depth, the shaft resistance will degrade from the peak value towards the minimum value, as an exponential function of the length of pile driven past the location. Thus the shaft friction at depth z can be written in terms of local value as:

$$q_s = \left[K_{max} - (K_{max} - K_{min}) \cdot e^{-\mu h/d_p}\right] \cdot \sigma'_{v0} \cdot tan\varphi_{cv} \qquad (1.2.13)$$

where K_{max} and K_{min} are the maximum and minimum earth pressure coefficients, h is the distance from the pile base and μ is a parameter that gathers all the information about soil compressibility, pile roughness, jacking energy (ranging between 0.05 to 0.1).

In particular, K_{min} is related to the active pressure coefficient and can vary from 0.2 to 0.4, while K_{max} is a function of the end-bearing capacity factor N_q:

$$K_{max} = 2 \cdot N_q e^{-7tan\varphi_{cv}} \qquad (1.2.14)$$

With reference to CPT results, the shaft resistance is generally expressed as:

$$q_s = \frac{q_c}{\alpha} \tag{1.2.15}$$

where α is a coefficient depending on soil relative density and pile type.

Table 1.2.7 summarizes the suggested values for the French Method (Bustamante and Gianeselli,1982). As it can be seen, for displacement piles 1/α is kept constant and equal to 300 for steel piles and 150 for concrete piles, independently from soil relative density; in any case, a limiting value of 120 kPa is suggested.

State of the sand	q_c (MPa)	Pile category							
		Non-displacement				Displacement			
		no tube|		with tube		Steel		Concrete	
		$1/\alpha$	q_{smax} (MPa)	$1/\alpha$	q_{smax} (MPa)	$1/\alpha$	q_{smax} (MPa)	$1/\alpha$	q_{smax} (MPa)
Loose	≤ 5	200	-	250	-	300	-	150	-
Medium dense	8 to 15	200	-	250	0.04	300	-	150	-
Dense to very dense	> 20	200	0.12	300	0.120	300	0.120	150	0.12

Table 1.2.7. Values for α (Bustamante and Gianeselli, 1982)

Similar values are reported by Eslami and Fellenius (1997).

The *Imperial College Method* (Jardine *et al.* 2005) has been developed on the basis of the experimental data related to the measurements made during the installation and subsequent loading of a jacked displacement pile (the so-called Imperial College Pile) in Labenne sand and in the dense sand of Dunkirk.

It explicitly considers all the terms contributing to the shaft resistance by the following equation:

$$q_s = (\sigma'_{h0} + \Delta\sigma'_{inst} + \Delta\sigma'_{load}) \cdot tg\delta \tag{1.2.16}$$

where σ'_{h0} is the effective geostatic radial stress, $\Delta\sigma'_{inst}$ is the radial stress change caused by the installation process, $\Delta\sigma'_{load}$ is the radial stress change that occurs during the pile; δ is the pile-soil interface friction angle.

The method concentrates on the estimation of the horizontal stress existing soon after the pile installation ($\sigma'_{inst} = \sigma'_{h0} + \Delta\sigma'_{inst}$) and the change occurring during pile loading ($\Delta\sigma'_{load}$):

$$\sigma'_{inst} = 0.016 \cdot q_c \cdot \left(\frac{\sigma'_{v0}}{p_a}\right)^{0.13} \cdot \left(\frac{2h}{D}\right)^{-0.38} \quad (1.2.17)$$

$$\Delta\sigma'_{load} = 4G\frac{\delta h}{D} \quad (1.2.18)$$

where h is the distance of the reference depth from the pile base, D is the pile diameter, G is the soil shear modulus, δh refers to the radial sand dilation, p_a is the atmospheric pressure.

According to Boulon and Foray (1986), equation (1.2.18) derives from the assumption of linear elastic behaviour of the soil around the pile during loading stage.

The radial sand dilation δh depends on soil relative density, the initial radial stress and the pile surface roughness. Chow (1997) and Jardine *et al*. (2005) relate the radial displacement δh to the average distance R_a of the peaks and depressions of asperities with respect to the central profile of pile shaft; typically, it is assumed $R_t = 2R_a$, where R_t is the average distance of peaks and depressions over an 8 mm pile length.

The soil shear modulus G should be estimated in correspondence of the shear strains that occur in the soil surrounding the pile during the loading phase; however, if not available from direct measurements, Jardine and Chow (1996) suggest the use of the expression given by Baldi *et al*. (1989), valid for small strain level:

$$G_0 = q_c \cdot [A + B \cdot \eta - C\eta^2]^{-1} \quad (1.2.19)$$

with $\eta = \frac{q_c}{\sqrt{p_a \cdot \sigma'_{v0}}}$, where A, B and C are empirical factors with the values 0.023, 0.00125 and 1.216E-6, respectively.

Fioravante (2002) suggests an operative value for G of about 5-10% G_0 with the latter obtained from the equation proposed by Jamiolkowski *et al*. (1994):

$$G_0 = 72.4 \cdot \left(\frac{\mathrm{p}'}{\mathrm{p_a}}\right)^{0.45} \cdot \frac{1}{\mathrm{e}^{1.3}} \quad (1.2.20)$$

in which e is the void ratio.

1.3. Installation effects

1.3.1. Experimental studies

White and Lehane (2004) provide the experiments carried out on four jacked pile installations in centrifuge at the University of Western Australia.

The stainless steel piles are squared, with a B x B = 81 mm^2 area and a length L_p = 120 mm (L_p/B = 13.3); they are pushed monotonically with a penetration rate v = 0.2 mm/s into two steps of 60 mm (L_p/2). The tests are performed in a medium dense fine silica sand at an acceleration level of 50g. During the tests, the horizontal stresses at the pile-soil interface have been measured by means of six total stress cells at four different location depths h behind the pile base (h/B = 1, 3, 6 and 9). In Figure (1.3.1.1) the measurements, recorded during one case of monotonic installation for each instrumented section, are shown.

As it can be seen, the horizontal stress at each measurement point during pile insertion is increasing with depth with a more-than-linear variation law and at a fixed penetration level, for example at z = L_p = 120 mm, σ'_{hm} increases with the measurement point depth.

Later on, the same Authors (Lehane and White, 2005) provide the variation of the lateral stress at pile shaft with pile head displacement as measured during the load test on piles (Figure 1.3.1.2).

For increasing applied load at pile head, the lateral stress σ_h increases at all the depths. At small pile head displacement (about 0.5 mm), at the section closer to the tip (h/B = 1) the maximum value for σ_h is observed; at the intermediate section (h/B = 3) the limit value for σ_h is attained at the end of installation and it overtakes the value measured at the deeper section; the measured value at shallow depth (h/B = 6) does not exhibit a limit value. It is worth of mentioning that the load test has been stopped at a pile head displacement of about 50% of pile diameter.

Figure 1.3.1.3 summarizes the distribution with depth of the lateral stresses σ_h at the end of the installation and of the load test: it is clear from the measurements that in both the cases σ_h increases with depth, with almost doubled values at the end of the loading stage if compared with those existing at the end of the installation stage.

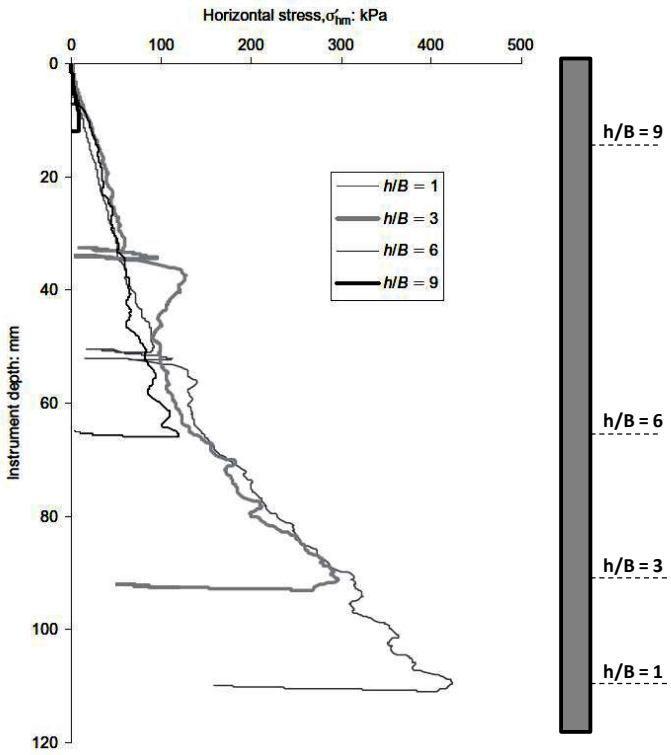

Figure 1.3.1.1. Horizontal stress during installation (White and Lehane, 2004)

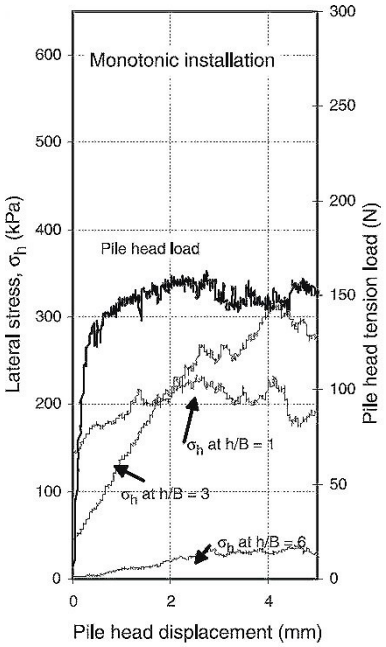

Figure 1.3.1.2. Development of lateral stress during load test (Lehane and White, 2005)

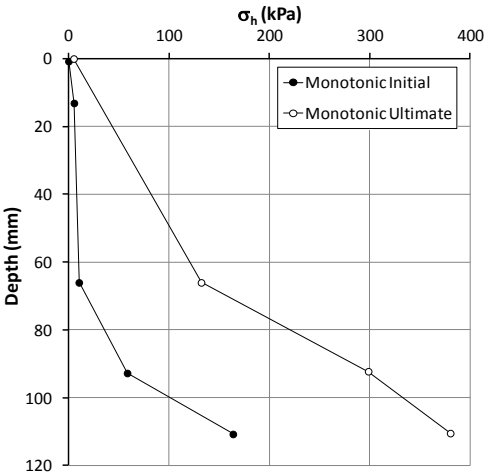

Figure 1.3.1.3. σ_h distribution with depth at the end of the installation and at the end of load test (Lehane and White, 2005)

Gavin and O'Kelly (2007) present a series of field tests of displacement piles installation. The tests are performed in the heavily overconsolidated Blessington sand (Ireland) with a close to 100% relative density. The stainless-steel model pile is tubular, with an outer diameter d_p of 73 mm and a length of 3.44 m ($L_p/d_p \approx 46$). The piles were instrumented at three different distances from the tip (h/d_p = 1.5, 5.5 and 10) by total earth-pressure and pore pressure transducers. Piles are pushed into the soil with a penetration rate of 20 mm/s.

Figure 1.3.1.4 reports the horizontal stresses σ'_{hp} recorded at each instrumented section during pile penetration. As it can be noticed, σ'_{hp} appears almost constant with pile insertion, in contradiction with the centrifuge results by White and Lehane (2004). It is confirmed that σ'_{hp} values decrease with the distance from the pile tip h/d_p, instead.

Dijkstra (2009) reports the results of five centrifuge tests at an acceleration of 35g in Baskarp sand. The model is prepared by pumping the sand in suspension in a circular strong box with a 600 mm outer diameter and a total height of 1 m, then densifying the sand from a maximum porosity n = 0.455 down to a minimum porosity n = 0.382.

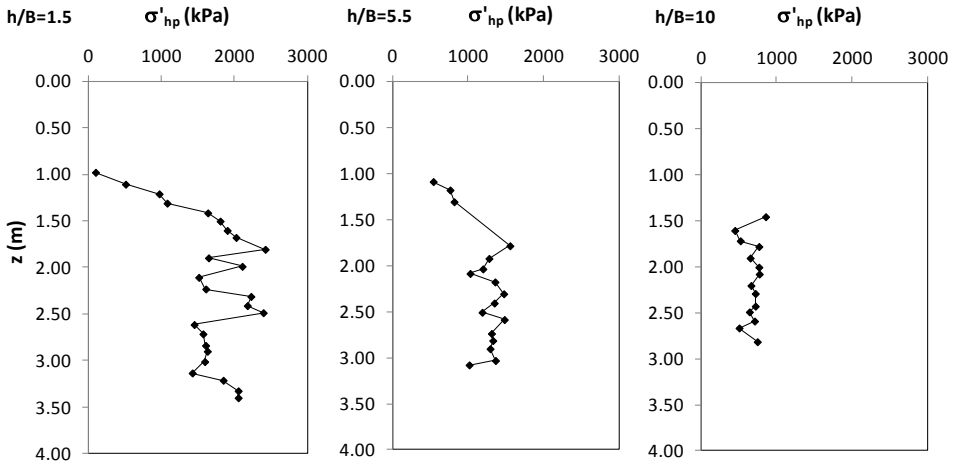

Figure 1.3.1.4. Horizontal stress during installation (Gavin and O'Kelly, 2007)

Pile model, which is already fixed in place, is 450 mm in height and has a diameter of 15 mm; it is initially embedded for 205 mm ($L_p/d_p \approx 13$) and is instrumented at three depths levels for the measurement of the density variation at 35, 110 and 200 mm from the base. During the test it is further embedded for 200 mm.

Figure 1.3.1.5 reports the change of porosity measured during the pile insertion: as it can be seen, independently from the initial value (that means from a loose or dense state), the porosity increases close to the pile during each test. The Author attributes these findings with the dilatancy occurring at pile interface during the initial monotonic shearing. In addition, from the experimental data it can be argued that the porosity increment is larger for dense samples than for the loose ones.

For all the tests, despite the initial conditions, after a pile insertion of about 10 times pile diameter, no more changes in porosity are observed, in some way suggesting that a sort of critical state has been attained.

For all the centrifuge tests, Figure 1.3.1.6 shows how the installation forces at pile head (a), at pile base (b) and at pile shaft (c) change with the penetration depth: as expected, the higher is density the higher is installation force, but in no case the resistances attain a limit value.

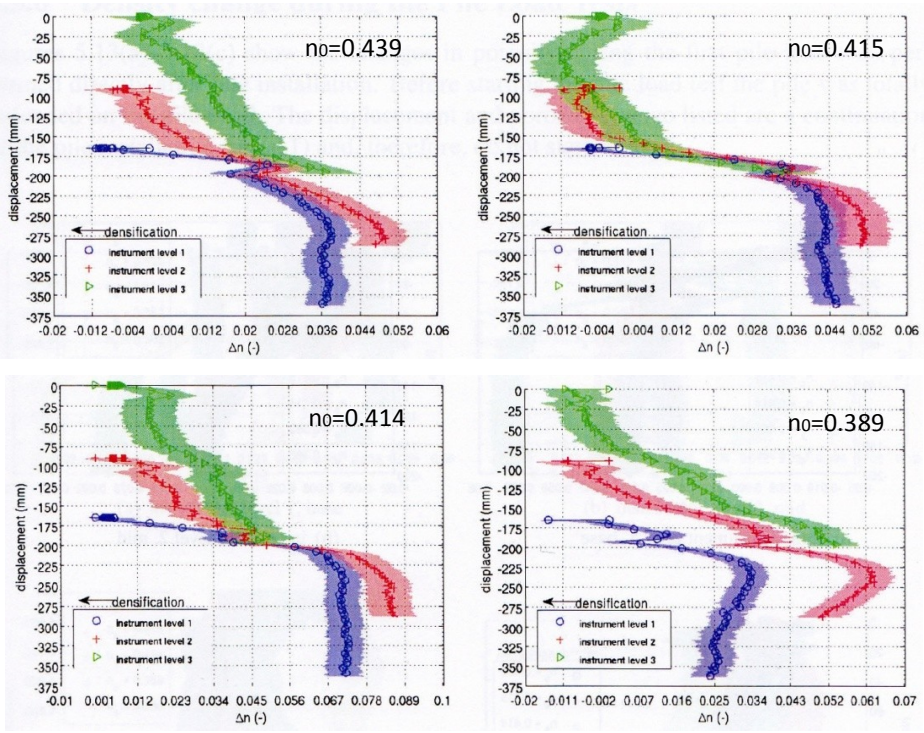

Figure 1.3.1.5. Change of porosity during pile installation in soil from loose to dense initial state (Dijkstra, 2009)

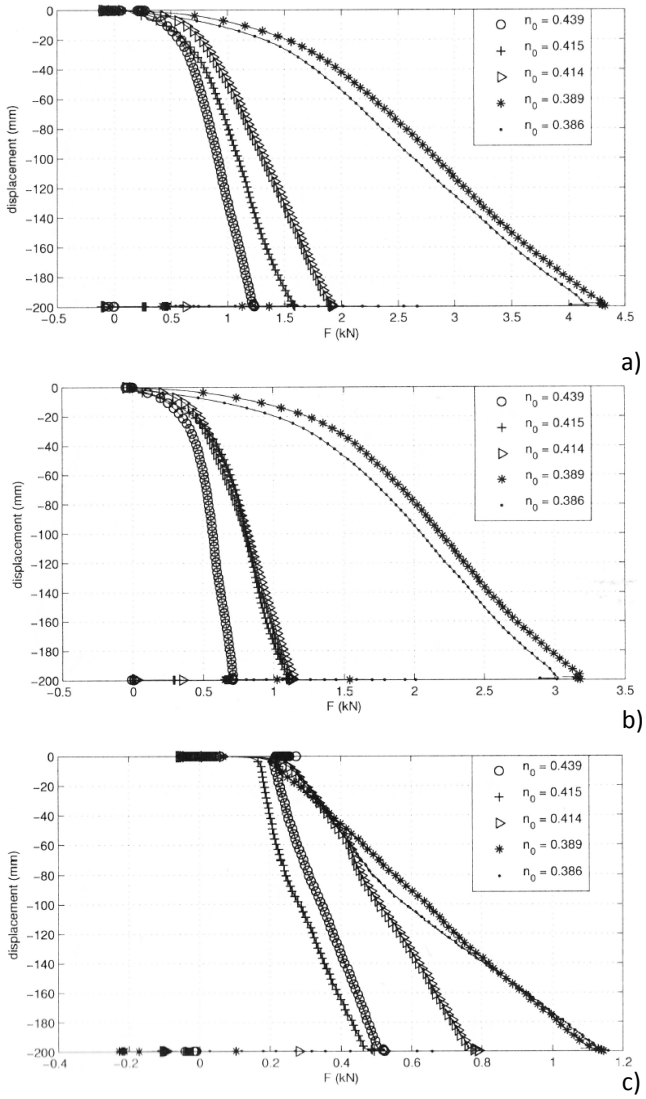

Figure 1.3.1.6. Measured force at pile head (a), pile base (b) and pile shaft (c) during installation (Dijkstra, 2009)

1.3.2. Theoretical studies

The theoretical approach for the study of installation effects is based on the cavity expansion theory, which focuses on the stress and displacement fields around embedded cavities. The use of cavity expansion theory to solve practical problems is generally defined "cavity expansion method". The main applications of this method in Soil Mechanics, so far, is the interpretation of in-situ testing, i.e. cone penetrometer test and pressumeter test.

Salgado and Prezzi (2007) propose a cavity expansion-based theory for calculation of cone penetration resistance q_c in sand checked by comparison with calibration chamber penetration tests. This work, following Salgado (1997), shows that the penetration of a cone in a sandy soil induces a horizontal displacement field, just below the cone tip, so that this mechanism can be described by the cylindrical cavity expansion theory. Hence, there is a strict relation between cone penetration resistance and the pressure required to expand a cavity from a zero initial radius. The cylindrical cavity pressure depends on the horizontal initial effective stress, relative density and friction angle.

If an infinite soil mass is considered and a cavity expanded from zero initial radius to a certain radius *a*, in the immediate proximity of the cavity it is created a plastic zone with radius *R*; beyond this zone there is a non-linear elastic zone which extends from radius *R* to *A* and that is bounded by a linear elastic zone (Figure 1.3.2.1).

The cavity expansion analysis is carried out considering the single zones separately and each zone is divided in thin shells which are bounded by inner and outer radii r_i and r_j measured from the cavity's centre.

Firstly, it is considered the plastic zone, where the combination of a yield criterion for purely frictional soils and the equilibrium equation:

$$\begin{cases} \sigma_r = N_{ij}\sigma_\theta \\ \dfrac{d\sigma_r}{r} + \dfrac{\sigma_r - \sigma_\theta}{r} = 0 \end{cases} \tag{1.3.2.1}$$

gives the effective radial stress during the expansion σ_r

$$\sigma_{ri} = \sigma_{rj}\left(\frac{r_j}{r_i}\right)^{\frac{N_{ij}-1}{N_{ij}}} \tag{1.3.2.2}$$

where σ_θ is the hoop stress around the expanding cavity and N_{ij} is the flow number at the centre of the element defined by the following ratio

$$N_{ij} = \frac{1 + sen\varphi_{ij}}{1 - sen\varphi_{ij}} \qquad (1.3.2.3)$$

with φ_{ij} the friction angle within the shell ij. The Authors refer to a friction angle which varies according to the Bolton's model for uncemented sands (Bolton, 1986), for plane strain conditions, considering the mean effective stress at the centre of the shell.

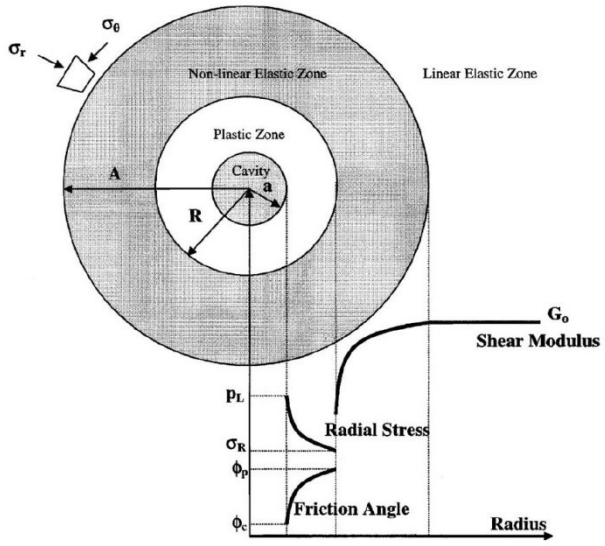

Figure 1.3.2.1. Plastic and elastic zone in cavity expansion (Salgado *et al*., 1997)

Eq. (1.3.2.2) defines the variation of the radial effective stress during cavity expansion, for each single thin shell which the soil surrounding the cavity is divided in. However, in order to obtain a relation for the cone penetration resistance q_c, as aforementioned depending on the cavity limit pressure, it is necessary to determine the limit radial stress at the border of plastic zone:

$$p_L = \sigma_R \left(\frac{R}{a}\right)_L^{\frac{N-1}{N}} \qquad (1.3.2.4)$$

where σ_R is the radial stress at the elastic-plastic interface defined by the following expression

$$\sigma_R = \frac{2N_p}{N_p + 1}\sigma_{h0} \qquad (1.3.2.5)$$

R is the plastic zone radius, a the cavity radius and N the flow number.

This closed-form is valid only in the hypothesis of linear elasticity and perfect plasticity (Carter *et al*., 1986 and Yu & Houlsby, 1991); it can be noticed that for very low values of friction angle the ratio $2N_p/(N_p+1)$ tends to 1, while for very high values it tends to 2; thus, whatever is the friction angle, the radial stress at the elastic-plastic interface varies in the range $\sigma_{h0} < \sigma_R < 2\sigma_{h0}$.

Once the radial stress at the plastic zone and the limit pressure are determined, it is possible to calculate the cone resistance. Salgado *et al*. (1997) point out that, for sands, the penetration of the cone device creates a displacement field that tends to be horizontal, therefore from the cone tip to the side a stress rotation is needed. The admissible slip mechanism they consider in order to develop a reliable analysis is showed in Figure 1.3.2.2. It is a slip mechanism with interface friction angle δ_c. Below the conical tip a transition zone is set up by an infinite number of log-spiral surfaces whose extension depends on δ_c, the operative friction angle φ_T, the operative dilatancy angle ψ_T of the transition zone and the semiapex angle of the cone θ_c.

The Authors determine the principal stresses at the cone surface through an analytical dissertation (for details refer to Salgado and Prezzi, 2007); these are then integrated, in order to obtain the total vertical force opposing penetration and, dividing the resultant for the cross sectional area of the cone, the q_c resistance is finally defined as:

$$q_c = 2f_v p_L \exp(2\Delta\lambda \tan\varphi_T)\frac{(1 + C_\lambda)^{\eta+1} - C_\lambda(\eta + 1) - 1}{C_\lambda^2\eta(\eta + 1)} \qquad (1.3.2.6)$$

where $\Delta\lambda$ is the angle between the log-spirals at which the principal stress becomes horizontal and depends on the friction interface angle and the semiapex angle of the cone; C_λ is a coefficient that depends on the friction interface angle, the semiapex angle of the cone and on the operative friction and dilatancy angle in the transition zone; eventually η is a coefficient which is a function of the operative friction angle in the transition zone.

f_v is a coefficient that depends on the critical flow number N_c, the cone interface angle δ_c and the semiapex angle of the cone θ_c and has the following expression

$$f_v = \frac{1}{2}\left[\left(1+\frac{1}{N_c}\right)+\left(1-\frac{1}{N_c}\right)(\cos\delta_c \cot\theta_c - \sin\delta_c)\right] \qquad (1.3.2.7)$$

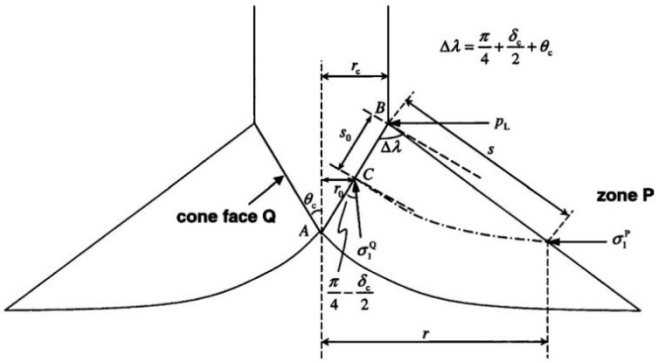

Figure 1.3.2.2. Variation of plastic radius with the initial lateral effective stress for different friction angles (Salgado and Prezzi, 2007)

The Eq. (1.3.2.6) has two unknown parameters, q_c and φ_T, for this reason the Authors suggest to solve it by means of an iterative procedure which consists of:

- Assume value for φ_T, thus computing ψ_T and N_T;
- Compute η, $\Delta\lambda$ and C_λ;
- Compute φ_T from the Bolton's relation;
- Compute q_c.

1.3.3. Numerical studies

Dijkstra (2009) performs numerical simulation of the centrifuge tests by the finite element method. The installation of a jacked pile is simulated by the software *Tochnog*, which allows large deformations with an hypoplastic constitutive model.

Two numerical approaches are used: a fixed pile model and a moving pile model. The former consists in soil moving along a fixed in place pile, while in the latter the pile penetrates in a fixed soil (Figure 1.3.3.1). Both models are axy-

symmetric; geometry and results are first scaled at the prototype scale, instead of considering the artificial acceleration field of the centrifuge.

The mesh consists of 5600 quadrilateral elements and is refined near the pile; the mesh radius R and height H are respectively 5 m and 10 m. The pile has a radius r = 0.25 m and a length L = 5 m (slenderness ratio L/r = 20).

At pile-soil interface shear force is assumed to be reduced to 51% of the undisturbed shear strength. In both models the horizontal velocity is zero; in the fixed pile approach the initial conditions (initial stress of 100 kPa and initial porosity from centrifuge tests) are prescribed on the lower boundary, as well as a vertical soil velocity of 35 mm/s.

For the moving pile approach, instead, the initial stress is obtained from initial gravity calculation and vertical velocity is set to zero on the lower boundary.

The simulations are performed in loose (n = 0.439), medium dense (n = 0.415) and dense sand (n = 0.389).

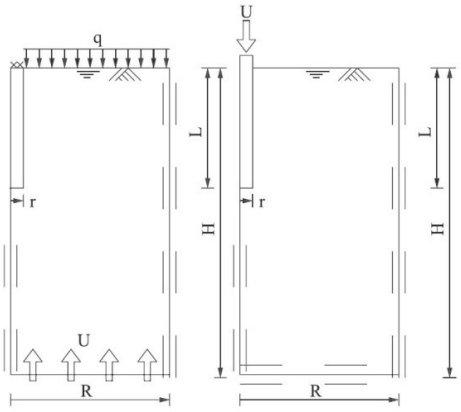

Figure 1.3.3.1. Fixed pile model -left- and moving pile model -right- (Dijkstra, 2009)

In Figure (1.3.3.2) and (1.3.3.3) the distributions of the horizontal σ_{xx} and vertical σ_{yy} stresses after five metres of pile installation, from the different approaches, are shown.

The horizontal stress reaches the highest values just below t pile base and then this increment reduces at the increasing radial distance from pile axis. The extension of the influence zone increases with the decreasing porosity, in particular, it spread over a 4r distance from pile axis for loose sand and till a 6r distance for dense sand.

Concerning the vertical stress σ_{yy}, it reaches the peak value below pile base, which reduces at the increasing distance from the pile. Unlike the horizontal stress increment, this is concentrated only below the base, therefore its variation does not influence the pile shaft.

The analyses show that very similar mechanisms of compression below the pile after the five meters insertion for both approaches, though the maximum values reached by the stresses in the moving pile model are higher and the influence zones are more widespread than the fixed pile approach. These differences lie, of course, on the very different mechanisms that are at the base of the two models: the fixed pile approach is not realistic and it is just a numerical artifice for obtaining a stress and strain state, both below the tip and at the shaft, quantitatively comparable with the measured one, while the moving pile approach reproduces what actually happens in situ, i.e. the pile displaces and the soil is relocated as a consequence. For these reasons the results from the moving pile approach are considered more trustworthy.

In addition, the porosity variation is reported in Figure 1.3.3.4, for the three initial states (loose, medium dense and dense sand). Despite the initial conditions, for both approaches, at the pile shaft a loosening occurs because of a dilatancy phenomenon, which reduces with the increasing distance from the pile interface; in particular, porosity reaches the initial values at a distance of one radius from the pile. At the base, in the loose sample porosity initially decreases, but then it increases with the distance from the pile. For medium dense and dense sample, instead, there is a decompression which reduces with the increasing distance from the pile.

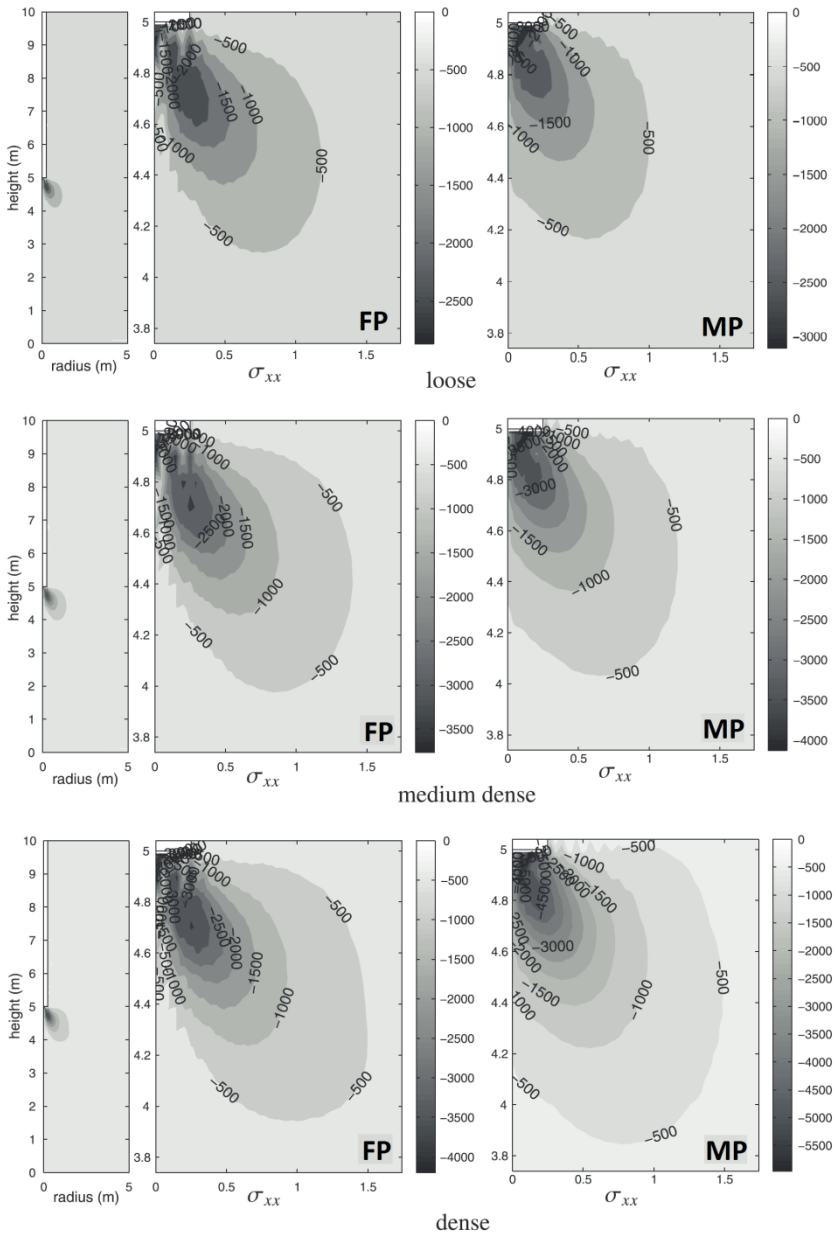

Figure 1.3.3.2. Horizontal stress distribution (in kPa) for fixed (FP) and moving (MP) for three different porosities (Dijkstra, 2009)

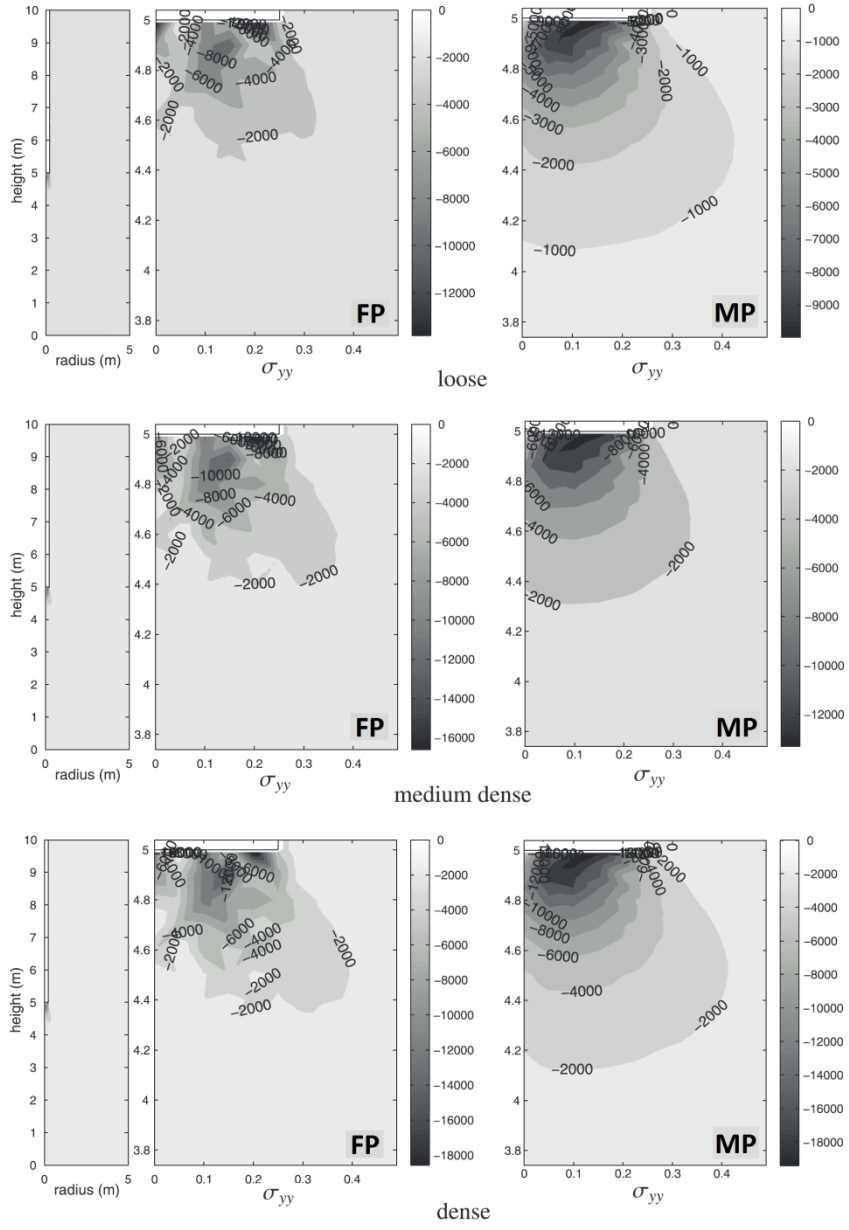

1.3.3.3. Vertical stress distribution (in kPa) for fixed (FP) and moving (MP) pile approach for three different porosities (Dijkstra, 2009)

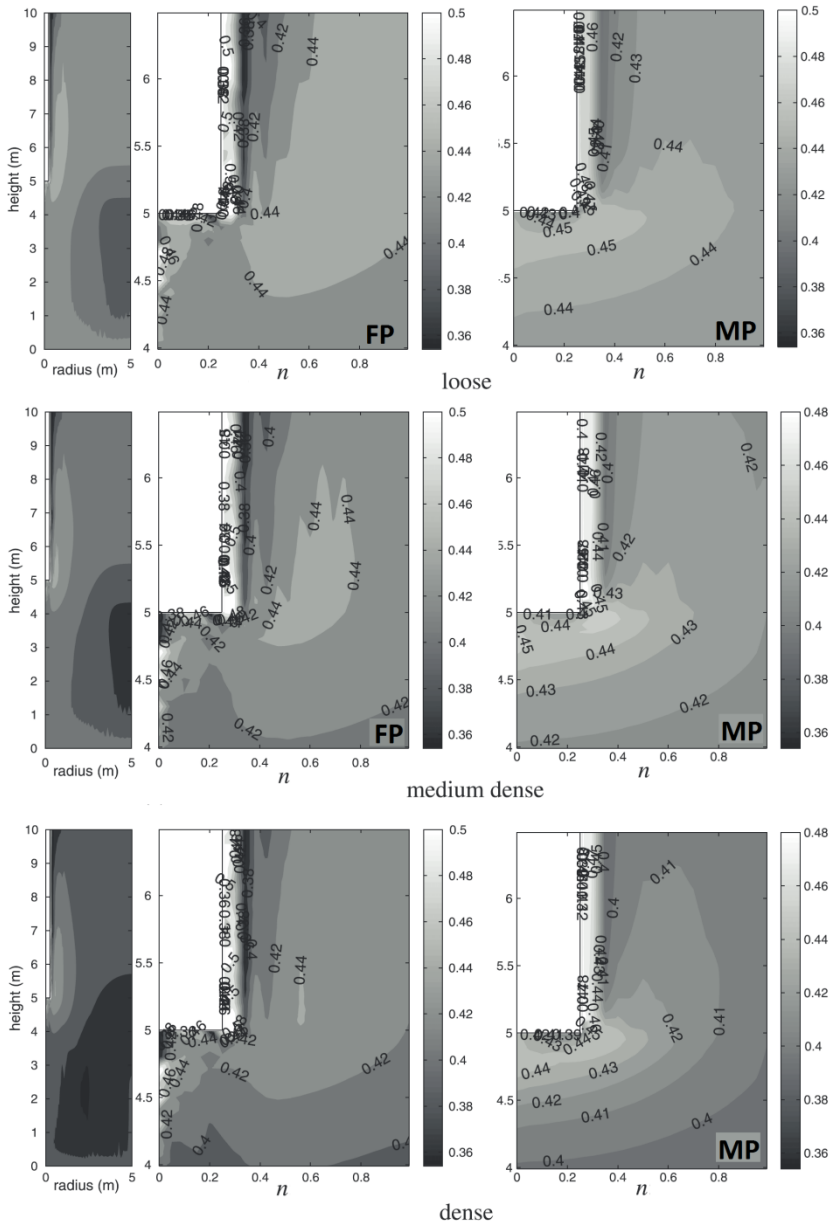

Figure 1.3.3.4. Distributions of porosities for fixed (FP) and moving (MP) pile approach (Dijkstra, 2009)

More exhaustive results are provided by Sheng *et al*. (2006) who reproduce centrifuge tests, which jacked pile installation in dry sand is performed in, by the finite element method. The device has a diameter of 30 mm and is installed for 230 mm ($L_p/d_p \approx 8$) at an acceleration gravity of 66.7g, only in the finite element analysis the base has a cone shape with an angle of 60°. The soil is modelled with the Cam Clay constitutive model; the earth pressure coefficient at rest K_0 is assumed to 0.5 for medium dense sand.

The numerical analyses are executed considering at pile/soil interface the Mohr-Coulomb criterion with a (very low) friction coefficient which can vary from 0 to 0.4. Thanks to this new contact formulation, it is possible to solve the problem of the stiffness contrast between soil and pile, therefore they obtain the variation of the stresses along the pile body during installation, just considering a pile with a finite stiffness E = 100 GPa.

Figure (1.3.3.5) shows the results in terms of radial (a and d), vertical (b and e) and hoop (c and f) stress variations in the soil and in the pile at the end of pile installation for a case without interface friction ($\mu = 0$, for the figures a, b and c) and $\mu = 0.1$ (for the figures d, e and f). Firstly, it can be noticed that for $\mu = 0$ and $\mu = 0.1$ the differences in terms of stress variation both for pile and soil are not significant: from this observation derives that the considered interface friction coefficient is too low. In addition, the horizontal stress variation (Figure 1.3.3.5 a and d) shows a gradually increase with depth in pile body. Regarding to the soil, instead, there is a peak at the side corner of the conical tip, that decreases at the increasing radial and vertical distance from the base. The vertical stress variation presents a strong increase constant along the whole pile body, whilst the soil has a gradually increase from surface to pile base, where it assumes the largest values.

Eventually, as to the hoop stress, pile is subjected to a gradual increase at the increasing depth, besides, the surrounding soil has an increase around the conical base, which reduces at the increasing vertical and radial distance from the pile.

Jiang *et al*. (2006) perform 2D discrete numerical analyses of cone penetrometer tests in sand. The model consists of about 10000 disk particles, whose mean diameter is 2.925 mm and homogeneity coefficient $d_{60}/d_{10} = 1.25$; thanks to the geometry of the cone the model is axial-symmetric with a height of 16R and a width 17.5R (where R is cone radius). The cone is made of three walls: the conical frictional tip with an angle of 60° and height h, a cylindrical

frictional sleeve with height h and the last frictionless wall whose height depends on the level of penetration of the device in the soil.

The ratio between cone diameter and mean soil diameter (R/d_{50}) is 10.7 and the cone penetration rate is 2 mm/s. The boundary walls are rigid, frictionless and fixed, except for the side one which as a K_0-boundary.

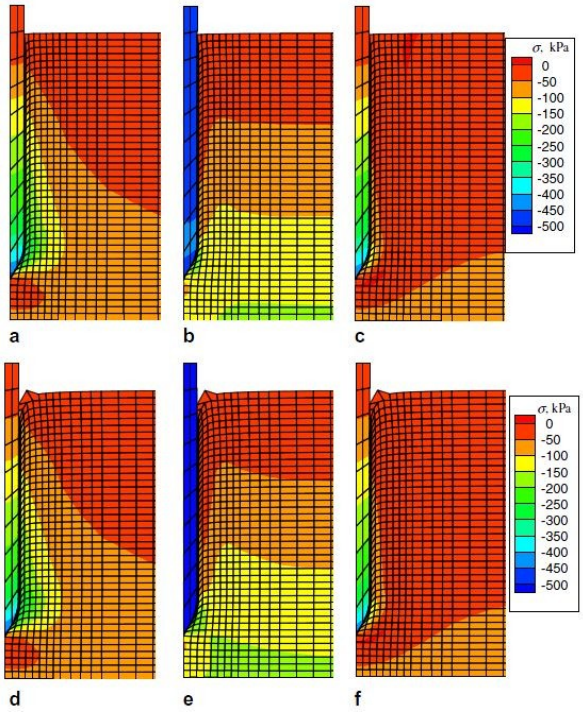

Figure 1.3.3.5. Variation of radial stress at the end of pile installation (Sheng *et al.*, 2006)

The Authors defined also six control points at four sections for three different depths where the stress state is measured (Figure 1.3.3.6).

The simulations are performed considering the contacts between particle and wall with and without friction (respectively Perfectly-Rough model with $\mu = 0.5$ and Perfectly-Smooth model with $\mu = 0$) .

The variation of mean and deviatoric stresses measured during cone installation at the six control points are presented in Figure 1.3.3.7. Both the mean and deviatoric stresses are not influenced by the particle-wall friction at the cone interface; they depend on the distance from the measure point and the pile shaft. In particular, at the increasing distance from pile/soil interface the

installation effects reduce. However, for Section 1,3 and 5, after a peak value (that is recorded when the cone tip is at the same depth of the measure point) the stresses decrease and substantially reach the initial values. These results are consistent with the friction fatigue phenomenon.

Figures 1.3.3.8 a)-d) show the horizontal displacement u_x for columns 1-4, for the perfectly rough and perfectly smooth models, measured during cone installation for the control sections. As expected u_x increases with in increasing depth and reduces at the increasing radial distance from the cone shaft.; column 4 (Figure 1.3.3.8a), indeed, has the largest values of u_x.

Moreover, the perfectly rough model gives rise to u_x larger than the perfectly smooth case.

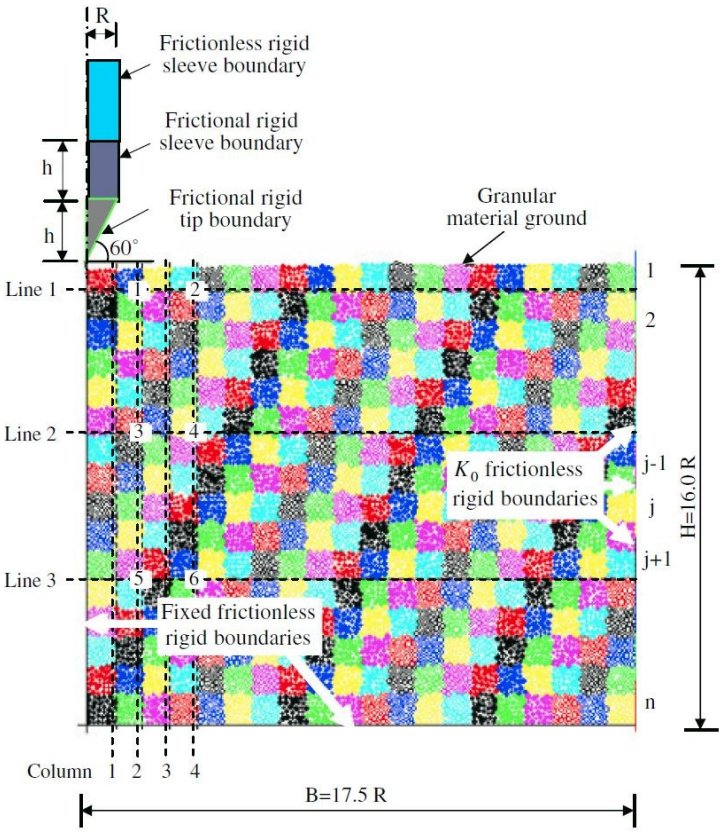

Figure 1.3.3.6. Geometry and boundary condition of CPT test model (Jiang *et al*., 2006)

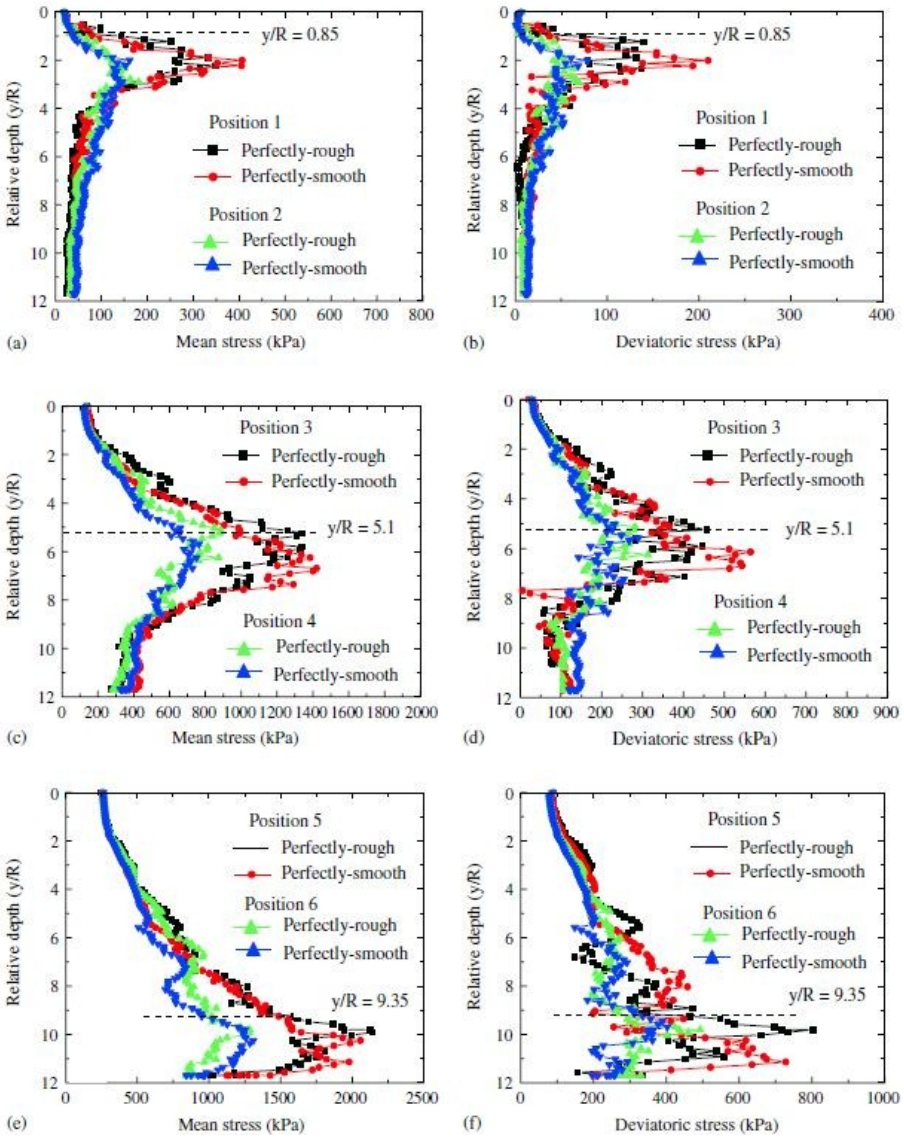

Figure 1.3.3.7. Mean and deviatoric stresses at the six control points for different stages of cone insertion (Jiang *et al*., 2006)

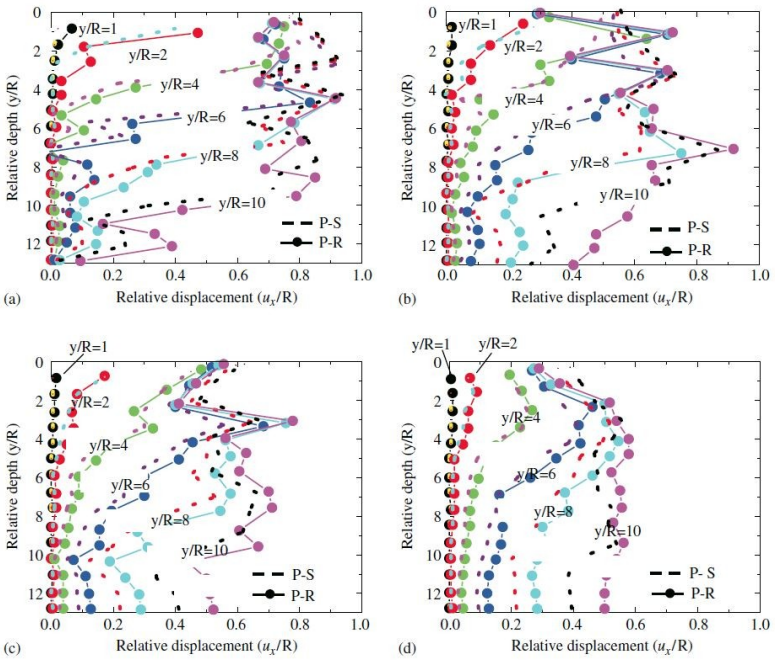

Figure 1.3.3.8. Horizontal deformations (Jiang *et al*., 2006)

Schmitt and Katzenbach (2006) simulate the effects of screw piles installation in sand by the continuum and discontinuum approaches.

Before performing the numerical analysis, the Authors gathered several data coming from test box filled with sand where different typologies of piles were installed in. During pile installation the change of horizontal stresses within the adjacent soil was recorded and soil density before and after the installation was investigated by CPT tests.

In the FE-model pile tip has a conical shape with diameter and length as the model pile (d_p = 22 – 28 cm, L_p = 2.8 m). The Drucker Prager / Cap model implemented in the code *ABAQUS* has been used. Since pile installation gives rise to soil horizontal displacements which cause a soil state variation, both in terms of relative density and horizontal stress, the modified horizontal stress state is simulated by considering a modified lateral earth pressure coefficient ranging from 1.0 to 1.2.

The installation process is simulated by the excavation of soil according to pile dimension, successively this hole is filled with elements that exert the liquid concrete pressure and the soil is allowed to expand or relax. When this

phenomenon is over, concrete pressure is reduced to zero and pile elements assumed the final stiffness, so that the pile can be loaded.

The results from the FE-analysis and the experimental data for CFA and displacement piles, in terms of total, base and shaft resistance, respectively R, R_b and R_s, are in very good agreement (Figure 1.3.3.9).

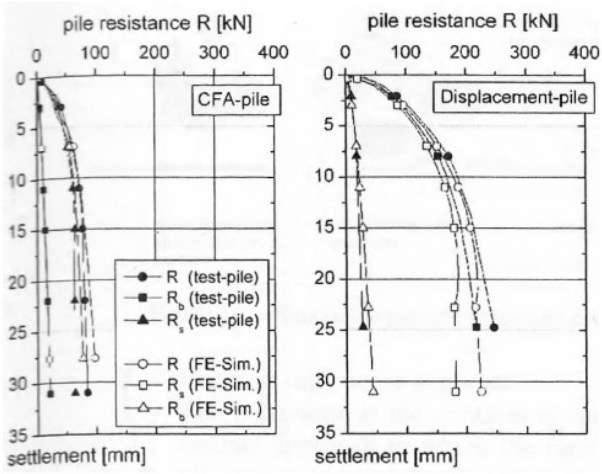

Figure 1.3.3.9. Comparison FE-simulation and test measures (Schmitt and Katzenbach, 2006)

In addition, a series of discrete numerical analyses are presented, where pile installation effects are simulated by using two different approaches. In the first one the model consists of a cubical arrangement of non-spherical particles where at the corner there is one quarter-shaft section of a pile (Figure 1.3.3.10-left). The shaft contact area within the soil body is defined by a control area (height 10 cm) where vertical and horizontal forces are monitored. Firstly, the pile is expanded from an initial very small diameter to a 10 cm diameter, in order to reproduce the increasing soil state which occurs during pile installation; at a later stage, it is pushed down for 1 cm in a sand with a confining pressure of 100 kPa.

Particles have a mean diameter of 6 mm and initial porosity is 0.346, which corresponds to a medium dense sand, and particle/particle friction coefficient μ_w is assumed to be 0.25 or 0.50.

In the second approach the installation process is simulated in a the testing box with size of 1 m x 0.75 m x 0.05 m (Figure 1.3.3.10-right), which is filled with non spherical particles whose size and distribution is the same as

before; the pile is rectangular and the overburden pressure is reduced to 25 kPa.

The horizontal stresses measured in the control volume at different distance from pile axis are reported in Figure 1.3.3.11 for both approaches.

It is evident that for the increasing horizontal displacement there is an increasing horizontal stress, which assumes the highest value in the control volume closer to the pile. For the first approach, at the end of displacement, in the borehole a concrete pressure is applied ($\sigma_{concrete}$ = 125 kPa) which gives rise to a reduction of measured stress state, even though it remains higher than the initial condition (confining pressure of 100 kPa). The greater is the horizontal displacement that pile installation induces in the soil the higher is the value of shaft friction, because relative density becomes higher and higher (Figure 1.4.3.11-left.). For the second approach, instead, the measured horizontal stress still increases with displacement, but reaches lower values than the first approach and has a stronger decrease at concreting stage, because the box is larger and the board is further from the pile, so it exerts less influence on the stress state (Figure 1.4.3.11-right.).

As to shaft resistance, it increases with the level of displacement mobilisation and with the increasing interparticle friction angle (Figure 1.4.3.12).

For the second approach the shaft resistance is as qualitative as the previous case: q_s increases at increasing horizontal displacement for an assigned value of the inter-particle friction angle (Figure 1.4.3.13).

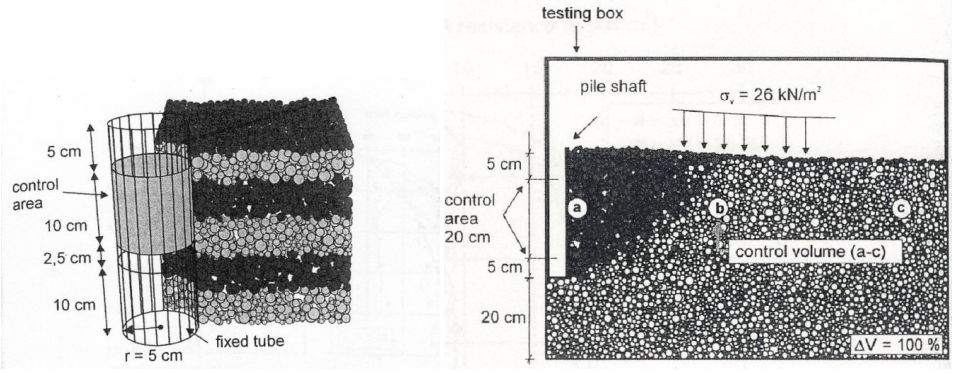

Figure 1.3.3.10. Discrete modelling of pile installation: first approach –left- second approach –right- (Schmitt and Katzenbach, 2006)

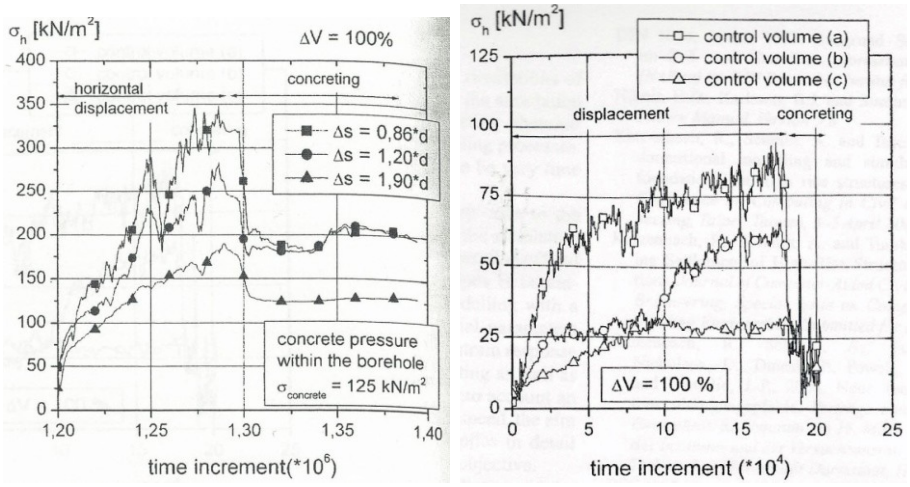

Figure 1.3.3.11. Horizontal stress during displacement and concreting phase for first – left- and second approach –right- (Schmitt and Katzenbach, 2006)

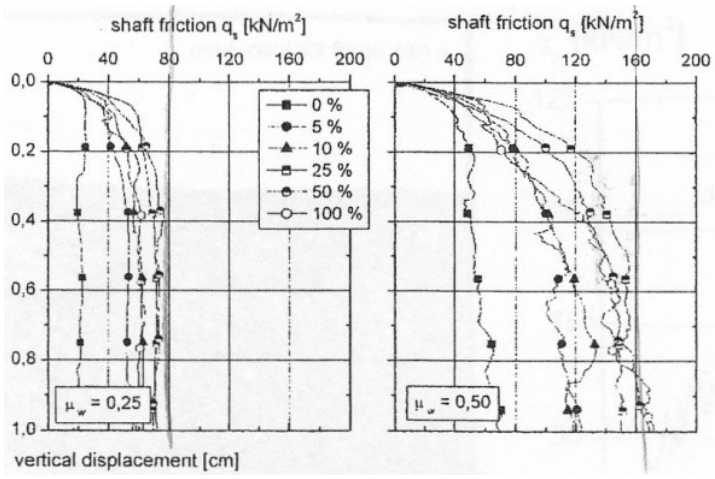

Figure 1.3.3.12. Measured shaft friction by DE-simulation- first approach for different interparticle friction angles (Schmitt and Katzenbach, 2006)

Porosity variation during the horizontal displacement is measured for both approaches within control volumes placed at increasing distance from pile axis. The first model presents a reduction of porosity in every control volume; in particular this reduction $\Delta n < 0$ decreases with the increasing distance from the pile and at a volume variation $\Delta V \approx 70\%$ soil starts to dilate (Figure 1.3.3.14). As far as the second approach concerns, only for the volume closer to the pile

shaft, there is a reduction of porosity, but also in this case at a percentage of displacement of about 75% soil starts to dilate. The other two control points, instead, record an increasing porosity during the whole installation process.

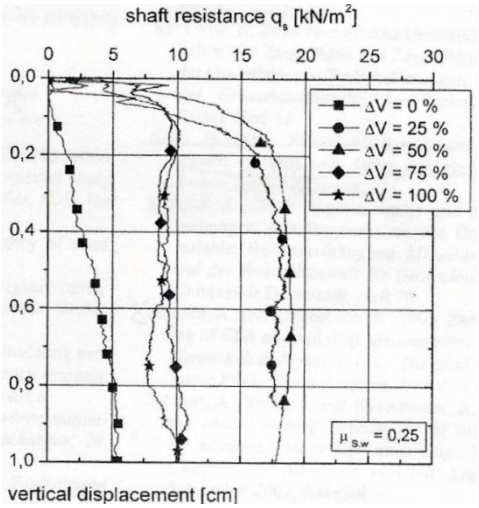

Figure 1.3.3.13. Measured shaft friction by DE-simulation – second approach (Schmitt and Katzenbach, 2006)

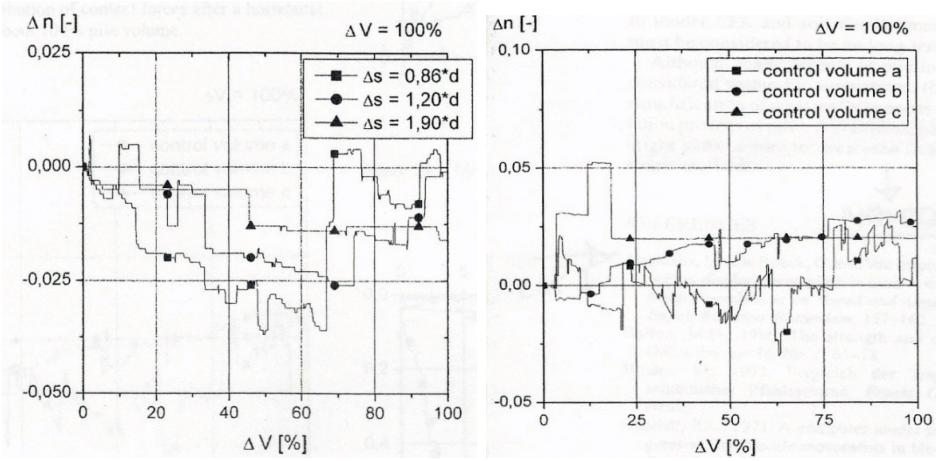

Figure 1.3.3.14. Change of porosity during horizontal displacement for first approach – left- and second approach –right- (Schmitt and Katzenbach, 2006)

Unfortunately, for the second model the stress and porosity measurements are recorded in three control volumes whose distance from the pile is not indicated.

Pucker *et al*. (2012) simulate the drilling process of a full displacement pile (FDP) by a 3D finite elements model. The perforation tool is a rigid body with the diameter of the displacement body of 51 cm and of 32 cm at the rod; the auger has the same diameter as the body and the tip is conical instead of flat (Figure 1.3.3.15). The pile penetrates in soil volume with a height of 20 m and a diameter d_p of 16 m; on the top of soil section there is a void area with a height of 2 m to make possible the displacement of soil during the drilling process. Friction angle at pile-soil interface δ is fixed at 1/3 φ' (the Authors do not specify what friction angle consider for numerical analyses).

Soil is modelled with a hypoplastic constitutive law with the extension of intergranular strain and the CEL-Method (Coupled Eulerian-Lagrangian Method) as contact algorithm, in order to overcome mesh distortion problems due to large deformation.

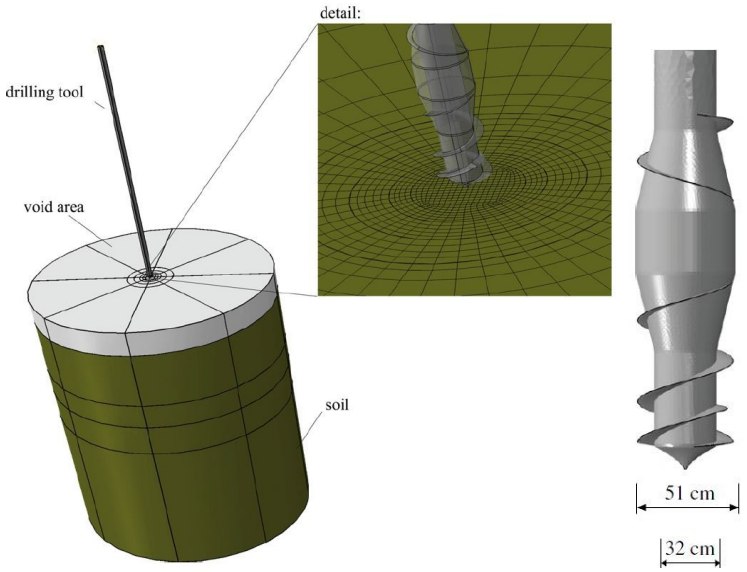

Figure 1.3.3.15. FE-model of FDP drilling process (Pucker *et al.*, 2012)

Simulations have been carried out in Mai Liao Sand model, with different initial relative density (D_R = 20, 50 and 80%) where pile is pushed by an

axial force and a rotation, considering the ratio between the vertical displacement and the rotation velocity v_z / v_r of 5 and 10, where $v_r = \omega_r d_p /2$.

For the elements rows at the distances of $1d_p$ and 3 d_p from the pile the horizontal stresses during perforation have been calculated for different values of relative density and velocity ratio. Figures 1.3.3.16 and 1.4.3.17 show the variation of σ_h at a penetration level $z/ d_p = 6$; it is evident that the closer is the measurement section the stresses are calculated at, the higher is their variation with respect to the geostatic stress state. It is quite worth noticing that σ_h has a very unstable distribution with depth, in particular the peak is reached in correspondence of the displacement body of the pile and below it there is a strong decrease of the stress which finally tends to the initial value. At different values of relative density the trend is the same and the absolute values of σ_h are more or less the same. For velocity ratio of 10, instead, the behaviour is the same, although there is a more evident difference among the stress variations at the different density states.

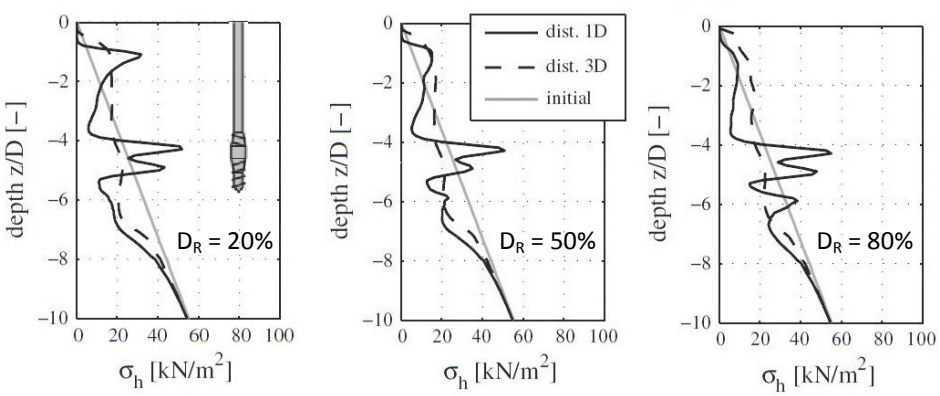

Figure 1.3.3.16. Variation of horizontal stress for velocity ratio v_r / v_z = 5 at different distances from pile axis (Pucker *et al.*, 2012)

In Figure 1.3.3.18 are reported the horizontal displacements of an elements row at the distance $2d_p$ from the pile during the insertion, for different porosities and ratio between vertical displacement and rotation velocity. For the case with $v_r/v_z = 5$ it is evident that the more is the initial relative density of the soil which the pile penetrates in, the less is the disturb this latter causes in terms of horizontal displacements.

However, if the pile penetrates with a higher velocity ratio ($v_r/v_z = 10$) the displacements are doubled.

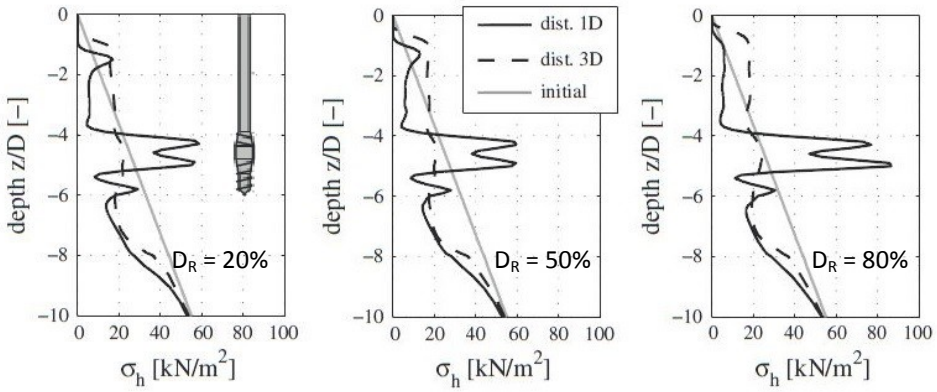

Figure 1.3.3.17. Variation of horizontal stress for velocity ratio v_r / v_z = 10 at different distances from pile axis (Pucker *et al.*, 2012)

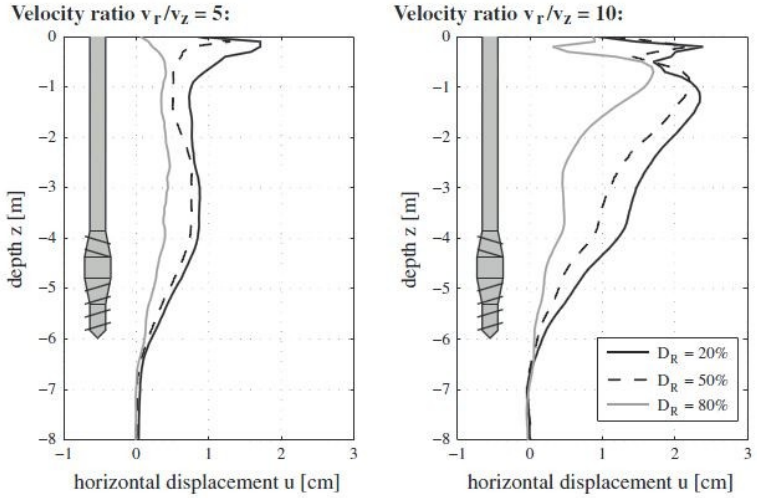

Figure 1.3.3.18. Horizontal displacements at a 2D distance from the pile at the end of penetration (Pucker *et al.,* 2012)

Besides, the Authors provide the variation of relative density calculated at three depths (1, 3 and 4.5 m) at the increasing horizontal distance from the pile during the installation process for the two different velocity ratios (Figure 1.3.3.19). For every case the relative density D_R(%) in correspondence of pile-soil interface decreases at first, then begins to increase and reaches a peak value

from a distance from the pile of about $1d_p$ to $2d_p$, and, afterwards, it starts decreasing till it reaches the initial value at a $7d_p$ distance from the pile.

For the case with the highest velocity ratio the most densified zone is more spread than the lower velocity, from $1d_p$ to $2d_p$ distance from the pile.

However, it is not quite clear how the soil could reach value of D_R higher than 100% as for the case with D_{R0} = 80%.

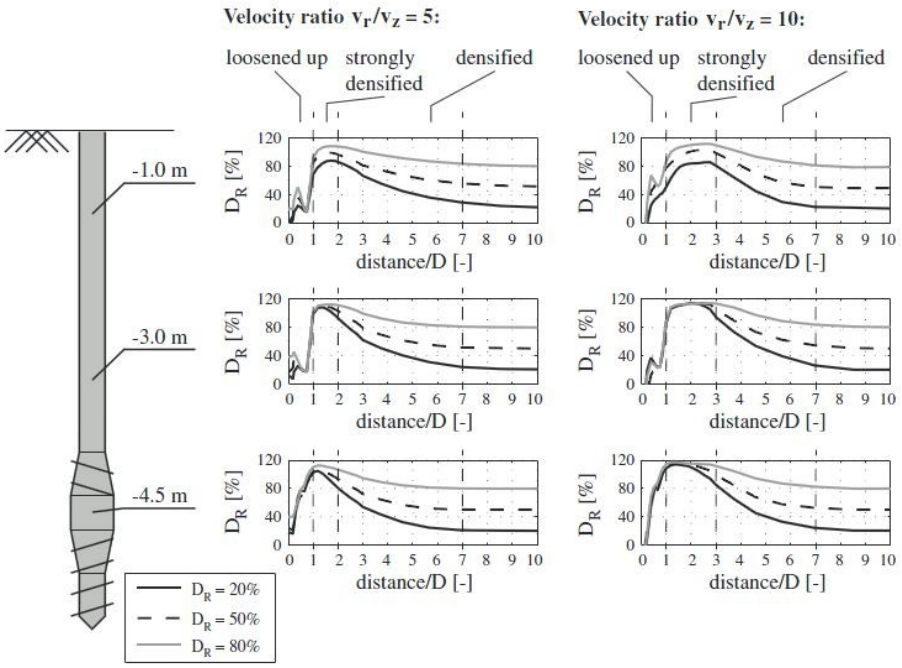

Figure 1.3.3.19. Variation of D_R(%) at three depths after the drilling process at increasing distances from the pile (Pucker *et al*., 2012)

During the penetration process, installation parameters have been calculated too, in particular reaction force and moment for both the velocity ratios considered (Figure 1.3.3.20). Concerning the reaction force, it increases at increasing relative density and decreases at increasing velocity ratio, in particular, for the case with v_r / v_z = 10, the force is about the same for different D_{R0} values. The moment, as the force, depends on D_R, but does not vary if there is a variation of velocity ratio. Hence, it seems that if the velocity ratio increases too much soils with different initial conditions assume the same response, because the pile installation destroy them.

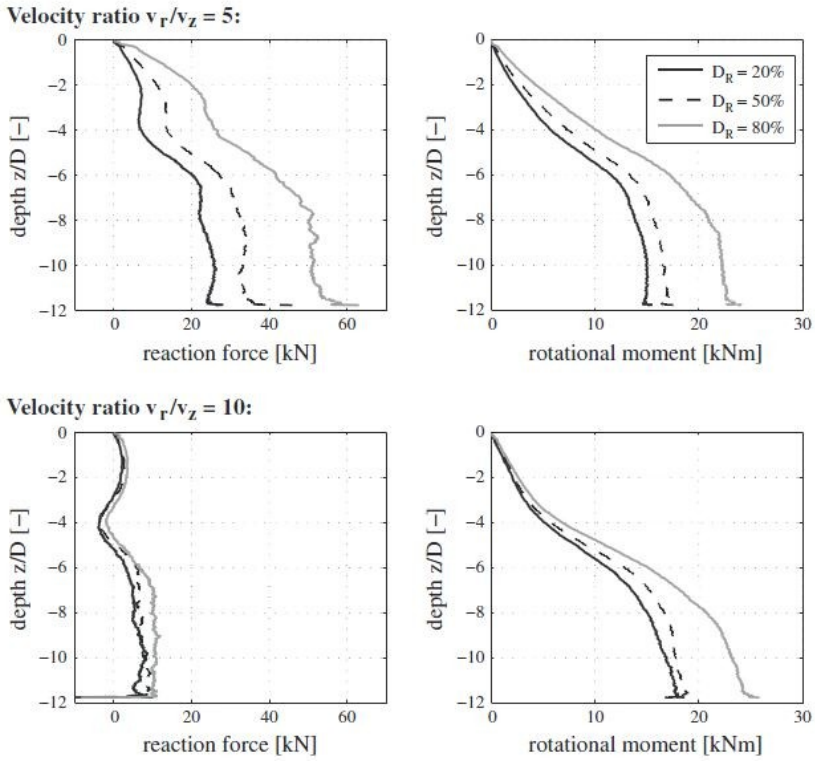

Figure 1.3.3.20. Reaction forces and rotational moments during FDP perforation in different soils with different velocity ratios (Pucker *et al*., 2012)

Zhou *et al*. (2012) present the results of the simulations of centrifuge tests performed by discrete element model and a coupled approach DEM+FEM with which they provide the variations of porosity during the displacement pile installation process.

The model has dimensions of 625 x 625 x 900 cm^3; it consists of a central nucleus of 26700 discrete non-circular particles and a boundary chamber with 21280 eight-node hexahedral elements; the pile is a stiff wall, with a diameter of 25 cm and length 400 cm (L_p/d_p = 16), that penetrates with a constant rate in the discrete soil. The particulate domain has a diameter 3.5 times and a length 1.8 times greater than the pile one.

As it can be noticed in Figure 1.3.3.21, first of all, both methods give the same results, from a qualitative point of view. Below the pile tip there is a high density core ($\Delta n < 0$), beyond which porosity gradually increases; above the

base, instead, at pile-soil interface porosity increases because of the pile-particles sliding mechanism, therefore dilatancy occurs, but also in this case there is a distance from which porosity starts to decrease. Figure 1.3.3.22 shows how the particle-particle and particle-pile contacts are distributed at three levels of pile insertion (S/d_p = 0.2, 0.7 and 1) both for DEM approach and coupled approach.

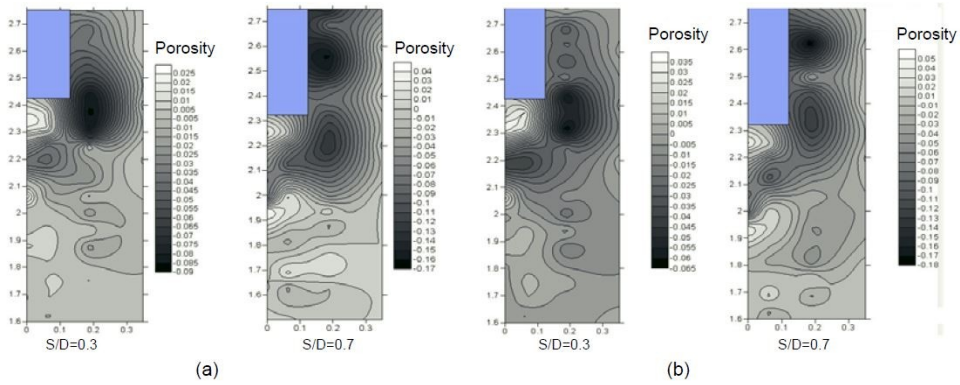

Figure 1.3.3.21. Distributions of porosities for coupled approach (a) and discrete approach (b) at two penetration steps (Zhou *et al*., 2012)

At the pile base the contact forces assume the highest values and, then, they spread to the pile side assuming the typical shape of the influence volume at the base of a pile under axial loads. For the discrete approach the contact forces chains appear to spread wider with respect to the coupled approach; for this latter, instead, the contact forces are higher on the pile surface. The Authors provide also the displacements of four traced particles along the principal directions and z during the penetration, in order to understand how the process of the pile installation influences the sand it passes through (Figure 1.3.3.23). From the comparison among the particles 1, 3 and 4 that are under the pile base at an increasing distance from the symmetry axis and between particles 1 and 2, which are underneath the tip at two different depths, it is evident that the particles just below the base are essentially unmoved in the horizontal directions, but have the highest displacement in the vertical direction; particle 1 has the highest value of vertical displacement just because it is closer to the pile tip (Figure 1.3.3.24).

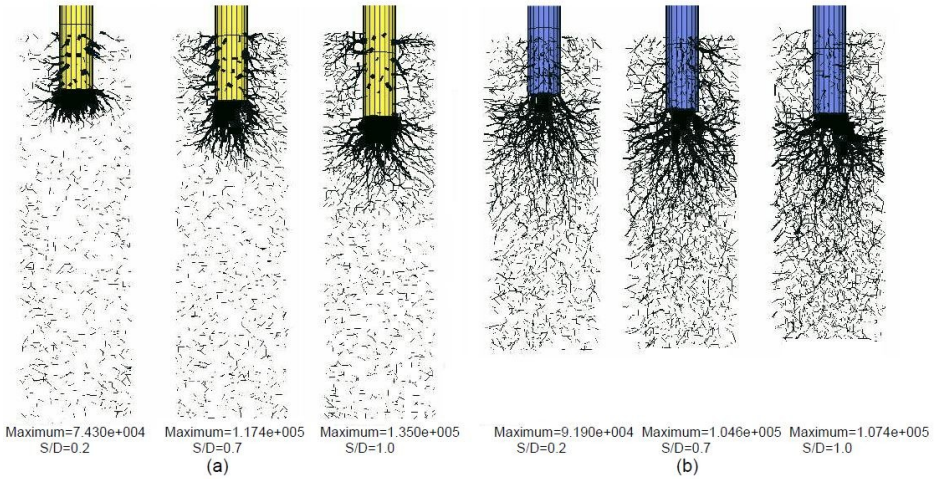

Figure 1.2.3.22. Distributions of contact forces for coupled approach (a) and discrete approach (b) at three penetration steps (Zhou *et al.*, 2012)

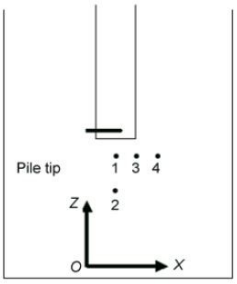

Figure 1.3.3.23. Position of four traced particles below pile tip (Zhou *et al.*, 2012)

Besides, particle 3 (which is below the corner of pile base) has an higher horizontal displacement than the particle 4 that lies at its side and which is almost unmoved.

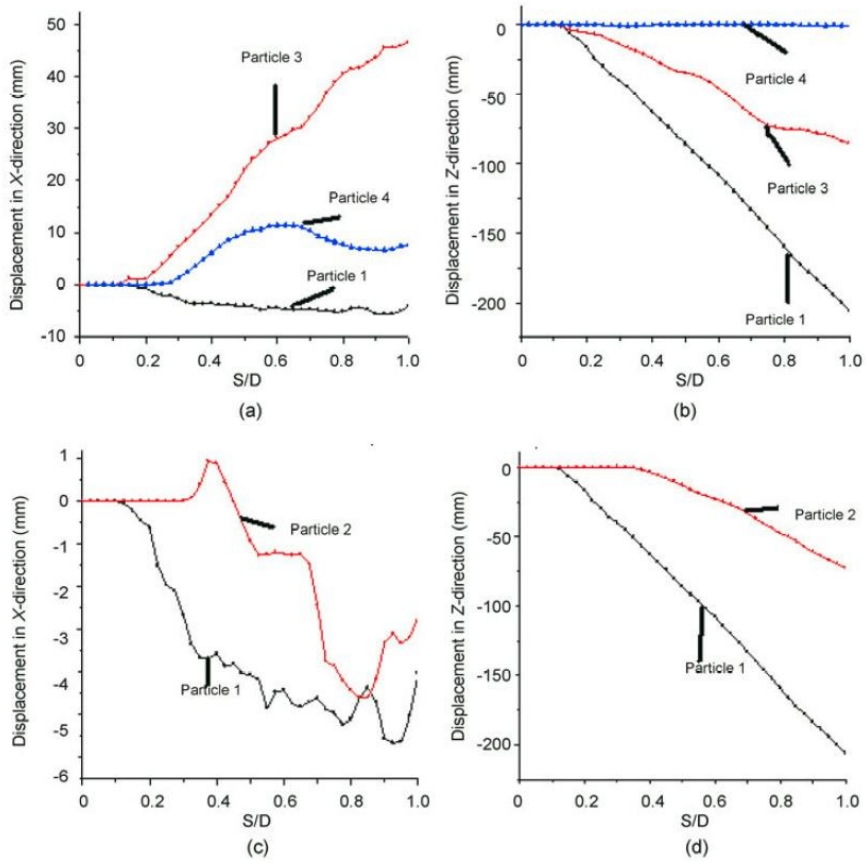

Figure 1.3.3.24. Displacement of traced particles along the principal axes (Zhou et al., 2012)

1.4. Concluding remarks

In this Chapter an attempt has been made to shed light on the fundamental aspects related to prediction and performance of axially loaded piles in granular soils.

Nowadays, soil state variations that occur during the loading stage are quite clear; nonetheless, the current design methods rely (above all) on empirical correlations based on the interpretation of in situ loading tests performed on instrumented piles.

Among the others, because of the geometric similarity between cone and jacked pile, a wide scenery of the design methods from CPT data is considered. The several methods reported in this Chapter provide empirical correlations hailing from the interpretation of experimental data gathered from all over the world and give very different indications from each others. Moreover, care must be taken in data extrapolation from these correlations to pile types and soil conditions outside the reference database.

Aiming to improve the knowledge about the mechanisms occurring during pile installation and their influence on pile response under axial loads, loads of experimental, theoretical and numerical studies have been carried out.

As to the experimental approach, centrifuge and field tests represent a very valid contribute to determine the variation and the distribution of stresses during the installation of jacked piles in sand. Unfortunately, these kinds of test are very expensive, therefore it is necessary to couple the experimental phase with the numerical analysis.

The numerical efforts that have been made so far are quite few, because of the complexity in simulating phenomena which cause such large deformations as pile installation.

The Finite Element Model requires the use of sophisticated mesh models, simplified geometries and reduced friction at interface, in order to ensure the numerical stability. The few works presented above about jacked pile installation give qualitative indications about the stress distributions, albeit, as a matter of fact, these refer just to the base mechanisms.

The numerical analysis of the full displacement pile installation by FEM are very interesting, even though they refer only to the insertion stage of the installation process.

As for the Discrete Element Model approach, the analysis of displacement pile installation is still at an initial stage, in which the more significant efforts have been concentrated above all on the CPT simulations. The very few studies about pile installation do not refer explicitly to the actual installation process and do not make reference to the stress state at both pile base and shaft.

It is evident that enhances for pile installation modelling are required.

In this work of Thesis the discrete approach has been chosen for modelling the installation and loading process of displacement piles realized in sand by different technologies. In the next chapter the theoretical basis of the Discrete Element Method will be presented.

CHAPTER 2. DISTINCT ELEMENT METHOD: THEORETICAL BASIS

2.1. Introduction

Cundall and Strack proposed for the first time the basic formulation for the Distinct Element Model (DEM) to the US National Science Foundation in 1978 and then they published it on the journal Géotechnique in 1979.

The model consists in the schematization of a medium as an agglomerate of individual particles, therefore it can simulate soil and other granular materials. The DEM explicitly considers the interactions among the single particles, the relative movements and rotations, and this aspect represents the most important feature and also the most evident difference with respect to the continuum model. In the continuum model the soil is assumed to be a continuum material which needs sophisticated constitutive models to describe the behaviour of its particulate nature; on the other hand, in DEM the particulate soil is explicitly used and, even if simple numerical models are considered, the mechanical response of the actual soil can be reproduced.

The scheme of calculation is a very simple loop: the user gives an input (generally an acceleration) to the system giving rise to a motion to the particles which change their position, thus upgrading their contact; changing contacts causes also a change in force acting on each particle, therefore the bodies undergo a further motion.

The assumptions typically made in particle-based DEM simulations can be stated:

- The basic particles are rigid, they possess a finite inertia and can be analytically described.
- The particles can move independently from each other, can translate and rotate.
- The program automatically identifies new contacts between particles.

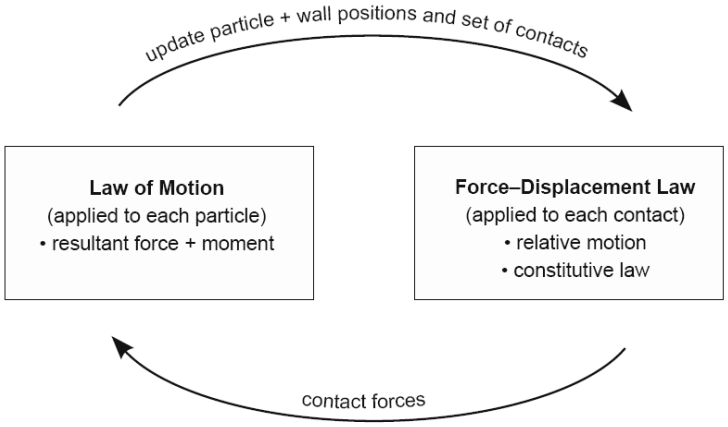

Figure 2.1.1. Calculation scheme

- The contact between particles occurs over an infinitesimal area and each contact involves only two particles.

- The particles are allowed to overlap slightly at the contact points and this overlap is analogous to the deformation that occurs between real particles. The magnitude of the deformation of each particle at the contact point is assumed to be small with respect to the particle size.

- The compressive inter-particle forces can be calculated from the magnitude of the overlap.

- At the contact points, it is possible for particles to transmit tensile and compressive forces in the contact normal direction as well as a tangential force orthogonal to the normal contact force.

- Tensile inter-particle forces can be calculated by considering the separation distance between two particles. Once the tensile force exceeds the maximum tensile force admitted for the contact, the particles can move away from each other, the contact is deleted and no longer considered when calculating the contact forces.

- The time increment chosen in a DEM simulation should be small enough that the motion of the particle over a given time step is sufficiently small to only influence its immediate neighbouring particles.

- Agglomerates of the rigid base particles can be used to represent a single physical particle, and the relative motion of these base particles within the agglomerate may cause a measurable deformation of the composite particles. Alternatively there agglomerates may themselves be rigid.

2.2. Contact mechanics

The mechanics of contacts among the particles, which the agglomerate consists of, is the base of the distinct element model. Two particles are in contact when the distance between their centroids is equal or minor of the sum of radius (Figure 2.2.1.).

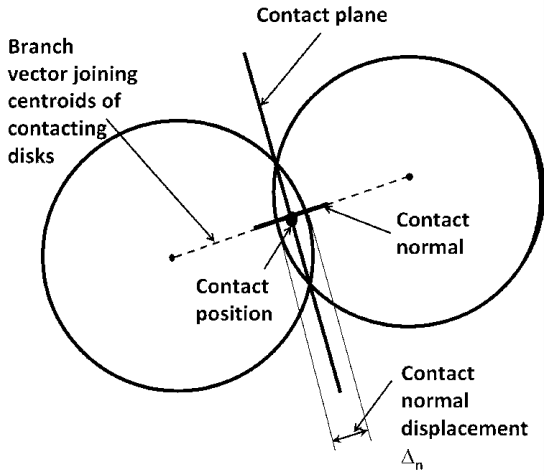

Figure 2.1.1. Contact scheme

DEM analysis considers the dynamic interacting particles, therefore the basic principles are introduced by directly considering the dynamic equilibrium of the individual particles. In Cundall and Strack's approach, indeed, the solution of the global system of equations is avoided by considering the dynamic equilibrium of the individual particles rather than solving the entire system

simultaneously (explicit approach). Referring to Zhu *et al*. (2007) probably the most general format for expressing the equation governing the translational dynamic equilibrium of a particle *p* with mass m_p is

$$m_p \ddot{\mathrm{u}}_\mathrm{p} = \sum_{\mathrm{c}=1}^{\mathrm{N\,c,p}} \mathrm{F}_\mathrm{pc}^\mathrm{con} + \sum_{\mathrm{j}=1}^{\mathrm{N\,nc,p}} \mathrm{F}_\mathrm{pj}^\mathrm{non-con} + \mathrm{F}_\mathrm{p}^\mathrm{g} + \mathrm{F}_\mathrm{p}^\mathrm{app} \tag{2.2.1}$$

where $\ddot{\mathrm{u}}_\mathrm{p}$ is the acceleration vector, $\mathrm{F}_\mathrm{pc}^\mathrm{con}$ are the contact forces due to contact *c* when there are $\mathrm{N}_\mathrm{c,p}$ contacts between particle *p* and either other particles or boundaries, and $\mathrm{F}_\mathrm{pj}^\mathrm{non-con}$ are no-contact forces between particle *p* and $\mathrm{N}_\mathrm{nc,p}$ other particles or boundaries; $\mathrm{F}_\mathrm{p}^\mathrm{g}$ is the body force and $\mathrm{F}_\mathrm{p}^\mathrm{app}$ is the applied load.

Concerning the rotational dynamic equilibrium, the torque generated at each contact point is calculated as the product of the contact force and a vector from the centroid of the particle to the contact centre:

$$I_p \frac{d\omega_p}{dt} = \sum_{j=1}^{N_{mom}} M_{pj} \tag{2.2.2}$$

where ω_p is the angular velocity, I_p the inertia and M_{pj} the moment applied by the j_{th} moment transmitting contact forces involving particle p.

In particular, simplifying the equation (2.2.1) it follows that:

$$m_p \ddot{\mathrm{u}}_\mathrm{p} = \mathrm{F}_\mathrm{p}^\mathrm{t} \tag{2.2.3}$$

with $\mathrm{F}_\mathrm{p}^\mathrm{t}$ as the resultant forces vector of the single particle; applying a central difference time integration approach with a time increment Δt, the acceleration at the time t is

$$a_p^t = \frac{1}{\Delta t}(v_p^{t+\Delta t/2} - v_p^{t-\Delta t/2}) \tag{2.2.4}$$

with the velocity vector v_p. The velocity at the time t+Δt/2 is calculated as

$$v_p^{t+\Delta t/2} = v_p^{t-\Delta t/2} + \Delta t m_p^{-1}(F_p^t) \tag{2.2.5}$$

In this way it is possible to calculate the updated position of the particle:

$$x_p^{t+\Delta t/2} = x_p^t + \Delta t \cdot v_p^{t+\Delta t/2} \qquad (2.2.6)$$

where the position vector components are the Cartesian coordinates and the total rotation with respect to the principal axes of the ball.

It is important to underline that, in this kind of simulation, time is discretized, therfore the analysis does not capture the real continuous physical changing of the system. Moreover, the model considers only the first derivate at time t in the prediction (this approximation is called “truncation error”).

2.3. Contact forces

In distinct element model interacting and potentially interacting particles are considered.

When two bodies are in touch they can share a contact point or a contact area; it depends on the particles’ shapes and their surfaces. For these reasons the contact types are distinguished into two categories: conforming contact or non-conforming contact.

The former occurs when the particles’ surfaces perfectly fit together, while the second one will initially contact in a single contact point.

As illustrated in Figure 2.3.1 particles with the most common and simplest shape (disks for 2D and spheres for 3D) have non-conforming contact.

When two particles come into contact they are allowed to overlap (*soft approach*) and because of this overlapping contact forces will born. In compression the normal inter-particle force acts to repulse the two contacting bodies, while, in case of separation, tensile forces occur to draw the particles up.

Hence, contact forces represent the integral of the real stresses acting along a physical contact and they are calculated as

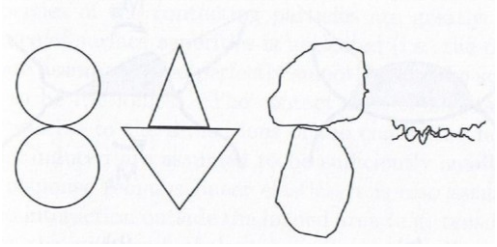

Figure 2.3.1. Conforming and non-conforming contacts

$$F_N = \int f_N \, dA \quad \wedge \quad F_S = \int f_S \, dA \tag{2.3.2}$$

where f_N and f_S are the normal and the tangential components of the surface forces per unit area, respectively.

The contributions of the two bodies will be equal in magnitude, but with opposite verse.

In case of non-circular or non-spherical particles the contact normal forces can give them a rotation and also resist to the one which is imparted by tangential forces.

These forces are calculated introducing virtual springs, normal and tangential, at the contact points. The springs have a force-deformation relationship, that is called "*Contact Constitutive Model*".

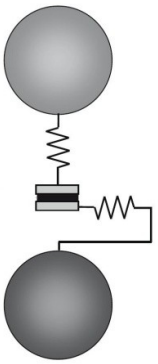

Figure 2.3.2. Contact model

In literature there are several models that describe the relationship between contact forces and overlapping (e.g. O'Sullivan, 2011); generally they come from rheological models, indeed there are:

- Elastic linear model
- Elastic non-linear model
- Viscous model
- Rigid perfectly plastic model

Herein, only the elastic linear constitutive model is reported, since it will be used in the following study. This is, without a doubt, the most common and the simplest constitutive model that calculates the contact normal force as

$$F_N = K_N \cdot \delta_N \tag{2.3.2}$$

where K_N is the contact stiffness in the normal direction and δ_N is the overlap at the contact point, measured at the direction orthogonal to the contact. The vector of this force lies on the line joining the centroids of the contacting particles.

The normal and tangential contact stiffness depends on the single particle stiffness and it is calculated as:

$$K_N^c = \frac{\prod_{i=1}^{p} k_n}{\sum_{i=1}^{p} k_n}$$
$$K_s^c = \frac{\prod_{i=1}^{p} k_s}{\sum_{i=1}^{p} k_s} \tag{2.3.3}$$

If the material is not cemented or bonded there is no need to calculate tension across the contact, therefore when the contacting particle drift away from each other the contact is considered broken.

The maximum shear contact force follows the Mohr-Coulomb's resistance criterion

$$F_{S,max} = F_N \cdot \mu = F_N \cdot \tan\varphi_\mu \tag{2.3.4}$$

where φ_μ is the interparticle friction angle; if the contact is subjected to a shear force higher than $F_{S,max}$ then the contact gets lost.

Eventually, this kind of model cannot reproduce the energy dissipation that occurs with the yielding. In order to simulate this dissipation it is used to consider a local non-viscous damping which is proportional to the out-of-balance force with a sign that ensures that the vibrational modes of each particle are damped. This means that, when the particle has not equilibrium because of an acceleration, it is possible to reach the equilibrium applying a damping force opposite to the verse of the acceleration (Cundall, 1987).

Referring to Itasca (2004), the damping force is given by:

$$F_d = -\alpha^* |F^p| sign(v^p) \tag{2.3.5}$$

where F^p is the resultant or out-of-balance force action on particle p, sign(v^p) is the sign of the velocity vector v^p for particle p and a^* is the damping coefficient (default value of 0.7).

2.3.1. Measurement of stresses

Stresses and strains are continuum parameters which cannot be computed in a discrete medium. Nonetheless, they are useful to understand soil behaviour, as a consequence, it is necessary to adopt averaging procedures in order to switch from the microscale to the continuum.

In literature there are several approaches to determine expressions for the stress parameter, the most common are: (a) stresses calculated by integration of forces along boundary; (b) local stresses calculated from particle stresses; (c) local stresses calculated from contact forces.

In this work the distinct element software **Particle Flow Code 3D (Itasca, 2005)** has been used; it implements the Cundall and Strack's model and computes the average stress $\bar{\sigma}_{ij}$ in a volume *V* of material

$$\bar{\sigma}_{ij} = \frac{1}{V}\int_V \sigma_{ij} dV \qquad (2.3.1.1)$$

where $\bar{\sigma}_{ij}$ is the stress acting throughout the measurement volume. The code allows to model the particles by spheres or clumps, that are agglomerates of spheres; thus, the integral can be replaced by a sum over the N_p particles and N_l clumps contained within *V* as

$$\bar{\sigma}_{ij} = \frac{1}{V}\left(\sum_{\mathrm{N_p}} \bar{\sigma}_{ij}{}^{(\mathrm{p})}\mathrm{V}^{(\mathrm{p})} + \sum_{\mathrm{N_l}} \bar{\sigma}_{ij}{}^{(\mathrm{l})}\mathrm{V}^{(\mathrm{l})}\right) \qquad (2.3.1.2)$$

where $\bar{\sigma}_{ij}{}^{(p)}$ and $\bar{\sigma}_{ij}{}^{(l)}$ are the average stresses in particle and clump, respectively. If the single body b is considered, the formulation for the stress is the same

$$\bar{\sigma}_{ij}^{(\mathrm{b})} = \frac{1}{V^{(\mathrm{b})}}\int_{V^{(\mathrm{b})}} \bar{\sigma}_{ij}^{(\mathrm{b})} dV^{(\mathrm{b})}, \mathrm{b} = \{p, l\} \qquad (2.3.1.3)$$

Considering the identity

$$S_{ij} = \delta_{ij} S_{kj} = x_{i,k} S_{kj} = \left(x_i S_{kj}\right)_{,k} - x_i S_{kj,k} \tag{2.3.1.4}$$

and applying it to the stress in each body, one can write

$$\begin{aligned} \bar{\sigma}_{ij}^{(\mathrm{b})} &= \frac{1}{V^{(\mathrm{b})}} \int_{V^{(\mathrm{b})}} \left[\left(x_i \sigma_{kj}^{(\mathrm{b})} \right)_{,k} - x_i \sigma_{kj,k}^{(\mathrm{b})} \right] dV^{(\mathrm{b})} \\ &= \frac{1}{V^{(\mathrm{b})}} \left\{ \left(I_{ij}\right)_1 - \left(I_{ij}\right)_2 \right\}, \mathrm{b} = \{p, l\} \end{aligned} \tag{2.3.1.5}$$

where the first integral $I_{ij,1}$ is rewritten as a surface integral

$$\begin{aligned} \left(\mathrm{I_{ij}}\right)_1 &= \int_{V^{(\mathrm{b})}} \left[\left(x_i \sigma_{kj}^{(\mathrm{b})} \right)_{,k} \right] dV^{(\mathrm{b})} = \int_{S^{(\Phi)}} \left[\left(x_i \sigma_{kj}^{(\mathrm{b})} \right)_{,k} \right] n_k dS^{(\mathrm{b})} \\ &= \int_{S^{(\Phi)}} \mathrm{x_i t_j}^{(\mathrm{b})} \mathrm{dS}^{(\mathrm{b})}, \mathrm{b} = \{\mathrm{p}, \mathrm{l}\} \end{aligned} \tag{2.3.1.6}$$

$S^{(b)}$ is the body surface, n_k is the unit outward normal to the surface and $t_j^{(b)}$ is the traction vector; the term $\left(x_i \sigma_{kj}^{(\mathrm{b})} \right)$ is assumed to be continuously differentiable. If the moment carried by each parallel bond is neglected, then each body is loaded by point forces acting at discrete contact locations, and the above integral can be replaced by a sum over the $N_c^{(b)}$ contacts as

$$\left(I_{ij}\right)_1 = \sum_{N_c^{(\mathrm{b})}} x_i^{(c)} F_j^{(c,\mathrm{b})}, \mathrm{b} = \{p, l\} \tag{2.3.1.7}$$

where $x_i^{(c)}$ is the location and $F_j^{(c,b)}$ is the force acting on the body (b) at the contact (c).

The location can be rewritten as

$$x_i^{(c)} = x_i^{(\mathrm{b})} + \left(x_i^{(c)} - x_i^{(\mathrm{b})} \right), \mathrm{b} = \{p, l\} \tag{2.3.1.8}$$

where $x_i^{(b)}$ is the position of the body centroid. By substituting Eq. (2.3.1.8) into Eq. (2.1.3.7)

$$\left(I_{ij}\right)_1 = \sum_{N_c^{(\mathrm{b})}} x_i^{(\mathrm{b})} F_j^{(c,\mathrm{b})} + \sum_{N_c^{(\mathrm{b})}} \left(x_i^{(\mathrm{c})} - x_i^{(\mathrm{b})} \right) F_j^{(c,\mathrm{b})}, \mathrm{b} = \{p, l\} \tag{2.3.1.9}$$

The second integral is dealt with as follows. In the absence of body forces and externally applied forces, the equation of motion for body (b) is

$$\sigma_{kj,k} = \rho a_j = \rho\left(\frac{F_i}{m}\right) = \frac{F_j}{V} \tag{2.3.1.10}$$

Where ρ is the density, a_j is the acceleration of the centroid and F_j is the resultant force acting at the centroid. This relation allows to write the second integral as

$$\begin{aligned}\left(I_{ij}\right)_2 = \int_{V^{(\mathrm{b})}} x_i \sigma_{kj,k}^{(b)} dV^{(b)} = \frac{F_j^{(b)}}{V^{(b)}} \int_{V^{(b)}} x_i dV^{(b)} = F_j^{(b)} x_i^{(b)}, \mathrm{b} \\ = \{p, l\}\end{aligned} \tag{2.3.1.11}$$

Substituting Eqs. (2.3.1.9) and (2.3.1.11) into Eq. (2.3.1.5) gives

$$\begin{aligned}\bar{\sigma}_{ij}^{(b)} = \frac{1}{V^{(b)}} \Bigg\{ \sum_{N_c^{(b)}} x_i^{(b)} F_j^{(c,b)} \\ + \sum_{N_c^{(\phi)}} (x_i^{(c)} - x_i^{(b)}) F_j^{(c,b)} - F_j^{(b)} x_i^{(b)} \Bigg\}, \mathrm{b} = \{p, l\}\end{aligned} \tag{2.3.1.12}$$

where the first and third terms can be canceled because $F_j^{(b)} = \sum_{N_c^{(b)}} F_j^{(c,b)}$, so that

$$\bar{\sigma}_{ij}^{(b)} = \frac{1}{V^{(b)}} \sum_{N_c^{(b)}} \left(x_i^{(c)} - x_i^{(b)}\right) F_j^{(c,b)}, \mathrm{b} = \{p, l\} \tag{2.3.1.13}$$

The body needs not to be in static equilibrium, but there should be no body forces and no externally applied forces acting on the body.

An expression for the average stress in a volume, *V*, is obtained by substituting Eq. (2.3.1.13) into Eq. (2.3.1.12). However, definition of the volume in the resulting expression is problematic because of the bodies that intersect the measurement region. The problem is overcome by noting that, in a

statistically uniform assembly, the volume associated with each body is $V^{(b)}/(1-n)$, such that

$$V = \frac{\sum_{N_p} V^{(p)} + \sum_{N_l} V^{(l)}}{1-n} \tag{2.3.1.14}$$

with n as the porosity of the region. The average stress in a measurement region is found by combining Eqs. (2.3.1.2), (2.3.1.13) and (2.3.1.14), to yield

$$\begin{aligned}\bar{\sigma}_{ij} &= \left(\frac{1-n}{\sum_{N_p} V^{(p)} \sum_{N_l} V^{(l)}}\right)\left(\sum_{N_p} \bar{\sigma}_{ij}^{(p)} V^{(p)} \sum_{N_l} \bar{\sigma}_{ij}^{(l)} V^{(l)}\right) \\ &= \left(\frac{1-n}{\sum_{N_p} V^{(p)} \sum_{N_l} V^{(l)}}\right)\left(\sum_{N_p}\sum_{N_c^{(p)}} \left(x_i^{(c)} - x_i^{(p)}\right) F_j^{(c,p)} + \sum_{N_l}\sum_{N_c^{(l)}} \left(x_i^{(c)} - x_i^{(l)}\right) F_j^{(c,l)}\right)\end{aligned} \tag{2.3.1.15}$$

where the summations are taken over the N_p particles and N_l clumps with centroids in the measurement region, and the various terms are defined:

- $V^{(b)}$ is the volume of body (b)
- n is the porosity of the measurement region
- $N_c^{(b)}$ is the number of contacts along the surface of body (b)
- $x_i^{(b)}$ and $x_i^{(c)}$ are the locations of a body centroid and its contact, respectively
- $F_j^{(c,b)}$ is the force acting on body (b) at contact (c), which includes both the contact and parallel-bond forces, but neglects the parallel-bond moment.

2.4. Porosity computation

The porosity n is defined as the ratio of total void volume, V^{void}, within the measurement-region volume, V^{reg}:

$$n = \frac{V^{void}}{V^{reg}} = \frac{V^{reg} - V^{mat}}{V^{reg}} = 1 - \frac{V^{mat}}{V^{reg}} \tag{2.4.1}$$

where V^{mat} is the volume of material in the measurement region. V^{mat} is approximated by

$$V^{mat} = \begin{cases} \sum_{N_{p'}} V^{(p')} + \sum_{N_l} V^{(l)} - \sum_{N_c} V^{(c)}, & B_v \neq 0 \\ \sum_{N_{p'}} V^{(p')} + \sum_{N_l} V^{(l)} - \sum_{N_c} V^{(c)} - \sum_{N_r} V^{(r)}, & B_v = 0 \end{cases} \tag{2.4.2}$$

where $N_{p'}$ is the number of particles not used by clumps that lie fully within or intersect the measurement region, and $V^{(p')}$ is the volume of the spherical particle p'; N_l is the number of clumps with centroids that lie in the measurement region, and $V^{(l)}$ is the clump volume given by

$$V^{(l)} = \begin{cases} \sum_{N_p} V^{(p)} - \sum_{N_r} V^{(r)}, & \mathrm{B_v} = 0 \\ V_l, & \mathrm{B_v} \neq 0 \end{cases} \tag{2.4.3}$$

with N_r clump-overlap regions with centroids in the measurement region, $V^{(r)}$ is the volume of clump-overlap region (r) taken as the overlap volume of the two disks or spheres defining the region and $\mathrm{B_v}$ is the volume-compute flag associated with each clump. The clump volume can be automatically determined based on the positions and radii of its constituent particles ($\mathrm{B_v} = 0$ – the default value), or it can be specified by the user as V_l.

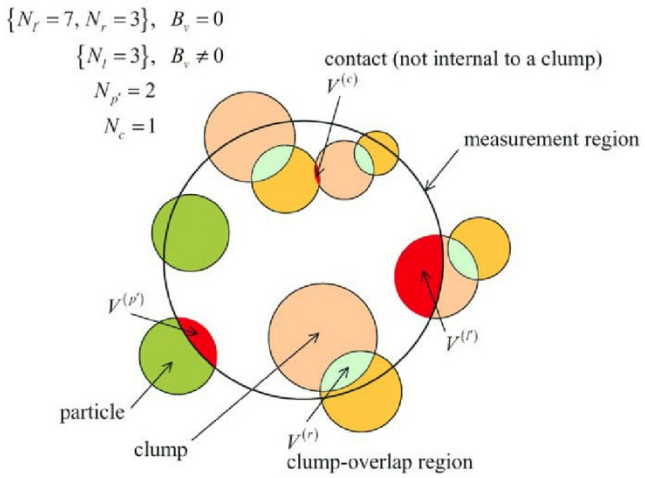

Figure 2.4. Relevant quantities for porosity computation in a mixed system (spheres and clumps)

CHAPTER 3. NUMERICAL MODEL CALIBRATION

3.1. Introduction

This Chapter concentrates on the numerical model calibration for the analysis of displacement pile installation into several steps.

At a first instance, the numerical analysis will start by studying the behaviour of soil samples through the modelling of laboratory triaxial tests with different initial conditions. Therefore, different stress paths are analysed to highlight the capability of the DEM to capture the actual behaviour of sand – contractive/dilative, critical state, dependence of the mobilized resistance from confinement stress and porosity -.

Afterwards, the installation problem will be approached by reproducing cone penetration tests, firstly at laboratory scale, successively in field.

Eventually, the CPT study will be developed and the installation process of a real pile in situ will be modelled.

3.2. Modelling the behaviour of soil samples under triaxial compression

The micromechanical parameters that govern the contact mechanics (interparticle friction angle, contact normal and shear stiffness) are not available in laboratory, as a consequence, it is strictly necessary to calibrate the soil model. The calibration phase is a very critical stage, because of the many differences between the modelled assembly and the actual soil volume (in terms of number of particles, particle shape and grain-size distribution) and the only one way to properly reproduce the material behaviour is the back-analysis of the experimental results.

Calvetti *et al.* (2003) calibrate the model of the dry dense Hostun sand by referring to the experimental data reported by Royis and Doanh (1998) for a single drained triaxial compression test performed at a confining stress p of 100 kPa. The Authors provide the set of the micromechanical parameters and kinematic constraints, determined by a trial and error procedure, which well-reproduce the response of the actual triaxial test.

The particulate model is performed with the three-dimensional distinct element code *Particle Flow Code 3D (PFC3D).* It consists of about 3500 particles contained in a cubical box with length 0.0045 m, whose three plates are fixed and three are used to apply loading conditions. This cubical sample is obviously a simplification of the real laboratory specimen, but it is considered sufficient to obtain a reliable qualitative and quantitative response of the material, so that its use is preferred because of the limited number of particles it contains (Figure 3.2.1).

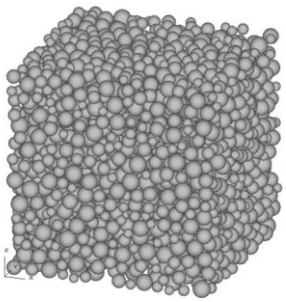

Figure 3.2.1. Cubical DEM sample for triaxial test

The particles are rigid weightless spheres with fixed rotation, in order to compensate the effect of the spherical shape which leads to unrealistically low mobilized stress ratios at ultimate failure (Calvetti, 2003). For the grain-size distribution, particles smaller than D_5 are neglected and the diameter range is from d_{min} = 0.00015 m to d_{max} = 0.00045 m, with a mean diameter d_{av} = 0.0003 m (Figure 3.2.2); the target porosity n is 0.42.

The specimen preparation follows the standard procedure:

- *Random generation of particles with a large prescribed porosity (in order to avoid a pre-stressed sample), a zero interparticle friction angle and a numerical damping of 70%. During this phase the plates are fixed, therefore the final confining stress is p = 0.*
- *Application of the isotropic compression p = 10 kPa, with the fixed interparticle friction and contact stiffness, the numerical damping is lowered to 10%.*

- *Progressive reduction of the interparticle friction angle at constant confining pressure, in order to decrease porosity from the input value to the target value.*
- *Simulation of the laboratory triaxial test performed in different initial conditions (porosity and confining stress) and calibration of the micromechanical parameters following a trial and error procedure.*

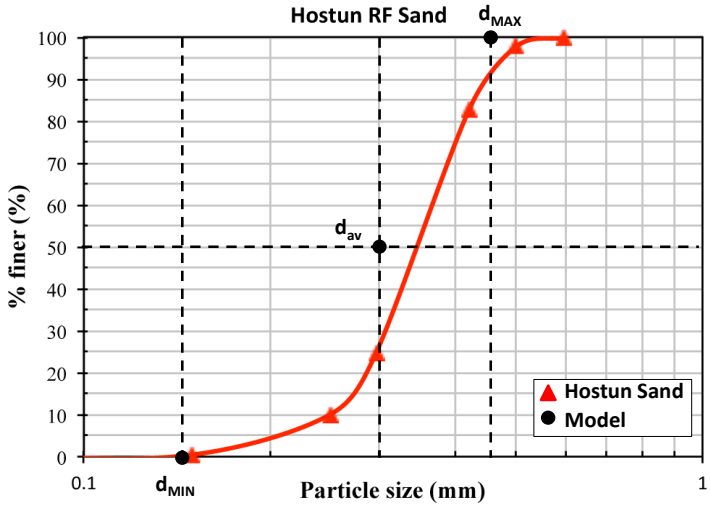

Figure 3.2.2. Grain size distribution for Hostun sand

The micromechanical parameters, carried out from the trial and error simulations, guarantee a good agreement between the experimental and the numerical results, in terms of deviatoric stress at failure. For the Hostun sand they are summarized in Table 3.2.1.

Sand Type	φ_μ (°)	K_N/d_{av} (MPa)	K_S/K_N (-)
Hostun	19.3	330	0.25

Table 3.2.1. Best fit micromechanical parameters for Hostun Sand (Calvetti *et al.*, 2003)

The comparison between the experimental and the numerical test is shown in Figure 3.2.3: the model has a higher stiffness at small shear strains, but reaches the same critical deviatoric stress. Moreover, it has larger volumetric expansion in correspondence of the fully plasticized zone. These evident differences merely arise from the early simplifications considered for the model (spherical shape and fixed rotation of the particles, simple grain size curve). Obviously, these aspects represent a limit of the adopted numerical approach; nevertheless, it gives the opportunity to perform analyses with a reliable response, in terms of resistance, limiting as much as possible the computational effort.

In the present work, the investigation of the Hostun sand model response under deviatoric stress at varying initial conditions (porosity and confining pressure) is carried out.

Firstly, the minimum and the maximum porosity for DEM sample are determined. The minimum porosity (or void index) is the lowest obtained by the progressive reduction of the interparticle friction angle at a fixed low confining pressure (p = 5 kPa): the absence of friction allows particles to slip free, therefore these tend to fill all the residual voids. The maximum porosity, instead, is the one obtained by generating a sample with a high value of the input porosity (for example n_{input} = 0.60) which a very low confining stress (p = 5 kPa) is applied to.

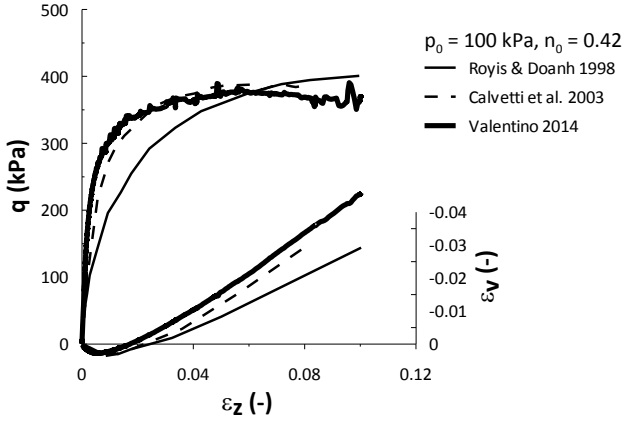

Figure 3.2.3. Comparison among DEM analyses and laboratory tests for Hostun Sand

The porosity range determined for the Hostun sand model goes from 0.380 to 0.490, in spite of the experimental maximum and minimum void ratios,

that corresponds to n_{min} = 0.393 and n_{max} = 0.508. This difference depends on two aspects: first of all, the implemented procedure does not correspond to the standard measurement test in laboratory; besides, the sand model has different index properties than the real sand (spherical particles and simplified grain size distribution). With these premises, the writer reserves to verify the goodness of the proposed porosity range in the following part of the work.

Afterwards, six samples with different porosities (n = 0.40, 0.41, 0.42, 0.43, 0.45, 0.48) are subjected to four drained triaxial tests with different initial confining stress levels (p_0 = 50, 100, 200, 800 kPa). For all the 24 cases considered, the stress-strain [ε_z-q/p] and the deviatoric strains – porosity planes [ε_z-n] are plotted. In Figure 3.2.4 all the numerical results are gathered, sorted by porosity.

In the stress-strain planes, for cases with n = 0.40, 0.41 and 0.42, the specimens exhibit a peak of resistance at a shear strain ε_z of about 1%, then it is followed by a softening till the deviatoric stress reaches the critical value at $\varepsilon_z \approx$ 20%. At the increasing initial confining stress the peak occurs at higher values of deformations ($\varepsilon_z \approx$ 8%).

For n > 0.42, the DE-soil assumes a ductile behaviour for every value of confining pressure. On the other hand, in the [ε_z-n] plane, for all the cases, firstly there is a reduction of porosity at a very low strain level that increases with the increasing initial confining pressure and goes from 0.3% to 4%. At larger ε_z, the soil expands indefinitely, without approaching to the critical porosity.

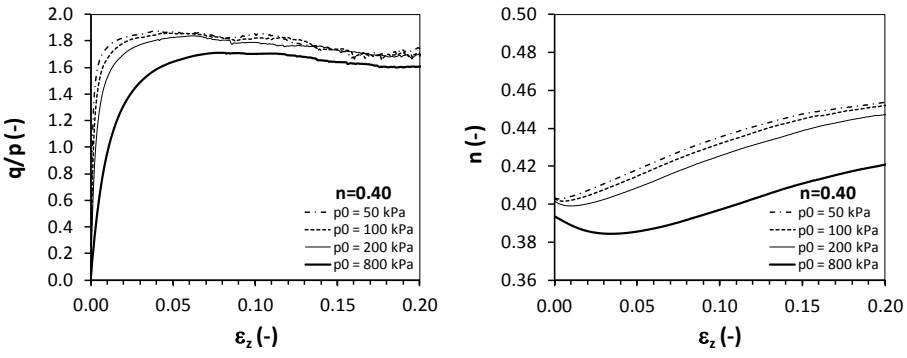

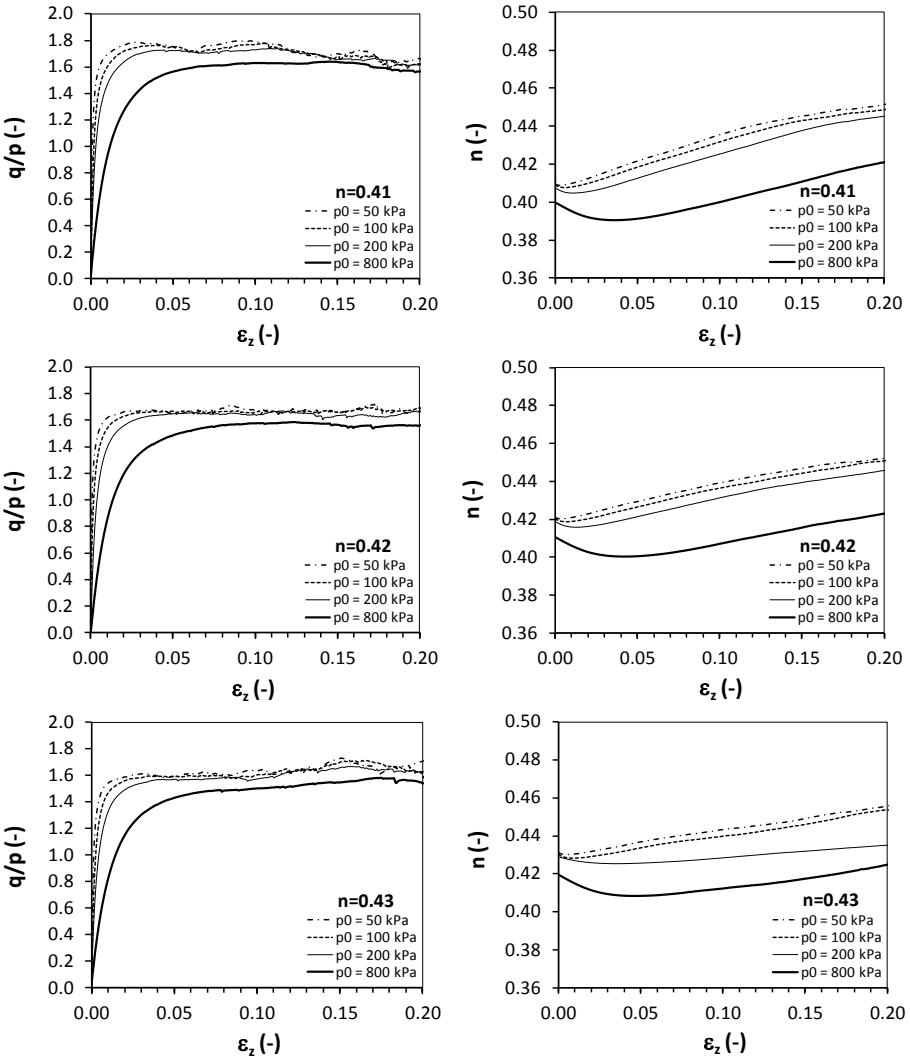
q/p (-)
n (-)
ε_z (-)
n=0.41
n=0.42
n=0.43
p0 = 50 kPa
p0 = 100 kPa
p0 = 200 kPa
p0 = 800 kPa

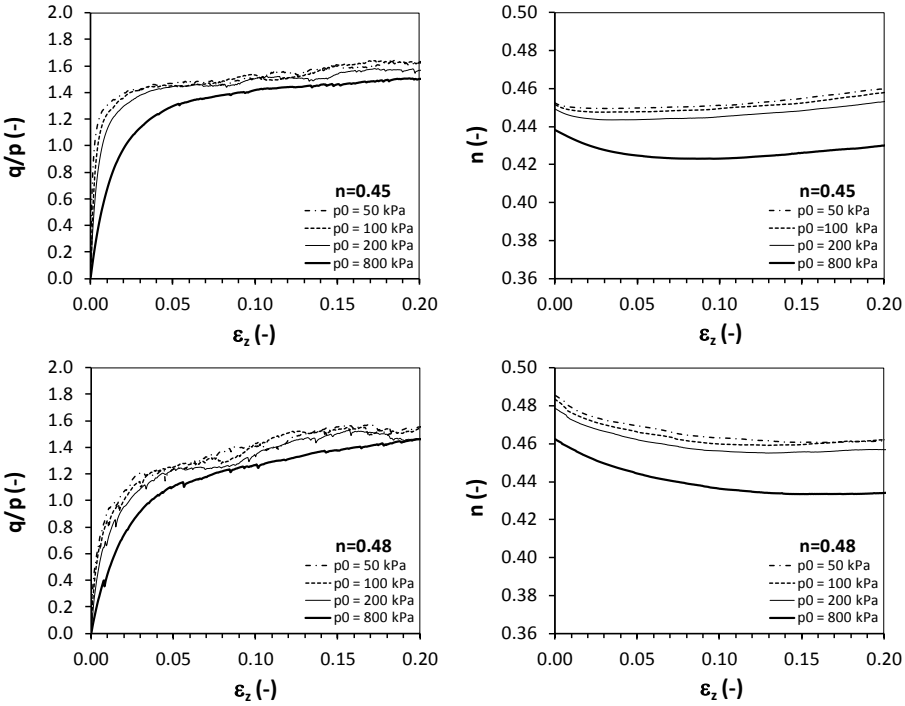

Figure 3.2.4. Stress-strain and porosity-strain planes from triaxial DE-test on Hostun sand model

The formulation proposed by Rowe (1962), which puts in relation the stress state with the increment of plastic deformations, is considered, in order to calculate the friction angle at constant volume φ_{cv} for the Hostun sand model:

$$\frac{\sigma_1'}{\sigma_3'} = \left[tg^2\left(45° + \frac{\varphi_{cv}}{2}\right)\right] \cdot \left[1 - \left(\frac{d\varepsilon_v}{d\varepsilon_z}\right)_p\right] \qquad (3.2.1)$$

In correspondence of the minimum of the curve [ε_v-ε_z] the ratio $\left(\frac{d\varepsilon_v}{d\varepsilon_z}\right)_p$ is null, therefore the contribute offered by dilatancy is null and the crtical deviatoric stress is determined. Figure 3.2.4 reports the variation of porosity, instead of volumetric strains, with deviatoric deformations. However, this does not make a conceptual difference with the Rowe's formulation, since the variation of porosity is exactly defined as a volume variation. Hence, for each case the critical deviatoric stress is considered in correspondence of the minimum porosity reached. All the critical points are collected in the

compression plane, then interpolated with a linear function: from the slope M = 1.44 the calculated friction angle at constant volume is φ_{cv} = 35.5° (Figure 3.2.5).

In Figure 3.2.6 the stress paths in the [n-p] plane for all the cases are shown. For n_0 < 0.45 the paths approach to the critical state by an initial compression till a confining stress ≈ $2p_0$, followed by a dilation. For n_0 > 0.45, instead, critical state is reached through a volumetric compression.

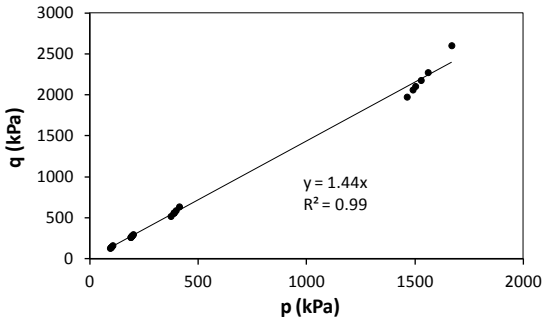

Figure 3.2.5. Critical state line from triaxial DE-test on Hostun sand model

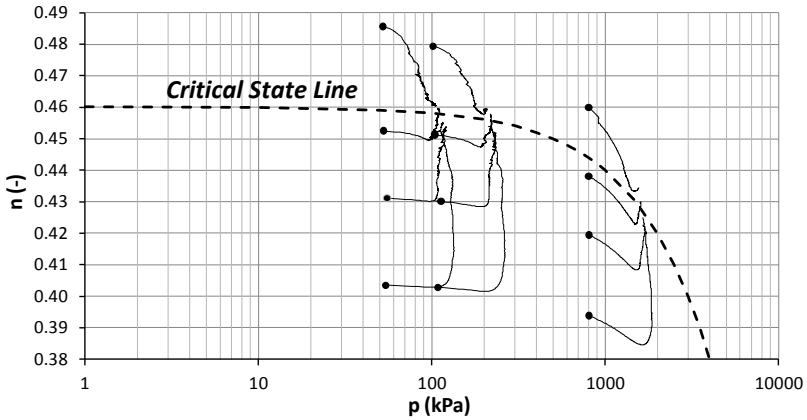

Figure 3.2.6. Stress paths from triaxial test on Hostun sand model

3.3. Modelling of Cone Penetration Tests in Calibration Chamber

Penetration tests in the Calibration Chamber (CC) are a valuable tool for reproduction and prediction of the cone response. Several formulations, which correlate the cone resistance with the mechanical soil parameters, hail from CC

tests. Nevertheless, these kind of laboratory tests are very expensive and time-consuming, for this reason their use is not so spread and many attempts to simulate the cone penetration test in sand have been done by both finite and discrete element method.

Arroyo *et al.* (2011) simulate the cone penetration tests performed in calibration chamber by Jamiolkowski *et al.* (2003) in Ticino River sand by means of the Distinct Element Model. For the numerical analyses the code *PFC3D* is used. Before performing the CC test, the Authors have calibrated the DE-soil by reproducing the response of the element test under triaxial compression at different initial conditions (following the same procedure introduced in §3.2.). The sample is cubical, with a length of 8 mm and contains about 4700 particles; the grain-size curve is truncated and the mean diameter is d_{av} = 0.53 mm. The micromechanical parameters they have found for this sand are reported in Table 3.3.1.

The DE-model for the calibration chamber test, called "*Virtual Calibration Chamber (VCC)*", has modified dimensions and a scaled grain size, with the aim to reduce the particles to a more manageable number.

Sand Type	φ_μ (°)	K_N/d_{av} (MPa)	K_S/K_N (-)
Ticino	18	420	0.25

Table 3.3.1. Micromechanical parameters for Ticino River Sand (Arroyo *et al.*, 2011)

If the real dimension of sand particles is considered, indeed, the model contains more than 1E+10 spheres and this number is far beyond the current computational abilities. In particular, the model grain size curve is obtained by cutting the finest diameters (less than 10%) and scaling by a 50 factor, as shown in Figure 3.3.1.

The geometry of the model is completely assigned if the n_p, R_d and n_h parameters are fixed, where n_p is the ratio between the cone diameter d_c and the mean particles diameter d_{av}; R_d is the ratio between the chamber diameter D_c and the cone diameter; n_h is the ratio between the chamber height H_c and cone diameter. In this case n_p is reduced from 67 to 2.7, R_d is the half than the CC value and n_h is 9.8 instead of 16.9. By means of the modified geometry ratios the number of particles ($\#_b$) goes down from 1E+10 to 6E+04, which represents a manageable computational effort. Table 3.3.2 reports a summary of the geometric parameters for the VCC model.

The cone shaft consists of three frictional rigid cylindrical walls and one frictionless; the tip has an angle of 60° and is frictional, too. The particle/wall

friction angle is assumed to be the same as the particle/particle angle, φ_μ = 19.3°.

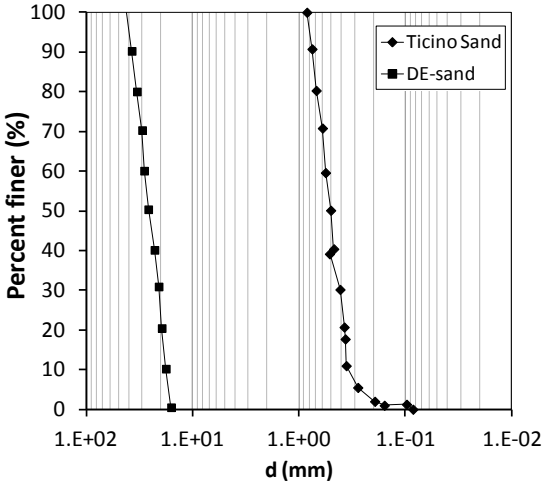

Figure 3.3.1. Grain size curve for Ticino River Sand (Arroyo *et al.*, 2011)

	CC Ticino Sand	**VCC Ticino Sand**
d_c (mm)	35.6	71.2
d_{av} (mm)	0.53	26.5
D_c (mm)	1200	1200
H_c (mm)	1500	700
n_p (-)	67	2.7
R_d (-)	33.7	16.9
n_H (-)	16.9	9.8
#$_b$ (-)	1.8×10^{10}	6.5×10^{4}

Table 3.3.2. Summary of geometrical parameters for VCC (Arroyo *et al*., 2011)

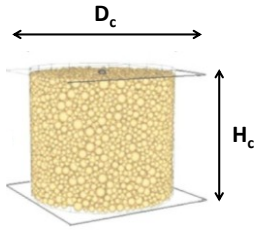

Figure 3.3.2. Virtual Calibration Chamber (Arroyo *et al.*, 2011)

The penetration rate is fixed at 10 cm/s, despite in the physical CC the CPT velocity is 2 cm/s, since using the real rate is very time-consuming. Therefore a scaling factor also for velocity is numerically convenient, as long as the inertia effects are second order and the cone resistance does not change (Butlanska *et al.*, 2010).

The Authors present a rich test series, where different initial conditions and different geometries have been considered. The penetration occurs in a soil with an isotropic stress constant with depth; the chamber has moving walls, in order to maintain the initial stress during penetration.

Cone resistance q_c is determined as the sum of the vertical components of cone/particles contact forces on the base area of the cone tip. Since q_c profile presents marked oscillations, a fitting function is considered with which it is possible to read the average value $q_{c,av}$. This latter increases with the increasing R_d (see Figure 3.3.3), and, as a consequence, there is an evident board effect. Moreover, the CPT response is influenced by the ratio n_p: when this is lower than 40, scrapping noises and erratic load readings can appear (Peterson, 1988). For this reason, in the paper is presented a sensitivity study where cone diameter increases and particles sizes are fixed, with an n_p ratio that assumes the values 2.7, 4, 5.4, 8. Figure 3.3.4. shows a cone penetration resistance that reduces at the increasing n_p, so this ratio seems to exhibit a very important influence on $q_{c,av}$. Actually, for the cases that have been considered, R_d is variable, too, because if d_c increases and the chamber diameter is fixed, the value of R_d (which is the ratio between these two terms) decreases and in particular it goes from 16.8 to 5.6.

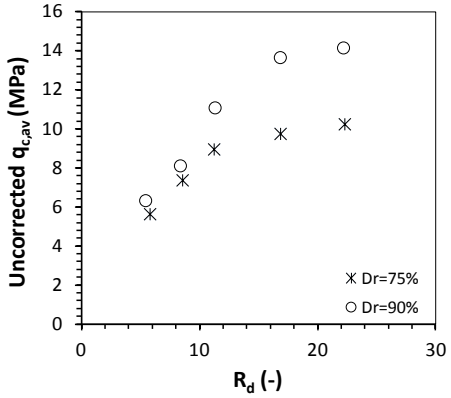

Figure 3.3.3. Influence of chamber size on $q_{c,av}$ (Arroyo *et al*., 2011)

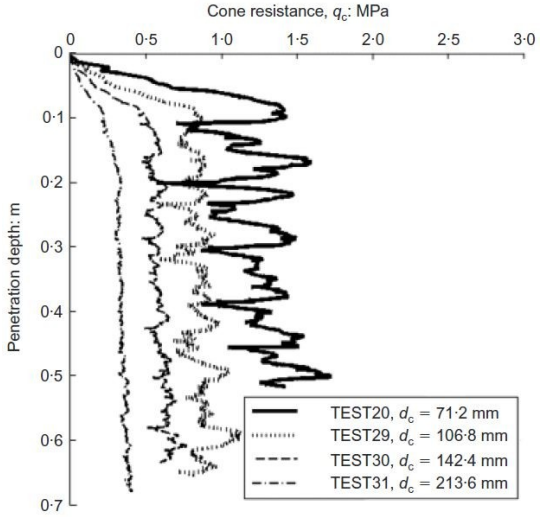

Figure 3.3.4. Influence of cone to particle size on q_c profile (Arroyo *et al*., 2011)

Eventually, the Authors suggest the optimal geometries ratios R_d and n_p, which guarantee the most reliable results with the most limited number of particles, as 16.9 and 2.7, respectively.

From this starting point, a series of CPT in virtual calibration chamber is performed (Table 3.3.3), considering different initial porosities and confining stresses, aiming to gain handiness for such a kind of simulations.

Test	CC	p_0 (kPa)	n_0 (-)
1	1	60	0.38
2	1	100	0.38
3	1	100	0.37
4	0.25	100	0.38
5	0.50	100	0.38

Table 3.3.3. Summary of performed CPT tests in VCC

For every test, the cone resistance q_c is plotted against the penetration level and, in particular, it can be seen that numerical results well reproduce the expected response, because q_c is constant with depth (it is reminded that the soil is subjected to a isotropic confining stress constant with depth).

Furthermore, it increases with p_0 at a fixed n_0 (Test 1 and 2) and increases with the decreasing n_0 at a fixed p_0 (Test 2 and 3), as shown in Figure 3.3.5.

In addition, a comparison of the numerical results with the empirical correlation by Jamiolkowski *et al.* (2003) for q_c is provided. The formulation requires the relative density profile for soil layer, but, as introduced in §3.2, the evaluation of minimum and maximum porosities for the sand model is not an easy matter, therefore many uncertainties lie on the calculated n_{min} and n_{max}.

For this reason, it appears reasonable to put the equality between the numerical result for q_c and the calculated cone resistance, in order to obtain an "operative value" of relative density for every model. In particular, the correlation by Jamiolkowski *et al.* (2003) is considered:

$$q_c{}^* = C_1 \cdot p_{atm} \cdot \left(\frac{p'}{p_{atm}}\right)^{C_2} \cdot e^{C_3 D_R} \tag{3.3.1}$$

where p_{atm} is the atmospheric pressure, p' the mean effective stress and C_1, C_2 and C_3 are experimental coefficients that, for an isotropic and constant with depth stress state of Ticino sand, assume respectively the values 23.19, 0.56 and 2.97.

This formula hails from a series of experimental CPT tests performed in a calibration chamber for different typologies of sand.

When moving walls are considered as boundary conditions the measured cone resistance can be underestimated, because it is influenced by the limited dimensions of the chamber box. For this reason, the Authors correct q_c by a correction factor CF, defined as

$$\mathrm{CF} = \mathrm{a}(\mathrm{D_R})^{\mathrm{b}} \tag{3.3.2}$$

where a and b are two statistic parameters that are function of R_d (Butlanska *et al.* 2010):

$$\begin{cases} a = 9 \cdot 10^{-5} \cdot R_d^{2.02} \\ b = -0.565 \cdot \ln(R_d) + 2.59 \end{cases} \tag{3.3.3}$$

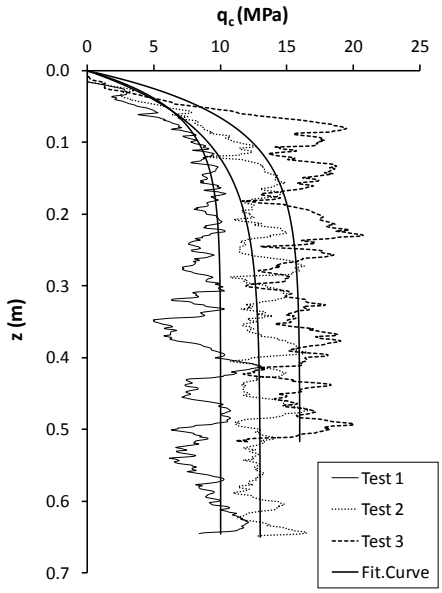

Figure 3.3.5. Influence of porosity and confining stress on CPT resistance

Hence, it is possible to put the following equality:

$$\mathrm{q_c^{UNCOR}} \cdot \mathrm{a} \cdot (\mathrm{D_R})^{\mathrm{b}} = C_1 \cdot p_{atm} \cdot \left(\frac{p'}{p_{atm}}\right)^{C_2} \cdot e^{C_3 D_R} \tag{3.3.4}$$

where the only one variable is D_R. In this way, it is possible to determine the operative relative density D_{Rop}, which guarantees the identity between VCC and CC. In Table 3.3.4. the values of the calculated D_{Rop} are reported for all the cases: it can be seen that to the initial porosities 0.38 and 0.37 correspond the operative relative densities 86% and 97%, respectively.

If relative density is calculated by considering the minimum and maximum void index from laboratory (for Ticino sand they are e_{max} = 0.924 and e_{min} = 0.578) the experimental D_R are 90% for n_0 = 0.38 and 97% for n_0 = 0.37.

This good correspondence has two important meanings: first of all, the DE model for Ticino sand has a grain-size distribution very close to the experimental one; in addition, the procedure to identify the operative value of D_R, just fitting the numerical profile for q_c with the one calculated by a simply correlation appears to be reliable.

Secondly, two further cases with a quarter (CC 0.25) and half (CC 0.50) chamber, respectively Test 4 and Test 5, are reported. Porosity and confining pressure are the same as Test 1 and Test 2, in order to make a comparison. From Figure 3.3.6. it is evident that the model CC 0.25 has a lower value of cone resistance than Test 2 and 5 (about -25%), the operative relative density is lower indeed. Test 5, instead, has quite the same $q_{c,UNCOR}$ than Test 2 (about -3%).

Definitively, the quarter model is not efficient for these kinds of tests, because of the higher porosity that the assembly presents in the corner where the cone comes down. As a consequence, it is possible to use the half model, so that the number of particles (i.e. the computational effort) is limited.

Test	CC	p_0 (kPa)	n_0 (-)	$q_{c,UNCOR}$(MPa)	CF	D_{Rop} (%)
1	1	60	0.38	10.0	2.30	86
2	1	100	0.38	13.3	2.26	86
3	1	100	0.37	16.0	2.55	97
4	0.25	100	0.38	10.7	1.97	75
5	0.50	100	0.38	12.8	2.24	85

Table 3.3.4. Results of performed CPT tests in VCC

As it has often been recalled in this chapter, such a kind of simulation is rather time-consuming. For this reason, a try to reduce the time solving is done by amplifying the cone penetration rate. Specifically, Test 1 is performed also with a penetration rate 10 times greater than the previous one (10 cm/s). From the comparison between the two cases (Figure 3.3.7), it is evident that there are no substantial differences, so for the further studies an higher penetration rate can be assumed.

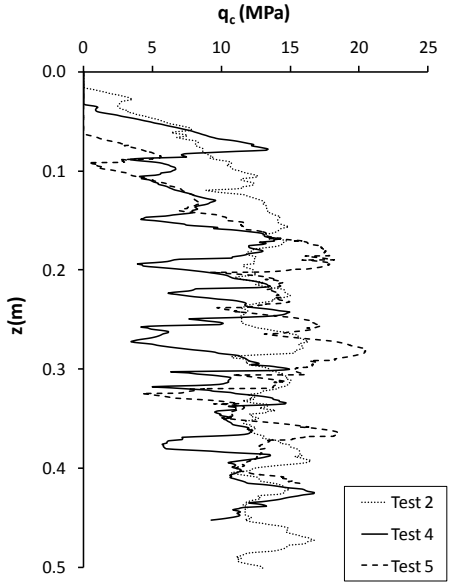

Figure 3.3.6. Influence of chamber type on CPT resistance

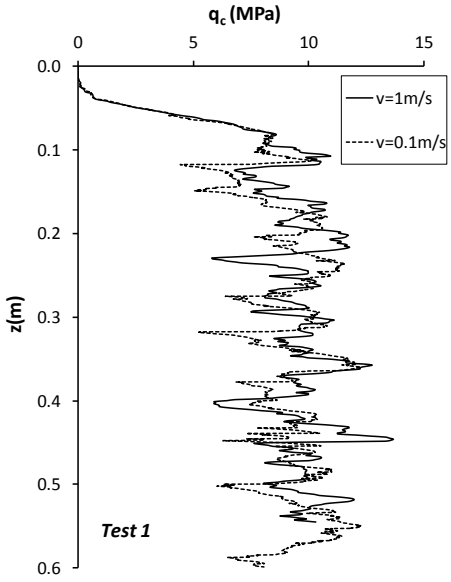

Figure 3.3.7. Influence of penetration rate on CPT resistance for Test 1

3.4. Modelling of Cone Penetration Tests in situ

The results reported in the previous paragraph show a cone response undoubtedly realistic. Consequently, it appears reasonable to model cone penetration test at a field scale. With this aim, suggestions for the geometry scaling factors by Arroyo *et al*. (2011) are fundamental, since the dimensions of the field model are much greater than the calibration chamber.

In the present work cone penetration tests in the Hostun sand model are performed. The site is modelled as an homogeneous layer with a simplified grain-size curve (see Figure 3.2.2). A gravitational initial soil state is imposed to the assembly and, during this phase, the chamber/particle friction angle is switched off. Porosity is kept constant with depth and, in particular, three values are considered: n = 0.45, 0.43 and 0.41.

The cone model has the standard diameter, d_c = 0.036 m, as a consequence, since the geometry ratios R_d and n_p are fixed at the values of 20 and 3, respectively, the chamber has a diameter D_c = 0.72 m and the mean diameter of particles is d_{av}^* = 0.012 m, corresponding to a scaling factor SF of 40. The wall/particle friction coefficient is assumed to be the same as the interparticle one $\mu_w = \mu = 0.35$ and the penetration rate is 10 times the standard velocity applied to mechanical devises (v = 1 m/s).

Falagush *et al.* (2013) show that the cone resistance profile is not affected by the chamber height, therefore the choice of H_c is a mere valuation that the user makes considering the desired maximum number of particles and the solving time. In this case the CPT are extended up to limited depths, because the high number of particles and the low scaling factor make the analyses very time-consuming. The only way to simulate a cone penetration test up to a deepened soil layer, adopting the actual cone dimensions, is to divide the layer into sections placed in succession. Every section is subjected to the respective geostatic state which is applied by a distributed load at the top of the chamber equal to the weight of the upper soil (Figure 3.4.1). Herein, one case of CPT in sequence is reported: the model consists of three sections with a height of 3.5 m, so the whole layer has a thickness of 10.5 m.

d_{av} (m)	SF (-)	d_{av}^* (m)	d_c (m)	D_c (m)	H_c (m)	R_d (-)	n_p (-)	n (-)	v (m/s)	$\#_{b,TOT}$ (-)
0.0003	40	0.012	0.036	0.72	3.5	20	3	0.44	1	750000

Table 3.4.1. Summary of model characteristics for CPT tests in sequence in Hostun Sand

Also for the test performed in the DE-field, it is possible to make a comparison between the q_c profile obtained from the numerical analysis and the profile calculated by a variation of Eq. (3.3.1), Equation (3.3.4), for a geostatic stress condition. The chamber has fixed walls: for this kind of boundary condition Jamiolkowski *et al*. (2003) suggest to divide q_c for the correction factor reported in Eq. (3.3.2). However, Butlanska *et al*. (2010) report cone penetration test in VCC with such a boundary condition and suggest not to correct the q_c values for $R_d \geq 17$.

$$q_c{}^* = 17.68 \cdot p_{atm} \cdot \left(\frac{\sigma_{v0}{}'}{p_{atm}}\right)^{0.55} \cdot e^{3.1 D_R} \qquad (3.3.4)$$

The q_c profile obtained for the CPT in sequence has a good match with a $q_c{}^*$ corresponding to a D_{Rop} = 15%.

Nevertheless, it is a writer's opinion that such a kind of simulations requires too much time and it is not worth, since the q_c profile matches well with the correlation. Hence, it is retained sufficient to extend the analysis up to a limited depth, fitting with the calculated profile and, when it is necessary, extrapolating the q_c related to the required depth.

With this early assumption, the cone penetration tests in short model and half chamber at the different porosities n = 0.41, n = 0.43 and n = 0.45 are performed; in Table 3.4.2 geometrical properties of the model are reported.

The q_c profile for the case with n = 0.45, 0.43 and 0.41 has a good match with the correlation, respectively corresponding to D_{Rop} = 5, 26 and 60%.

d_{av} (m)	SF (-)	d_{av}^* (m)	d_c (m)	D_c /2 (m)	H_c (m)	R_d (-)	n_p (-)	μ_W (-)	v (m/s)	$\#_b$ (-)
0.0003	40	0.012	0.036	0.36	3.5	20	3	0.44	1	224885

Table 3.4.2. Summary of model characteristics for CPT tests in Hostun Sand

As for the calculated maximum and minimum porosities, to n = 0.41, 0.43 and 0.45 correspond a relative density of 76%, 59% and 41%, respectively. These calculated values are clearly very different from the operative ones.

Hence, it is evident that the procedure adopted for the evaluation of the porosity range is not reliable.

This affirmation could appear a contradiction, if the good agreement between the porosity range from DEM and the laboratory for Ticino Sand is considered; however, the laboratory tests for the DE-model of Ticino sand have been carried out considering a much more detailed grain-size curve, closer to

the actual one. For the Hostun sand, instead, because of the will to model in situ tests, a much simpler distribution has been preferred from the beginning, in order to limit the number of particles as much as possible. Anyway, the operative relative density is just a numerical value, which is very useful for the comparison with the experimental data, but without a real physical meaning. For these reason, it is retained to be proper not to refer to it, but to the porosity of the assembly and to the corresponding response (expanding or contractive) at the varying confining stress accurately investigated in §3.2.

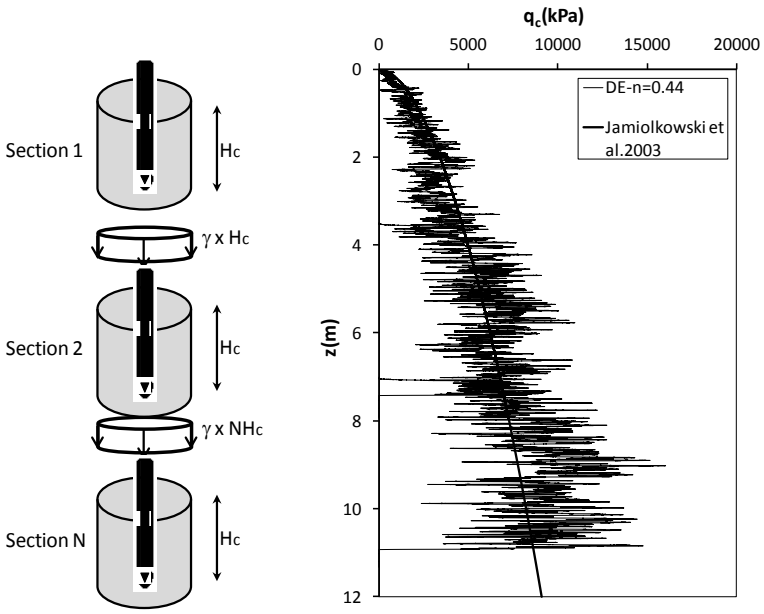

Figure 3.4.1. Cone Penetration Tests in sequence

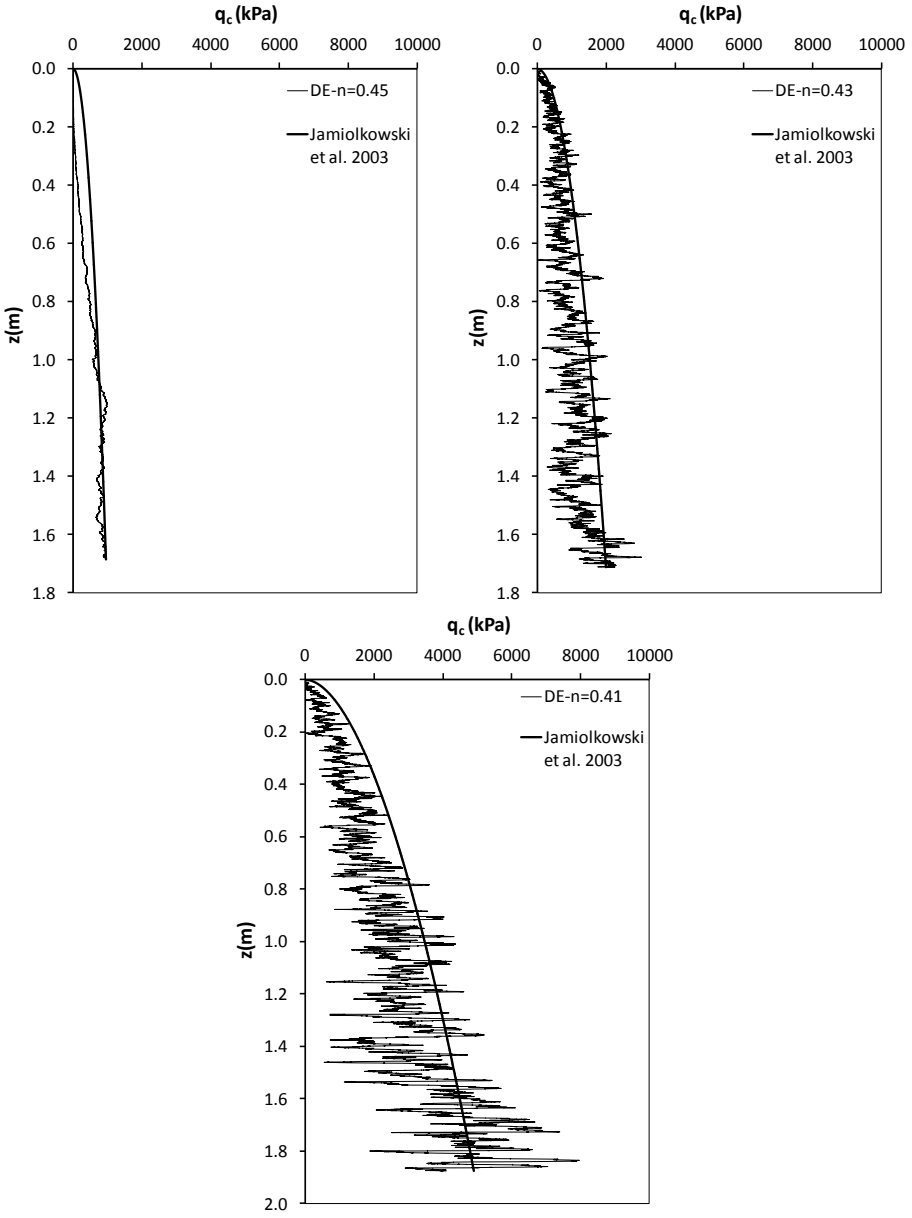

Figure 3.4.2. q_c profile from CPT in the short model for n = 0.41, n = 0.43 and n=0.45

3.5. Modelling of jacked pile installation

The installation of a jacked closed-ended pile is modelled by pushing the pile by a constant penetration rate till the project depth is reached. As the insertion phase is accomplished, a traction force is applied as far as the total load at pile top is null (Figure 3.5.1).

In the previous paragraphs the simulations of cone penetration tests in calibration chamber and in situ have been presented. As a cone device can be seen as a small jacked pile, the same typology of simulation can be performed for full scale jacked piles installation. However, pile response strictly depends also on the sliding mechanism at soil-pile interface (shaft friction), but this aspect has not been considered for the modelling of CPTs, so far. Moreover, the investigations on R_d and n_p variation reported by Arroyo *et al.* (2011) are not exhaustive, because from Figure 3.3.3 it is evident that $q_{c,av}$ does not reach an asymptotic value and, from Figure 3.3.4, n_p increases with decreasing R_d. As a consequence, it is not possible to understand the actual influence exerted by the single parameter. In addition, there is not any connection to the influence that porosity could exert on the fixed geometric ratios. No one reference has been made about the possible influence by the inferior board of the chamber, as well.

For all these reasons, further research is needed so that good results will be provided also for pile response.

In this paragraph, sensitivity analyses for the modelling of jacked piles installation are carried out.

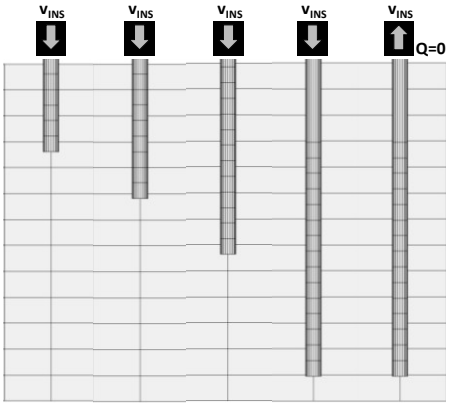

Figure 3.5.1. Stages of jacked pile installation

The simulations are performed in the Hostun sand whose geometric and micromechanical properties have already been introduced in §3.2. Pile is a wall element modelled as an assembly of cylindrical frictional sections with a height of 0.60 m. Pile length and diameter are indicated with L_p and d_p, respectively. The micromechanical parameters for the wall/particle contact are set the same as for the particle/particle contact.

The chamber has fixed walls for all the cases.

The sensitivity study consists of 25 cases, summarized in Table 3.5.1, where the influence of the single parameters on pile response is investigated.

In particular, these are:

- $R_d = \frac{D_c}{d_{av}^*} = 10 \div 35$
- $n_p = \frac{d_p}{d_{av}^*} = 3 \div 8$
- $n_H = \frac{H_c - L_p}{d_p} = 1.3 \div 2.5$
- $G = \frac{v_{ins}}{v} = 1 \div 20$
- *Disk and Conical tip*
- *Complete, Half and quarter model*
- *Uniform and radial scaled grain-size distribution*

Case	SF (-)	d_{av}^* (m)	n (-)	L_p (m)	d_p (m)	n_p (-)	n_H (-)	G (-)	R_d (-)	Model Type	$\#_b$ (-)
1	500	0.15	0.45	4.50	0.45	3	2.50	10	20	*Complete*	112442
2	500	0.15	0.45	4.70	0.45	3	2.50	10	25	*Complete*	140553
3	500	0.15	0.45	4.70	0.45	3	2.50	10	30	*Complete*	202397
4	500	0.15	0.45	4.50	0.45	3	2.50	10	35	*Complete*	275485
5	500	0.15	0.45	3.90	0.60	4	2.00	10	20	*Complete*	159918
6	500	0.15	0.45	4.20	0.90	6	1.75	10	20	*Complete*	359817
7	500	0.15	0.45	4.36	1.20	8	1.30	10	20	*Complete*	639675
8	500	0.15	0.41	2.30	0.90	6	1.75	1	20	*Complete*	518137
9	500	0.15	0.41	5.47	0.90	6	1.75	10	20	*Complete*	518137
10	500	0.15	0.41	5.00	0.90	6	1.75	20	20	*Complete*	518137
11	500	0.15	0.41	4.40	0.90	6	1.75	10	27	*Complete*	639675
12	333	0.10	0.45	3.40	0.60	6	1.75	10	10	*Complete*	107977
13	333	0.10	0.45	2.80	0.60	6	1.75	10	13	*Complete*	182482
14	333	0.10	0.45	3.00	0.60	6	1.75	10	15	*Complete*	242949
15	333	0.10	0.45	7.90	0.60	6	1.75	10	15	*Complete*	518137

16	333	0.10	0.43	3.25	0.60	6	1.75	10	15	*Complete*	242949
17	333	0.10	0.43	3.60	0.60	6	1.75	10	17	*Complete*	312055
18	333	0.10	0.43	5.75	0.60	6	1.75	10	20	*Complete*	518137
19	333	0.10	0.43	8.45	0.60	6	1.75	10	20	*Half*	653264
20	333	0.10	0.41	8.22	0.60	6	1.75	10	20	*Half*	653264
21	333	0.10	0.43	4.35	0.60	6	1.75	10	20	*Quarter*	129535
22	333	0.10	0.43	2.40	0.60	6	1.75	10	20	*Radial SF*	257285
23	333	0.10	0.45	2.44	0.60	6	1.75	10	15	*Cone*	518137
24	333	0.10	0.43	2.96	0.60	6	1.75	10	20	*Cone*	653264
25	333	0.10	0.41	3.56	0.60	6	1.75	10	20	*Cone*	653264

Table 3.5.1. Summary of case studies for jacked pile installation model

INFLUENCE OF R_d

The first set of parametric analyses are done varying the ratio between chamber diameter and pile diameter. The minimum value which has been considered is R_d = 20, porosity n and n_p are fixed at 0.45 and 3, respectively (Cases 1-4).

In Figure 3.5.2 the unit base resistance q_b is reported, normalized to the vertical effective initial stress and plotted against the insertion level on pile diameter d_p. The ratio $q_{b,INS} / \sigma_{v0}$, which corresponds to the end-bearing capacity factor $N_{q,INS}$, has an initial drastic increase, but, after the peak value, it starts decreasing as long as it reaches a constant value, even though at about a $2d_p$ distance from the lower boundary of the chamber $N_{q,INS}$ starts increasing again. All the considered tests have the same response and there is a good match among all the curves.

As to shaft friction, the horizontal stress is calculated for each one of the pile sections as the sum of the horizontal contact forces acting on the single section and divided by its side area. The horizontal stress during pile insertion $\sigma_{h,INS}$ is plotted against the insertion level for all the sections in the four cases considered. These are quite overlapping at increasing R_d.

Definitively, for n_p = 3 and n = 0.45 the minimum ratio R_d = 20 appears reasonable both for base and shaft resistance.

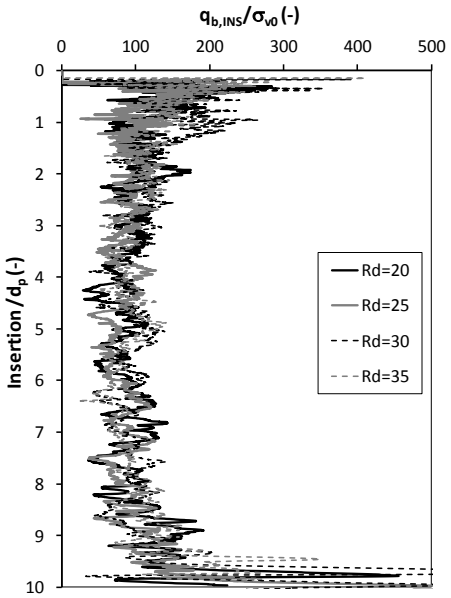

Figure 3.5.2. Normalized base resistance at varying R_d ratio

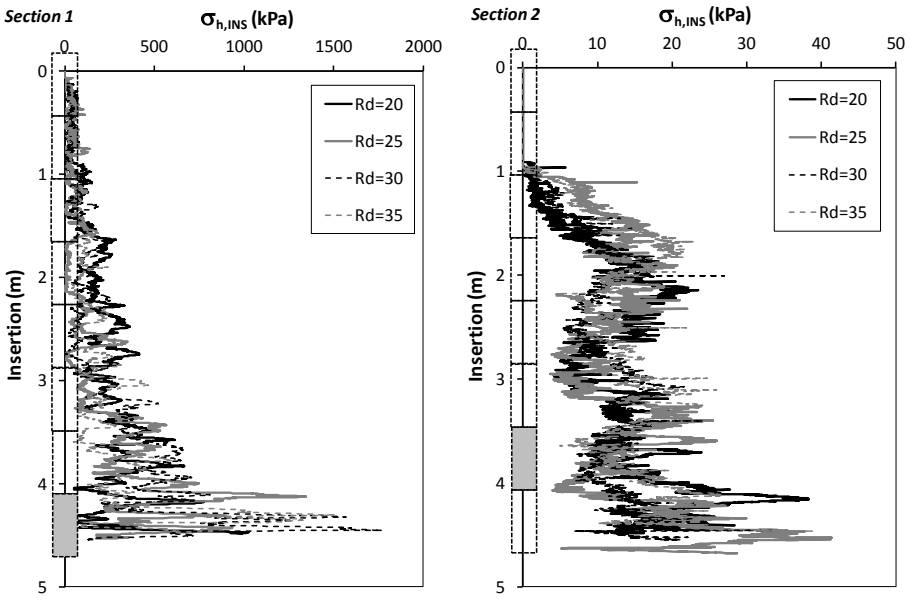

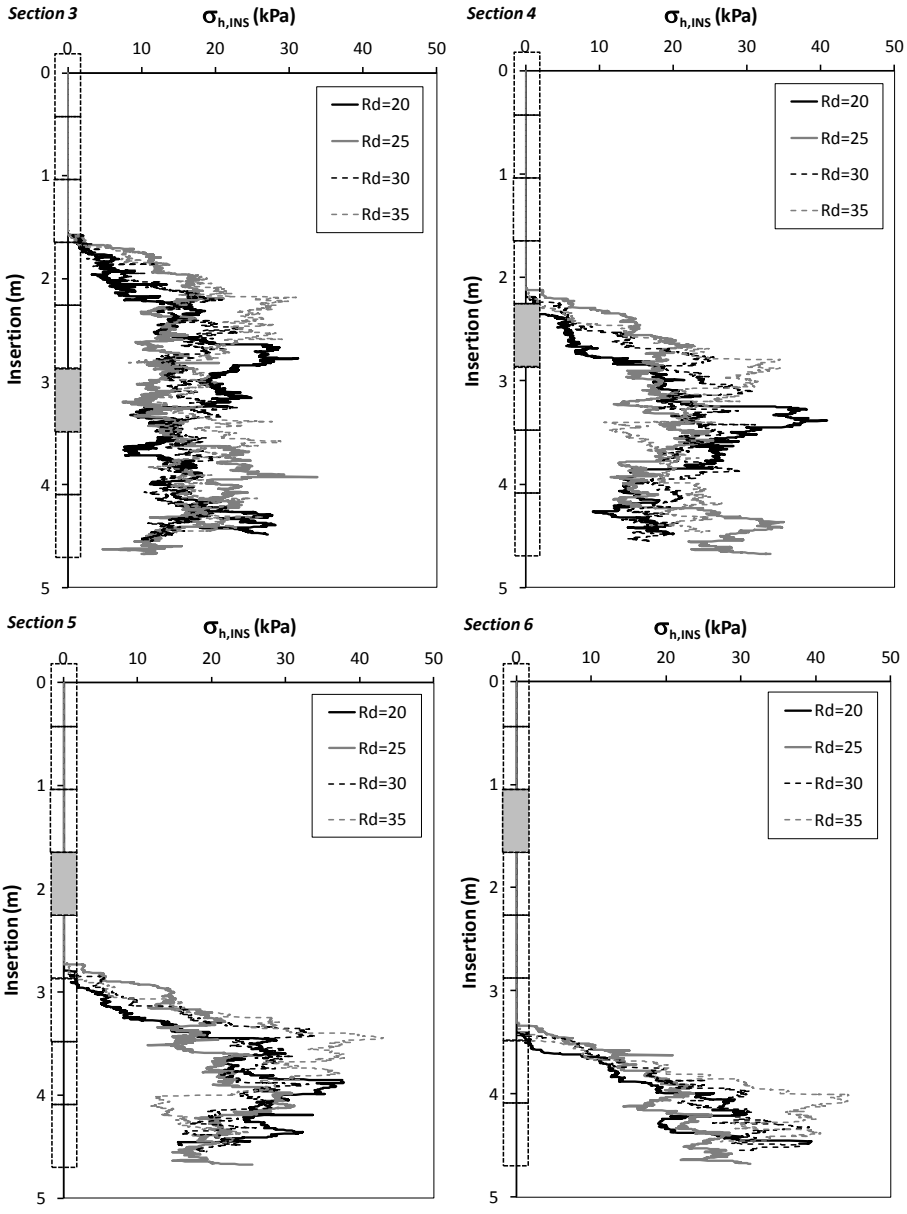

Figure 3.5.3. Horizontal stress at pile shaft during pile insertion at varying R_d

INFLUENCE OF n_p

The second set of analyses is for the investigation about n_p influence on pile response (Cases 5-8). As for R_d variation, base resistance is recorded during pile insertion and the ratio $q_{b,INS}/\sigma_{v0}$ is plotted against the normalized insertion for all the cases: from Figure 3.5.4 it can be noticed that at varying n_p the base resistance maintains the same profile and average values.

At pile shaft, the horizontal stress during the insertion is reported in Figure 3.5.5, where it is shown a $\sigma_{h,INS}$ profile decreasing at the increasing n_p. Specifically, for n_p = 3 the stress is markedly higher than in the other case, whilst cases n_p = 6 and 8 have a quite good match. Unfortunately, it has been not possible to investigate higher values of this ratio, because of the strong computational limits, but, from the considerations above, n_p = 6 is retained to be a good compromise between the reliability of results and the computation effort.

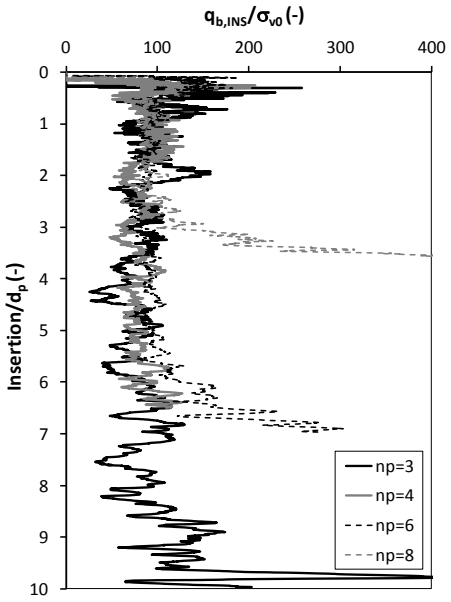

Figure 3.5.4. Normalized base resistance at varying n_p ratio

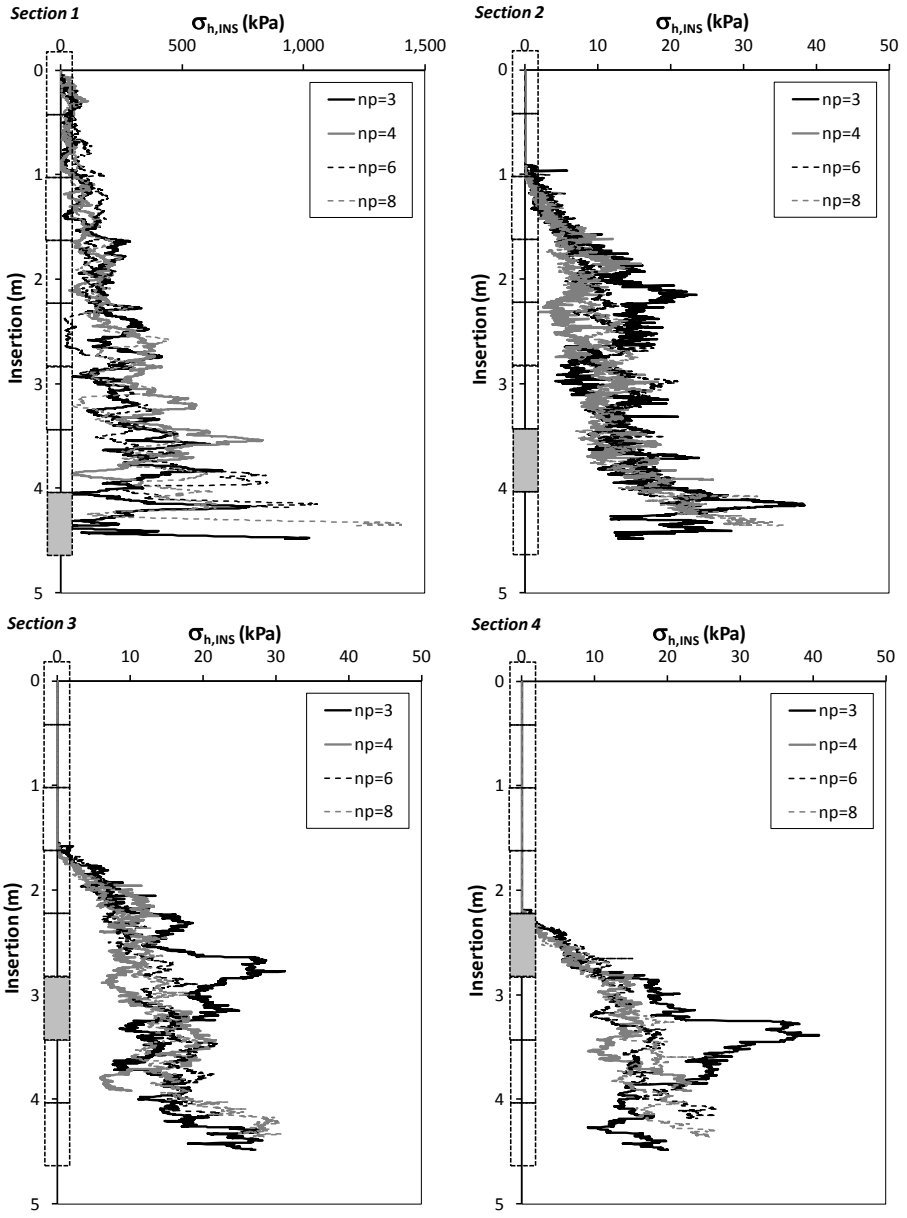
Section 1
σh,INS (kPa)
0
500
1,000
1,500
Insertion (m)
np=3
np=4
np=6
np=8
Section 2
σh,INS (kPa)
0
10
20
30
40
50
Insertion (m)
np=3
np=4
np=6
np=8
Section 3
σh,INS (kPa)
0
10
20
30
40
50
Insertion (m)
np=3
np=4
np=6
np=8
Section 4
σh,INS (kPa)
0
10
20
30
40
50
Insertion (m)
np=3
np=4
np=6
np=8

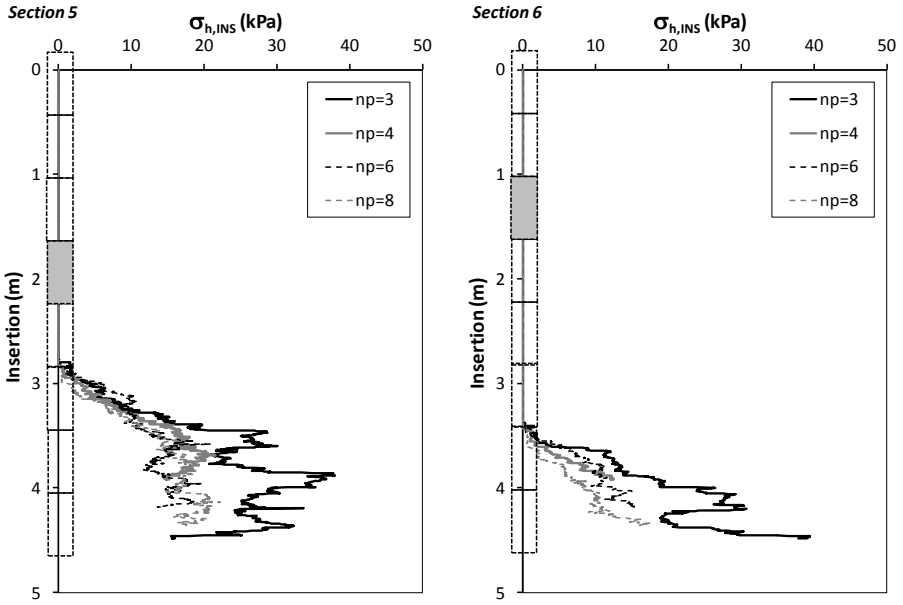

Figure 3.5.5. Horizontal stress at pile shaft during pile insertion at varying n_p

INFLUENCE OF n_H

Since the bottom of the chamber is fixed, if the pile gets too close the base resistance can be affected by the board influence. Hence, it is necessary to find a minimum distance from the board beyond which there is no effect on pile base response. Firstly, it is worth noticing that the chamber height H_c does not correspond to the actual soil layer thickness, because, during the densifing procedure in the model generation phase, the assembly has a volume reduction, therefore its maximum level droops. Consequently, the corrected height z_{max} is considered (Figure 3.5.6a).

The influence distance from the bottom is determined as $q_{b,INS}/\sigma_{v0}$ changes gradient: from Figure 3.5.6b it can be seen that this decreases with the increasing the insertion level, as far as it reaches an asymptotic value, but, at a further insertion, it starts increasing again just because of the board effect.

Herein, the variation of the influence distance ($z_{max} - L_p$) at varying n_p ratio and porosity is investigated; in particular the non-dimensional parameter n_H, which is the ratio between the influence distance and pile diameter d_p, is considered.

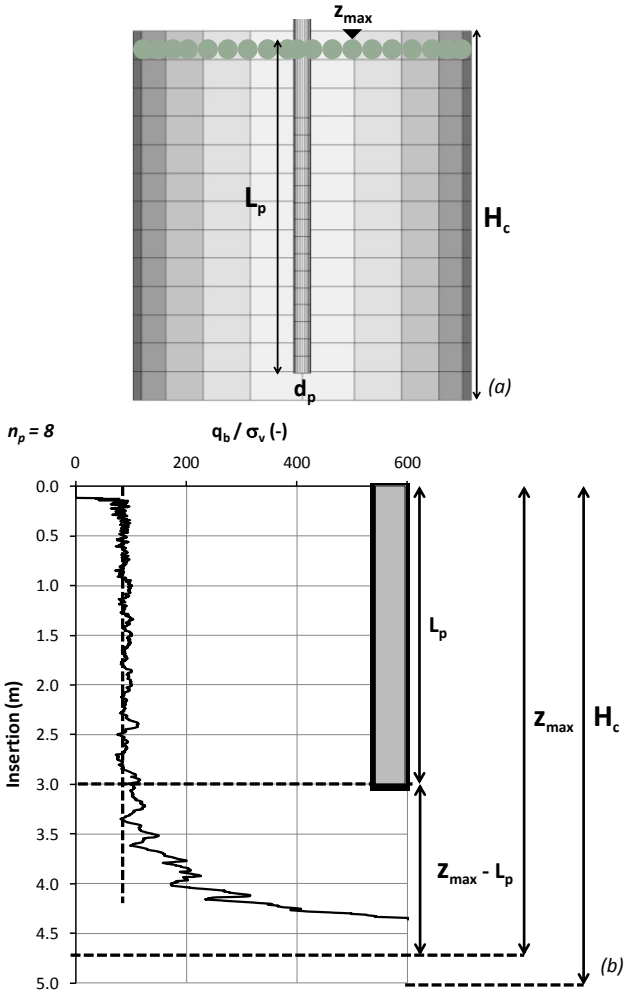

Figure 3.5.6. Scheme for n_H definition

Figure 3.5.7 shows that n_H depends on the n_p ratio, but there is not any influence of porosity. For this reason, since the minimum $n_p = 6$ has been chosen for all the following cases, n_H is fixed as 1.75.

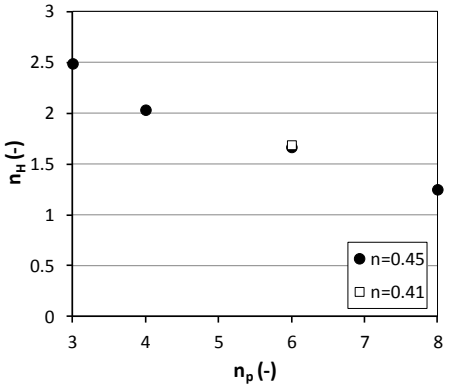

Figure 3.5.7. Variation of n_h for varying n_p and porosity

INFLUENCE OF THE BASE SHAPE

When a jacked closed-ended pile is inserted in field, a wedge-shaped rupture surface develops below the base, whatever is the base shape.

The same is not true for the jacked pile model, because the failure mechanism is affected by the limited number of particles below the base. It follows that different base shapes can give rise to different failure mechanisms, that is different base responses. In particular, at a fixed n_p ratio, the difference between the disk-shaped pile and the conical-shaped pile base resistance ($q_{b,d}$ and $q_{b,c}$, respectively) decreases at decreasing porosity: this confirms the dependence of this ratio only from the number of base/particles contacts, therefore this is exclusively a limit of the model.

These observations hail from the analysis of six cases (Cases 14,19 and 20, cases 23-25), where, for the fixed n_p = 6 and three different porosities, the insertion of jacked piles with disk-shaped and conical-shaped base is reproduced. The ratio $q_{b,d}$ /$q_{b,c}$, called α_c, for n = 0.45, 0.43 and 0.41 assumes the values 2.5, 1.6 and 1.3, respectively (Figure 3.5.8).

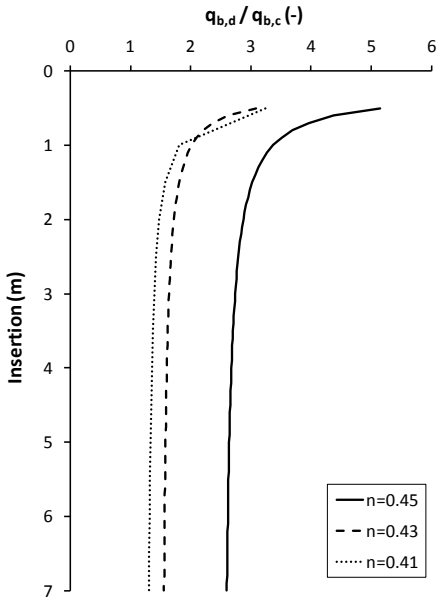

Figure 3.5.8. Ratio between disk-shaped and conical base response during insertion, for different porosities

INFLUENCE OF THE PENETRATION RATE

In §3.3 it has been shown that the amplification of the cone penetration rate by a factor 10 does not influence cone response. For the jacked pile it is important to verify that this amplification does not affect both for base and shaft resistance. Therefore, three cases with different velocities are performed for the medium dense model (n = 0.41), where the ratio between the numerical insertion rate and the standard rate, G, is equal to 1, 10 and 20 (Cases 8-10).

Regarding base response, at the first 2 m of insertion cases with G = 10 and 20 present a $q_{b,INS}/\sigma_{v0}$ much higher than G = 1; as the pile penetrates further, the ratio decreases and overlaps the curve for G = 1, for both tests. This response at low confinement levels depends on the inertia effects which rise from a too fast insertion and that get lost at the increasing depth. At the end of the insertion, the cases G = 1 and G = 10 have the same average base resistance, while for G = 20 it is about 1.25 times larger. The horizontal stresses at pile shaft for the 3 rates, instead, have a good overlapping (Figure 3.5.9). At the end of these consideration an amplification coefficient of 10, which represents a good compromise between time-consuming and analyses reliability, is chosen.

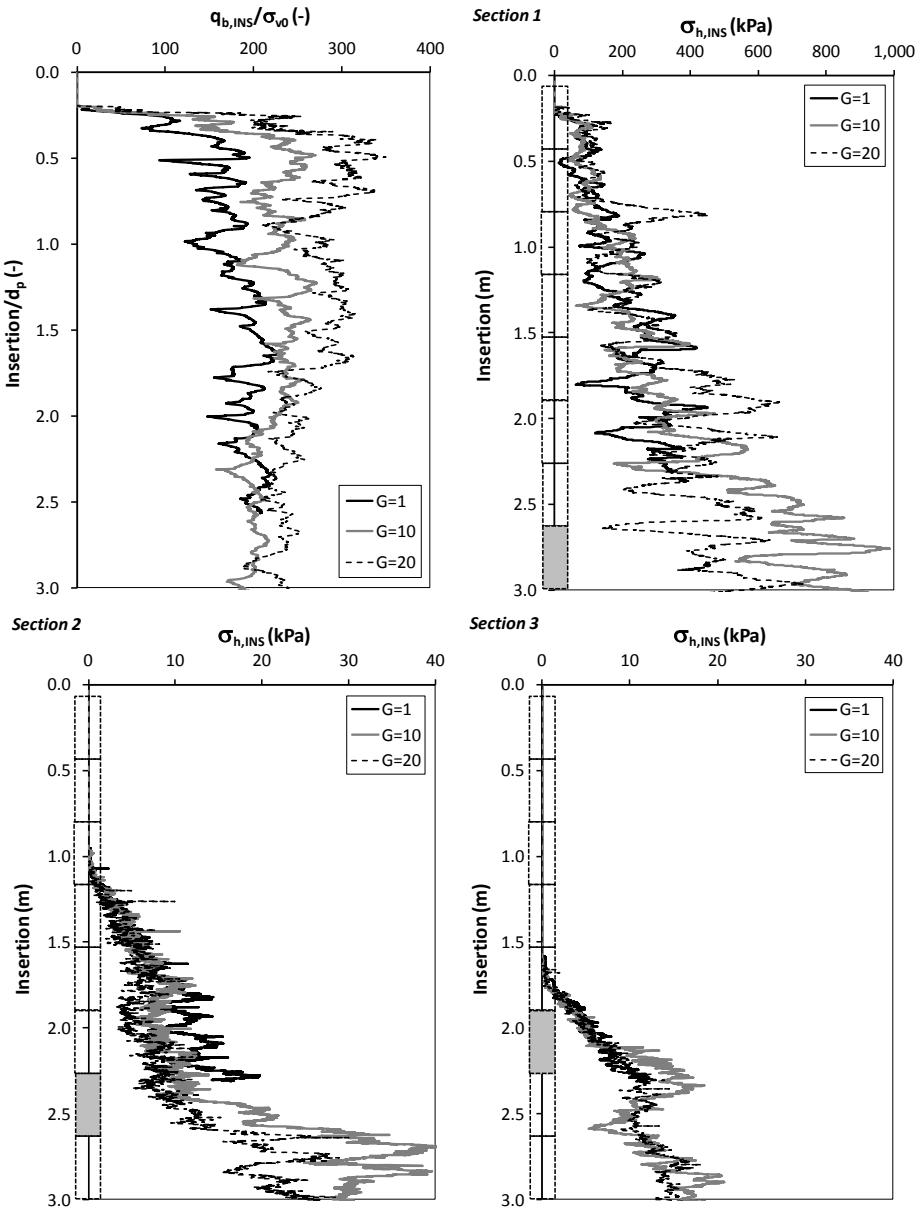

Figure 3.5.9. Normalized base resistance and horizontal stress at pile shaft during pile insertion at varying G

POROSITY, n_p AND R_d VARIATION: THE COUPLED EFFECTS

Parametric analyses for R_d and n_p have shown that the minimum values which guarantee the goodness of pile response are 20 and 6, respectively. However, these values have been determined only for n = 0.45, which corresponds to a loose state for the Hostun DE-sand. Besides, the minimum ratio R_d = 20 for n = 0.45 corresponds to n_p = 3, albeit successively n_p = 6 has been fixed as the minimum ratio.

The mutual independence of these parameters is not taken for granted at all, consequently, another set of tests is performed, in order to finally throw light on these aspects.

First of all, it is necessary to verify if the chamber size ratio is valid also for a denser soil. Therefore, the comparison between cases 10 and 11 (for which R_d is equal to 20 and 27, respectively) is reported: both base resistance and shaft resistance do not vary substantially at varying R_d, except for Section 3, where there is an evident leap after 3.50 m of insertion, but it is a difference that can be simply justified by a local effect (Figures 3.5.11 and 3.5.12).

In a second instance, it is verified if a model with n = 0.45 and $n_p > 3$ can have $R_d < 20$; with this aim tests 12-14 are performed and the results are presented in Figures 3.5.13 and 3.5.14.

The normalized base resistance for case with R_d = 15 presents an initial peak about two times the one recorded for the reference case with R_d = 20, then it decreases and two curves overlap; for R_d = 10 and 13, instead, the peak value is the same than for R_d = 15, successively, it decreases reaching a limit value about 1.6 times higher than the other cases. The horizontal stresses, instead, maintain a rather good overlap. Basing on this new results, for n = 0.45 it can be assumed an R_{dMIN} = 15.

Eventually, it is verified if $R_d < 20$ is still valid for a sand with n < 0.45. Specifically, two attempts are performed with n = 0.43 and R_d = 20, 17 and 15 (Cases 16-18). From the results presented in Figures 3.5.15 and 3.5.16, it can be noticed that both base and shaft resistances are strongly influenced by the R_d ratio, so it is not possible to adopt an R_d value lower than 20.

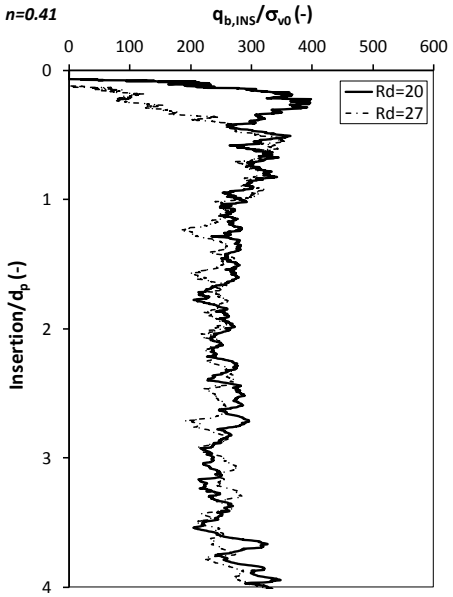

Figure 3.5.11. Base resistance for n = 0.41 at varying R_d

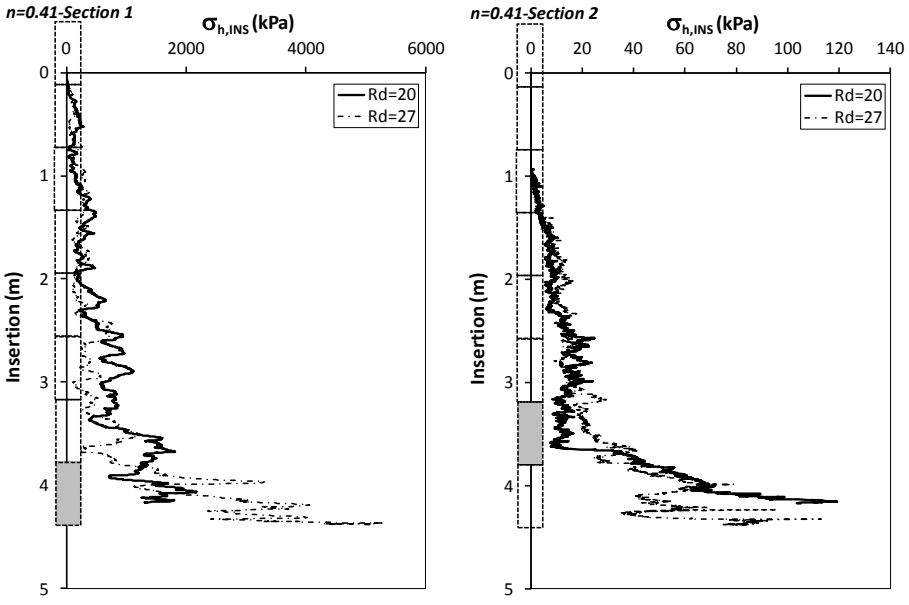

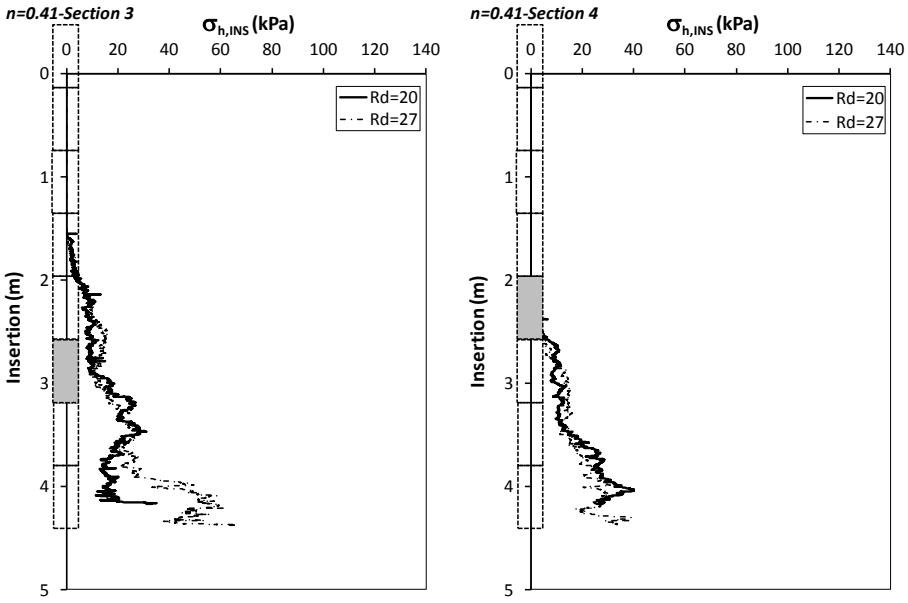

Figure 3.5.12. Horizontal stress at pile sections for n = 0.41 at varying R_d

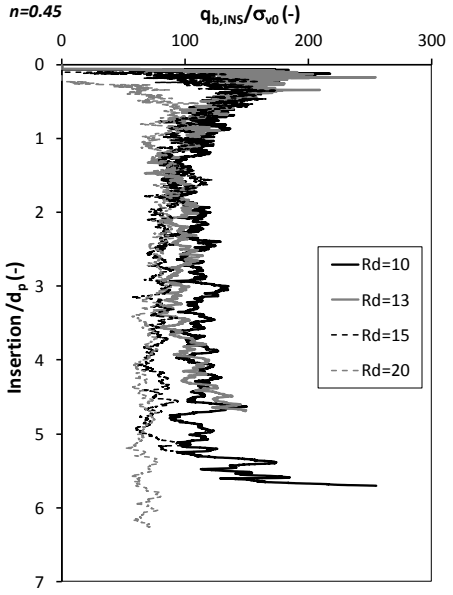

Figure 3.5.13. Base resistance for n = 0.45 at varying R_d

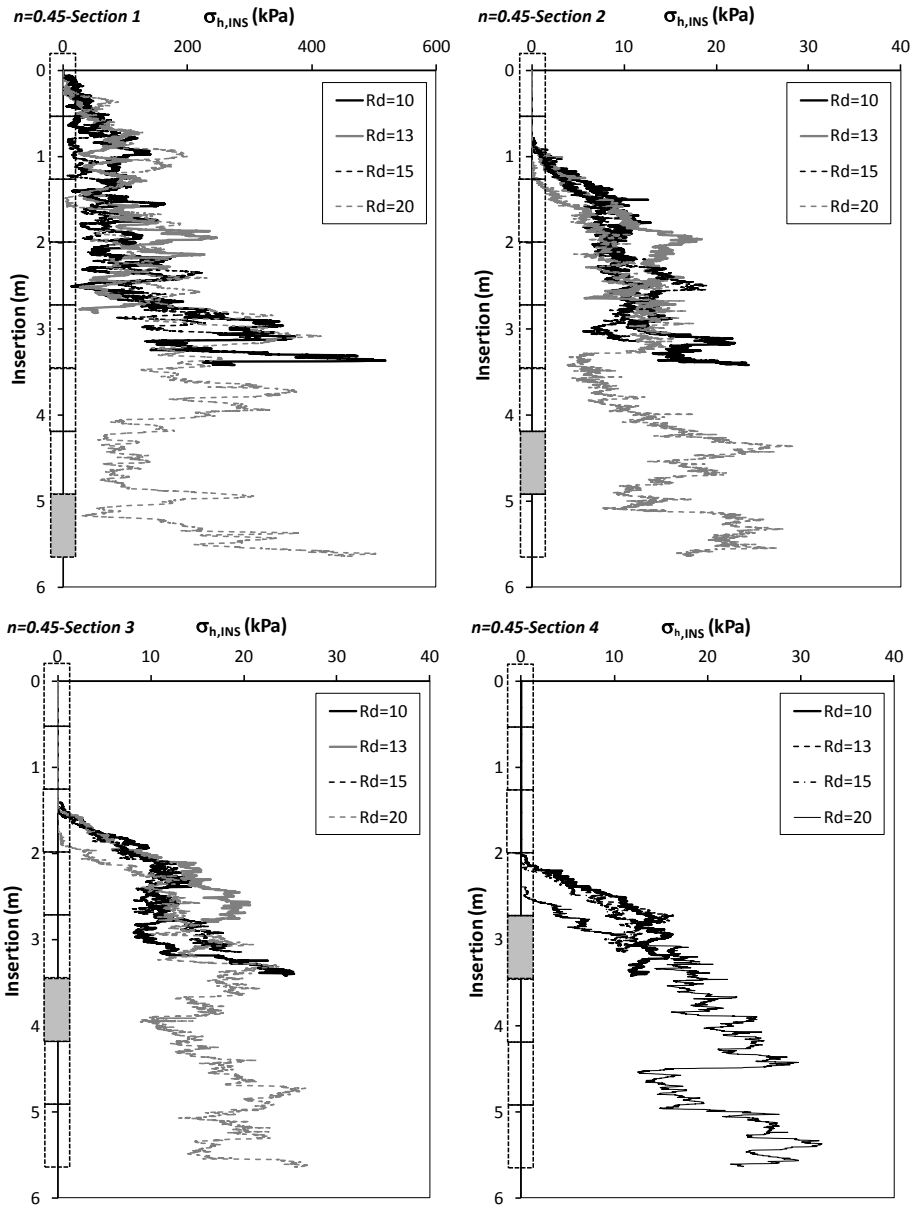

Figure 3.5.14. Horizontal stress at pile sections for n = 0.45 at varying R_d

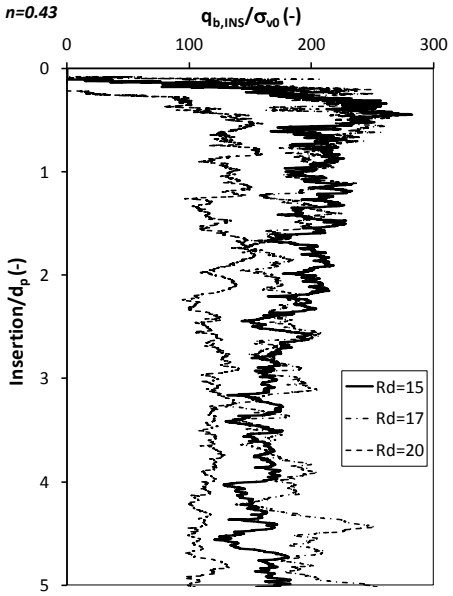

Figure 3.5.15. Base resistance for n = 0.43 at varying R_d

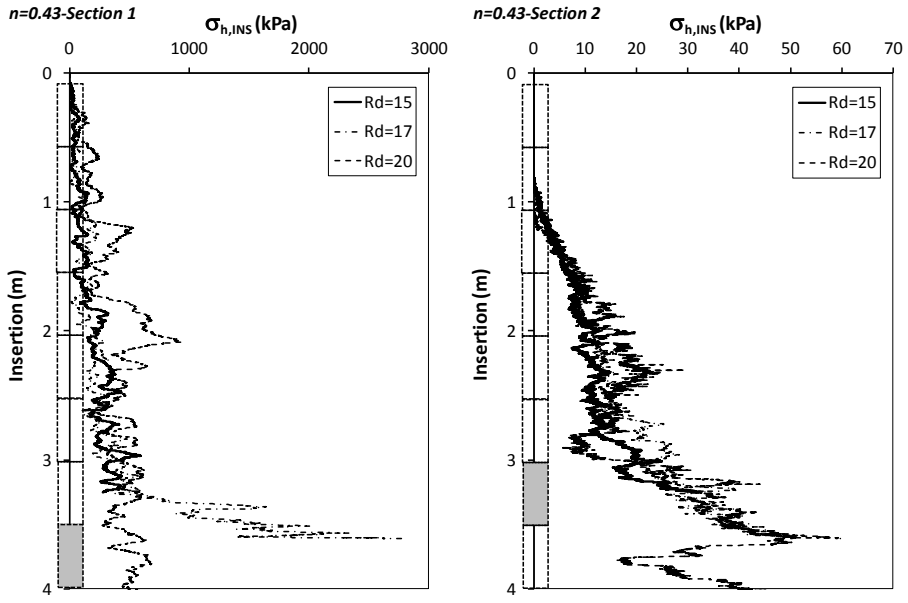

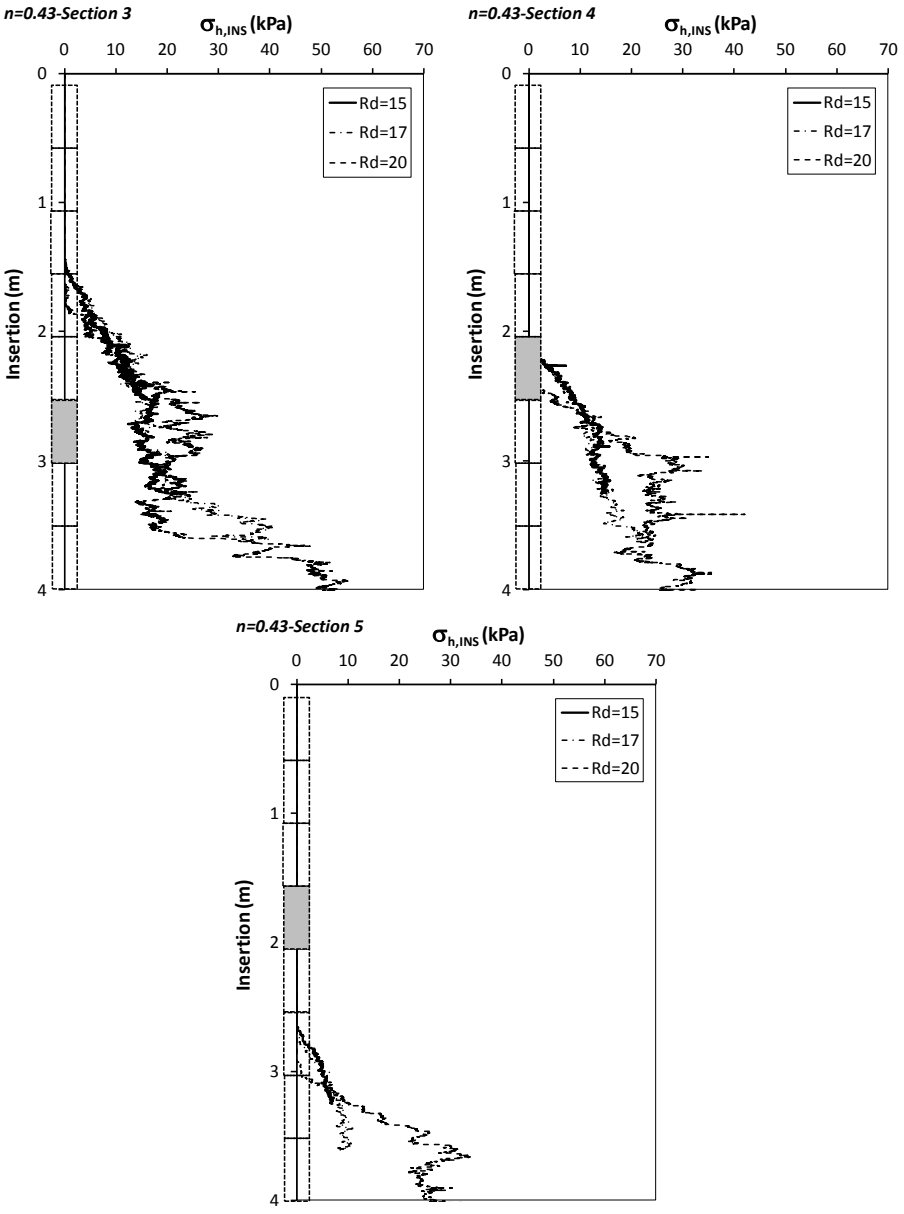

Figure 3.5.16. Horizontal stress at pile sections for n = 0.43 at varying R_d

L/D VARIATION

All the geometric parameters have been defined as the best compromise between the reliability of results and the computational effort.

However, the respect of all of these "constraints" brings to a very limited model, where the maximum pile embedment ratio is about 7.

It is clear that such a short pile is not of particular interest, therefore there is the strong need of a further simplification, in order to model much longer piles.

In §3.3 the CPTs in virtual calibration chamber are performed also in a quarter of the chamber, but it has been showed that this reduced model underestimates cone resistance, because the higher porosity in the corner causes a sensitive underestimation of cone resistance.

Herein, for the pile case, a check is done anyway, since a higher value of n_p (from 3 to 6) is considered, therefore the number of contacts between pile base and the soil below is higher than CPT. Nevertheless, Figure 3.5.17 shows a lower base resistance (about the 20%) for the quarter model, while the horizontal stress along pile sections is about the half than the complete model.

Definitively, the quarter model does not work well also for the simulation of piles installation.

The reduction of particles size could appear to be a solution to such a kind of problem, but, since the particles number increases with the decreasing diameter, the solution for the computational problem provokes itself the unfeasibility of the analysis!

Aiming to the pile embedment increase, a second attempt is done by considering a model with the complete chamber and a grain size distribution amplified at the increasing distance from pile axis r. The scaling factor SF varies with r and, in particular, the cylindrical chamber is divided into four concentric volumes, where particle radius increases with a linear law (Figure 3.5.18). The maximum SF reached in correspondence of $r = D_c / 2 = R_c$ is 1.5 times larger than the initial SF. By means of this artifice, the number of particles reduces down to about the half, but unfortunately also this approach does not work well: looking at the contact forces distributions in Figure 3.5.19, indeed, it can be noticed that there are circular chains in which contact forces are very low. Consequently, also for this case, there is a strong underestimation of base and shaft resistances measured during the jacking. From the comparisons in Figure 3.5.17, it is evident that both $q_{b,INS}$ and $\sigma_{h,INS}$ are quite lower than those for the complete chamber.

Eventually, as for cone penetration tests in VCC (§3.3), the model with the half chamber is checked. As it can be seen from Figures 3.5.20 and 3.5.21, the complete and half models exhibit quite the same response at both base and shaft, therefore the half chamber is retained to be a good approach which strongly reduces the particles number though it guarantees the reliability of the results. Thanks to this model, it is possible to double the slenderness value, so, if the maximum computable number of elements, the maximum slenderness ratio reached is 14.

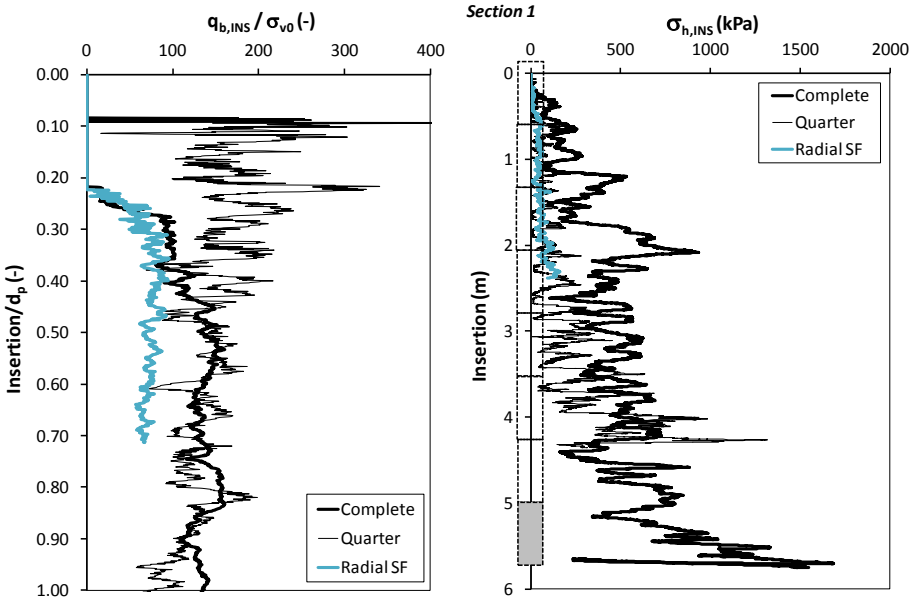

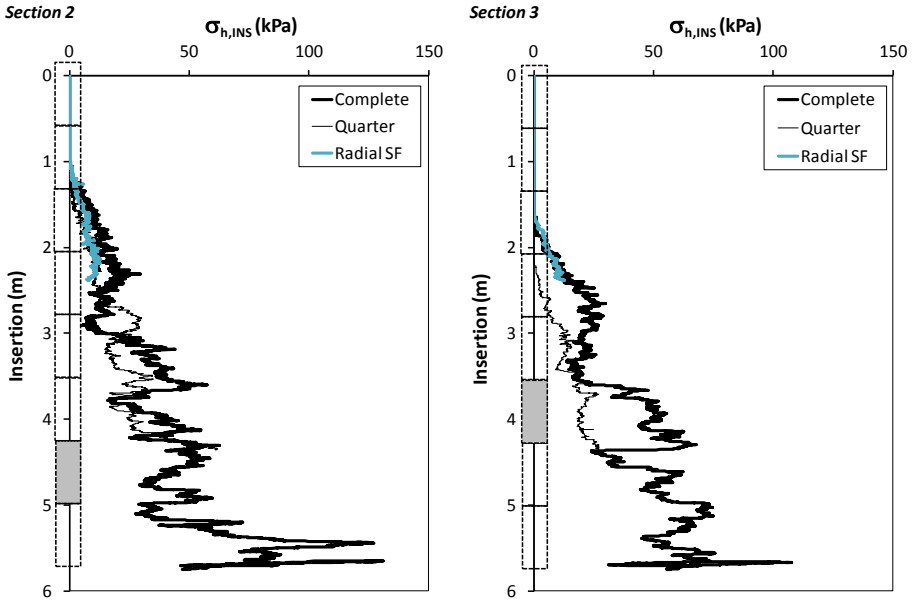

Figure 3.5.17. Normalized base resistance and horizontal stress at pile sections for Complete, Quarter and Radial scaled model

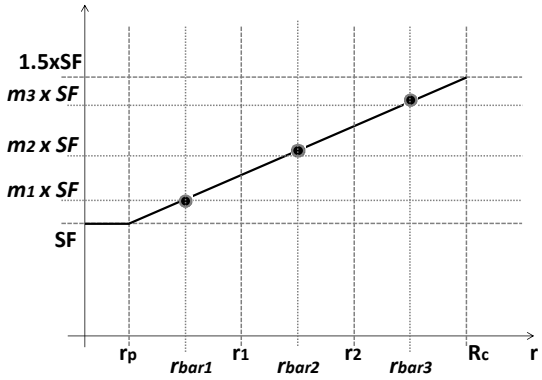

Figure 3.5.18. Radial increasing of the scaling factor

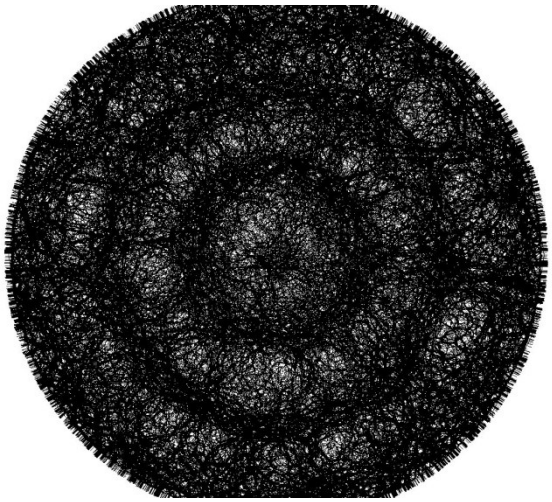

Figure 3.5.19. Contact forces distribution for the model with particle radius variable

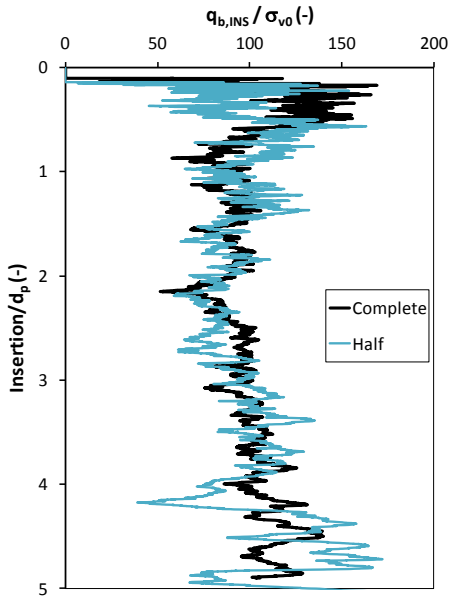

Figure 3.5.20. Base resistance for Complete and the Half model

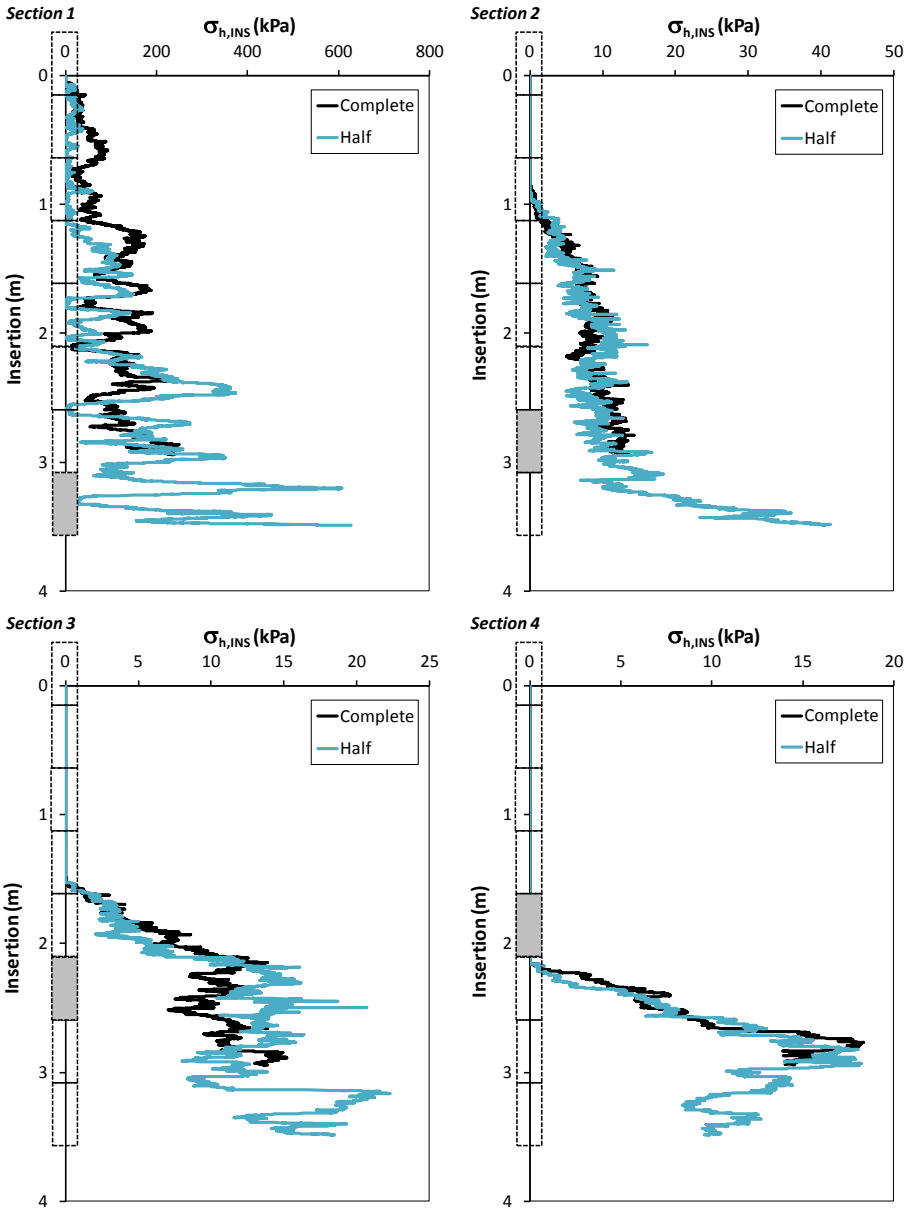

Figure 3.5.21. Horizontal stress at pile sections for Complete and Half model

3.6. Modelling of Full Displacement Pile installation

The Full Displacement Pile is realized by means of a perforation tool with a particular shape which consists of four sections: perforation, compaction, stabilization and compaction; it presents also two spirals whose one is clockwise and the other is anticlockwise (Fig. 3.6.1). This utensil can have two standard lengths, L = 3 m and L = 6 m.

The of pile is realized in 5 phases:

- *positioning and setting up drilling rig over pile position;*
- *drilling the body by pushing and rotation;*
- *drilling down to the final depth, which is limited by the height of the drill must;*
- *on reaching the final depth the tool is extracted by a rotation, with the same direction as in the insertion phase, and a pull out force; simultaneously concrete is pumped through the hollow drill stem.*
- *The cage is pushed into the fresh concrete.*

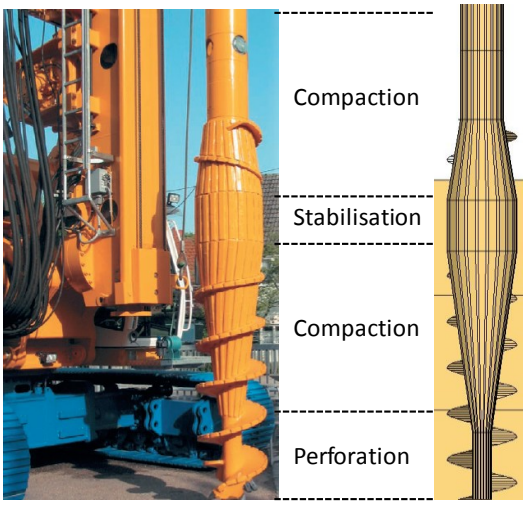

Figure 3.6.1. Full Displacement Pile

In this work the insertion of the cage is completely ignored, because it has not any influence on pile response under axial loads and on the surrounding soil state.

The installation process is modelled into two separated stages: the insertion and the extraction. During the first stage the tool is statically pushed into the ground by axial force and a clockwise torque; once the design depth is reached (Figure 3.6.2a), the pile is extracted by a traction force and a clockwise torque. Contextually the extraction, pile elements with a height of 0.20 m are generated in sequence (Figure 3.6.2b).

The new sections have the interparticle friction and the contact wall/particles stiffness the same for the jacked pile.

Because of its particular morphology, it is not possible to reproduce the installation process into the half model, since it is not possible to invoke the axial-symmetry of the problem. As a consequence, only three cases are performed with the complete chamber, summarized in Table 3.6.1. The abbreviation **S045-4** (e. g) stands for **S**crew pile in porosity n = **0.45**, with an embedment ratio equal to **4**.

Case	Name	n (-)	L (m)	d_p (m)	L/d_p (-)	SF (-)	R_d (-)	n_p (-)	G (-)	Model Type	$\#_b$ (-)
1	S045-4	0.45	2.4	0.60	4	333	20	6	10	*Complete*	433078
2	S045-14	0.45	8.6	0.60	14	333	15	6	10	*Complete*	649890
3	S041-4	0.41	2.4	0.60	4	333	20	6	10	*Complete*	433078

Table 3.6.1. Summary of the case studies for Full Displacement Piles

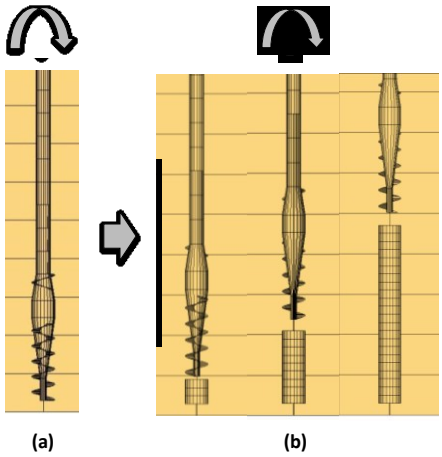

Figure 3.6.2. Full displacement pile installation phases

Regarding the insertion stage, the perforation tool has a length of 3 m, and it has fixed penetration rate and angular velocity; in particular, following the standard velocity adopted in situ, the penetration rate is v_{INS} = 0.1 m/s, while the angular velocity is ω_{INS} = 1.57 rad/s. As for the jacked pile, an amplification factor G equal to 10 is considered.

For all of the cases considered (S045-4, S045-13 and S041-4), during the penetration the variation of the pushing forces and torques at pile base and along the shaft is calculated. In Figure 3.6.3 the profiles of F_{INS} and T_{INS} with the insertion level are reported.

The profiles are very noisy as a consequence of the contacts among the blades and the particles.

After the insertion, the FDP is extracted: the pull out and the torque necessary to extract the FDP tool are plotted against the uplift normalized to the maximum pile length in Figure 3.6.4.

On the overall, the results are retained absolutely realistic, since the insertion and extraction parameters increase with the decreasing porosity and the increasing embedment ratio.

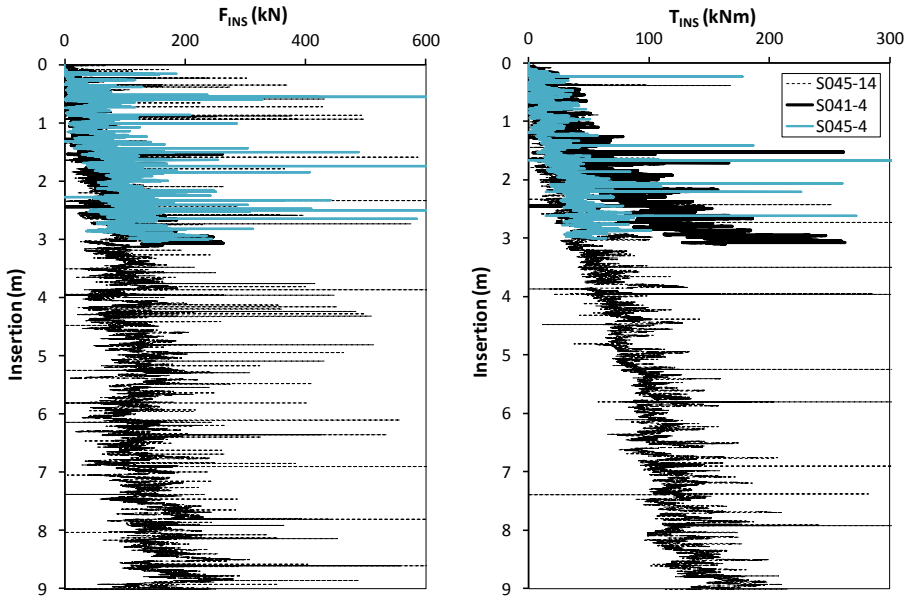

Figure 3.6.3. Pushing force and torque for FDP during the insertion stage at varying porosity and embedment

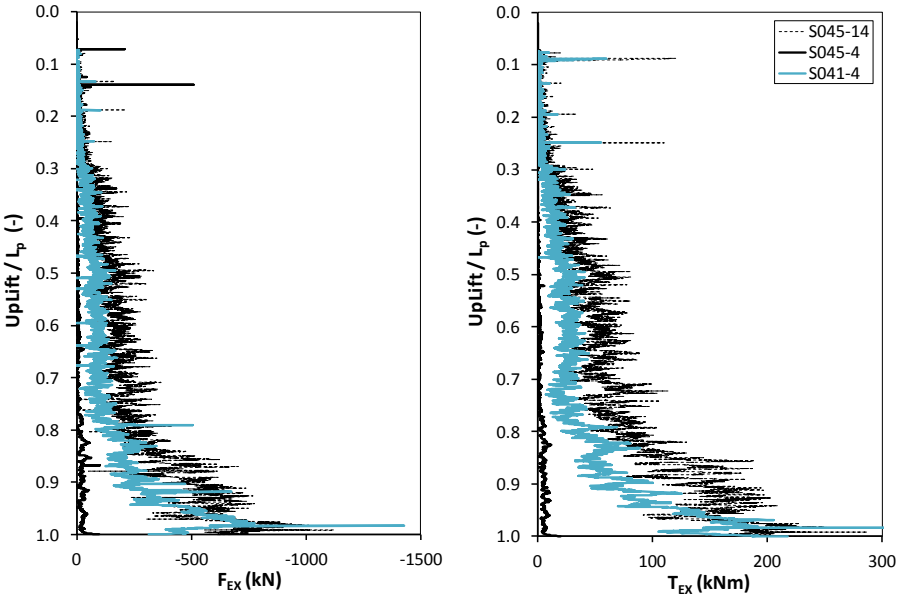

Figure 3.6.4. Pull out force and torque for FDP during the extraction stage at varying porosity and embedment

3.7. Soil state measurements

3.7.1. Definition of the Measurement Spheres

The horizontal stress, vertical stress and porosity have been measured globally and locally at the end of the gravitational phase. The global stress state is determined from the resultant stress on the bottom and the shaft of the chamber, whilst the local soil state is measured within measurement regions, also called "Measurement Spheres MS" (see §2.3.1).

Since the sizes of the MS strictly depend on the particles grain size, firstly it has been necessary to perform a sensitivity study, in order to find the diameter which guarantees the best measure possible. Herein, the measurements of the horizontal stress $\sigma_{h0,MS}$ and porosity $n_{0,MS}$ (respectively normalized to the theoretical and the input value) are reported with reference to the fixed depth z = 3.2 m, in a model with H_c = 7 m, D_c = 18 m, d_{av}^* = 0.15 m and n = 0.43. The spheres have diameters that vary from 5 times d_{av}^* up to 30 and are positioned along the x-axis with a mutual distance between the centroids equal to their radius (Figure 3.7.1.1).

As it is shown in Figure 3.7.1.2, the ratios between the calculated and the theoretical parameters are, first of all, very different from each others for $D_{MS}/ d_{av} < 10$ and tend to be equal for all the sphere at $D_{MS}/d_{av}^{*} > 18$. For this reason it is retained that the best ratio which guarantees the optimal measure is $D_{MS}/d_{av}^{*} = 20$.

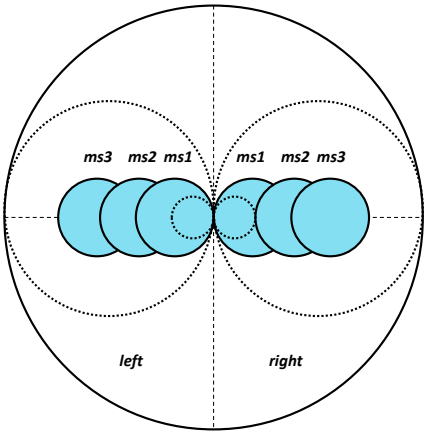

Figure 3.7.1.1. Measurement spheres position for sensitivity study

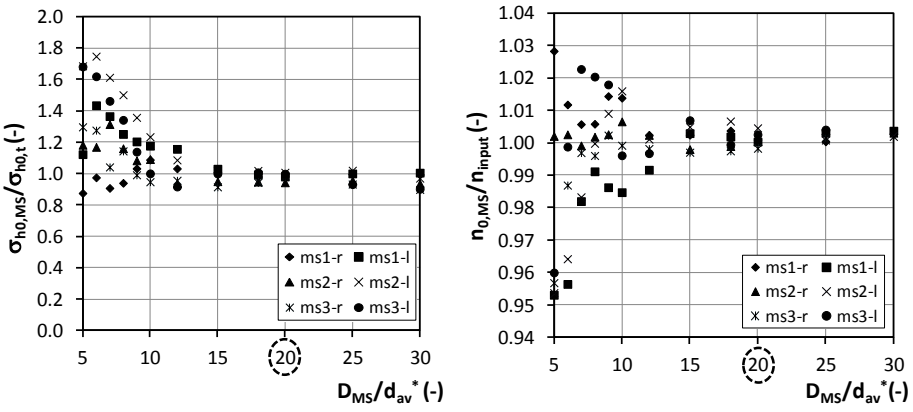

Figure 3.7.1.2. Sensitivity study for measurement spheres

3.7.2. Initial soil state

As the measurement tools have been calibrated, for all the models in Tables 3.5.1 and 3.6.1 the initial soil state is determined. Herein, the variations

of the measured initial horizontal stress $\sigma_{h0,MS}$ and vertical stress $\sigma_{v0,MS}$, normalized respectively to the theoretical stresses $\sigma_{h0,t}$ and $\sigma_{v0,t}$, and porosity $n_{0,}$ normalized to the input value n_{input}, are reported with reference to the biggest models with n = 0.45, 0.43 and 0.41 (cases 15, 19 and 20).

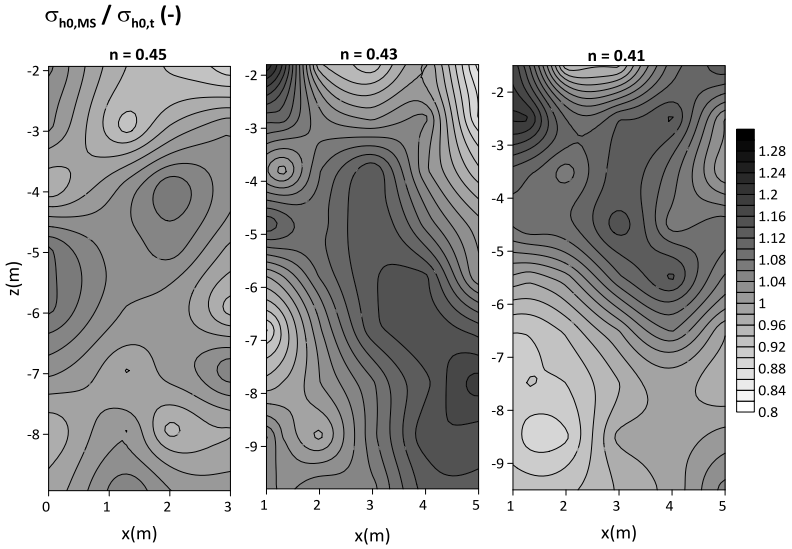

Figure 3.7.2.1. Horizontal initial stress for models with different porosity input

Figure 3.7.2.1 shows the normalized horizontal stress, whose distribution is not perfectly homogeneous because of local stress concentrations. These flaws are local contact forces concentrations that are born during the model generation and are very difficult to correct, since the number of particles is very high.

The same considerations are valid for the vertical stress (Figure 3.7.2.2) and porosity (Figure 3.7.2.3).

Literature offers several procedures for generating homogeneous samples, for example by generating the assembly layer by layer; nevertheless, it is practically impossible to apply these techniques to such big models which consist of about 600000 particles, because of the computational overwork.

For this reason the initial soil state of the model is considered rather satisfactory.

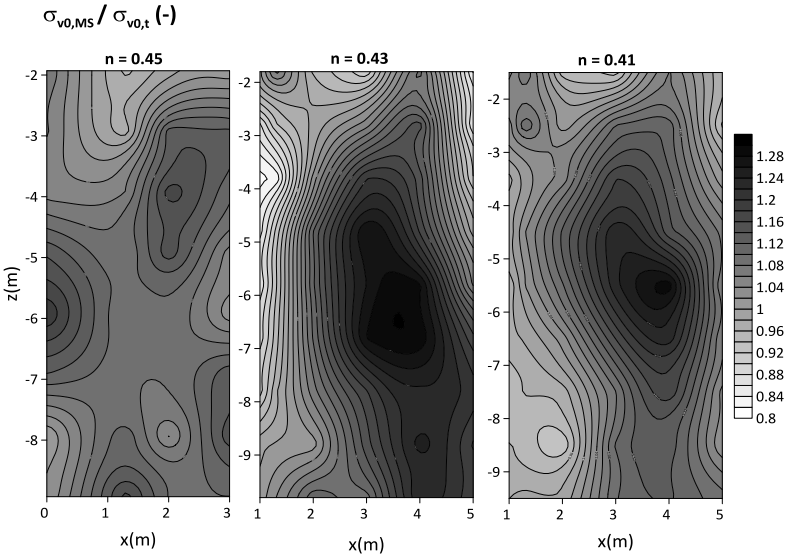

Figure 3.7.2.2. Vertical initial stress for models with different porosity input

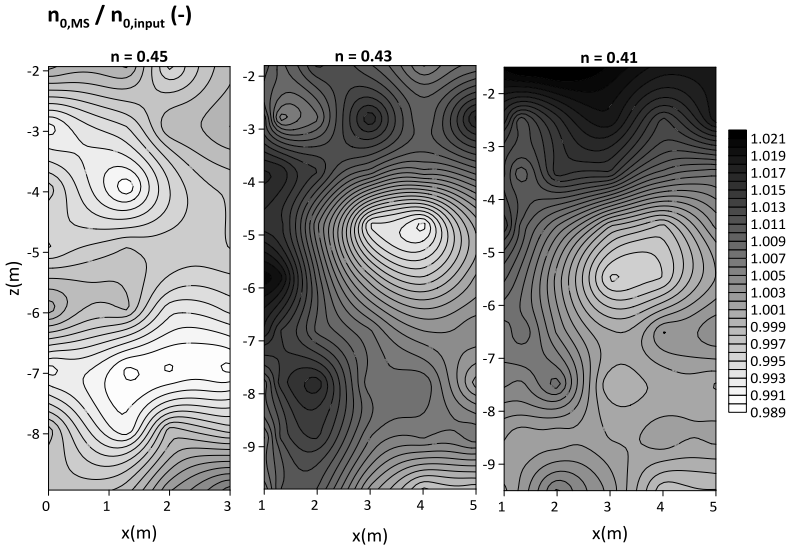

Figure 3.7.2.3. Measured porosity distribution for models with different porosity input

3.8. Concluding remarks

In this Chapter the calibration of the DE-model, from the laboratory triaxial test to the installation of a pile in situ, has been dealt with. As a result, it is evident that the Discrete Element Model allows to simulate all the stages of the pile design: the investigations in laboratory and onsite before, then the pile realization itself. It is likewise evident that the calibration of a DE-soil is a quite delicate phase, because of the differences of the model sand from the actual one. The model that has been chosen has very strong simplifications (spherical particles, simplified grain-size distribution, fixed rotations of the particles, elastic linear contact constitutive law), for this reason a great care is needed in selecting the micromechanical parameters that make the model response definitively matching with reality.

Concerning the field problem, the recommendations for the cone penetration tests in laboratory have been developed to the full scale tests; all the good-working suggestions for the CPT modelling have been improved and adapted to the pile case.

The software PFC3D allows a very realistic modelling of the complete installation process for both jacked and screw pile. Anyway, the analysis of piles installation comes from the constant need to make a compromise between time-consuming, maximum number of particles manageable, results reliability. All the available computational sources have to be capitalize on performing an installation process as realistic as possible.

After the calibration phase described in this Chapter, in the following the analyses of jacked and screw pile installation and loading into sands with different initial conditions will be presented. In particular, the focus will be on the stress variation along the pile and in the surrounding soil during these different stages.

CHAPTER 4. NUMERICAL ANALYSIS OF THE INSTALLATION AND LOADING PROCESS

4.1. Introduction

In this Chapter the analyses of the whole installation and loading process for jacked and screwed piles in different sandy soils are presented. Table 4.1.1 summarizes the case studies for which an abbreviation, as for the screw piles in Table 3.6.1, is adopted.

Case	Name	n (-)	L (m)	d_p (m)	L_p/d_p (-)	SF (-)	R_d (-)	n_p (-)	G (-)	Model Type	$\#_b$ (-)
1	J045-6	0.45	5.69	0.90	6	500	20	6	10	*Complete*	518137
2	J041-6	0.41	5.48	0.90	6	500	20	6	10	*Complete*	518137
3	J045-13	0.45	7.90	0.60	13	333	15	6	10	*Complete*	649890
4	J043-14	0.43	8.45	0.60	14	333	20	6	10	*Half*	653264
5	J041-14	0.41	8.25	0.60	14	333	20	6	10	*Half*	653264
6	S045-4	0.45	2.4	0.60	4	333	20	6	10	*Complete*	433078
7	S045-14	0.45	8.6	0.60	14	333	15	6	10	*Complete*	649890
8	S041-4	0.41	2.4	0.60	4	333	20	6	10	*Complete*	433078

Table 4.1.1. Summary of the case studies for jacked and screw piles

4.2. Insertion

4.2.1. Jacked piles

As discussed in §3.5, the insertion of the jacked pile is executed by the application of a constant penetration rate to the pile element. During this stage, the developing of base and shaft response with the penetration level is continuously determined.

Herein, the effects of the insertion process at base and along pile shaft are presented.

EFFECTS AT PILE BASE

The profiles of the unit base resistance during insertion $q_{b,INS}$ for all the cases (summarized in Table 4.1.1) are shown in Figure 4.2.1.1: as expected, $q_{b,INS}$ increases with the insertion level and at decreasing porosity.

The reported profiles are, undoubtedly, rather good from a merely qualitative point of view. Nevertheless, a check also from a quantitative point of view is needed. Since the static insertion of a jacked pile provokes a continuous failure process in the soil below, it is possible to compare the numerical values of the end-bearing factor $N_{q,INS}$ with the theoretical formulation for N_q at failure by Fleming *et al.* (1992) – see §1.2-. Cases J045-6 and J041-6 are not explicitly considered, since their $q_{b,INS}$ profiles overlap those for J045-13 and J041-14, respectively.

As it can be noticed from Figure 4.2.1.2, $N_{q,INS}$ has a very good match with the theoretical value for J045-13 and J043-14; slightly higher values are obtained for J041-14. It is believed that the differences can be attributed to the choice of an average operative relative density for the evaluation of $N_{q,INS}$, while the actual porosity profile of the model is decreasing with depth (Figure 3.7.2.3).

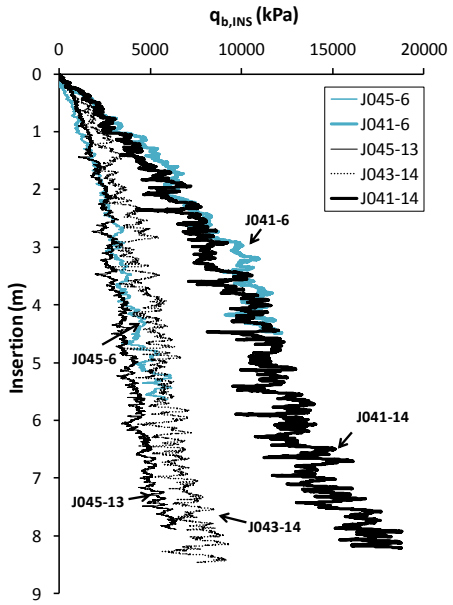

Figure 4.2.1.1 End-bearing resistance during insertion for jacked piles

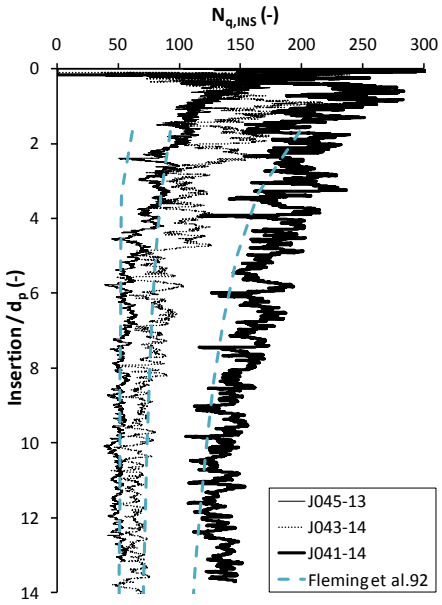

Figure 4.2.1.2. Comparison between bearing capacity factors deduced from the analysis ($N_{q,INS}$) and by theory according to Fleming *et al.* 1992

EFFECTS AT PILE SHAFT

During pile insertion, the horizontal stress $\sigma_{h,INS}$ on pile sections is calculated, as well. Once introduced the distance h between pile tip and the barycentre of generic sections, it is possible to plot the stress variation for increasing pile penetration at different values of h/R, where R is the pile radius. At the completion of the insertion stage, the horizontal stress $\sigma_{h,INS}$ for pile sections is plotted against the depth of each barycentre z_G.

Figures 4.2.1.3a, 4.2.1.4a and 4.2.1.5a show the variation of $\sigma_{h,INS}$ with the insertion level for cases J045-13, J043-14 and J041-14, respectively, with reference to some selected pile sections.

The horizontal stress during insertion increases with the penetration and, in particular, for h/R = 1 it assumes much larger values than the above sections, since it is affected by the failure mechanisms at pile base. This finding qualitatively agrees with the results of centrifuge tests presented by Bruno and Randolph (2000),White and Lehane (2004) and the trend observed in the field by Lehane (1992) and Chow (1997).

Figures 4.2.1.3b, 4.2.1.4b and 4.2.1.5b report the $\sigma_{h,INS}$-profile with depth. As it can be seen, the calculated values are larger than the geostatic value at relatively small depths (that means, at low confining stress) for the first two cases. For J041-14, $\sigma_{h,INS}$ substantially increases with the depth, and is larger than the geostatic value.

Close to pile base, in all the cases a sudden increase is observed.

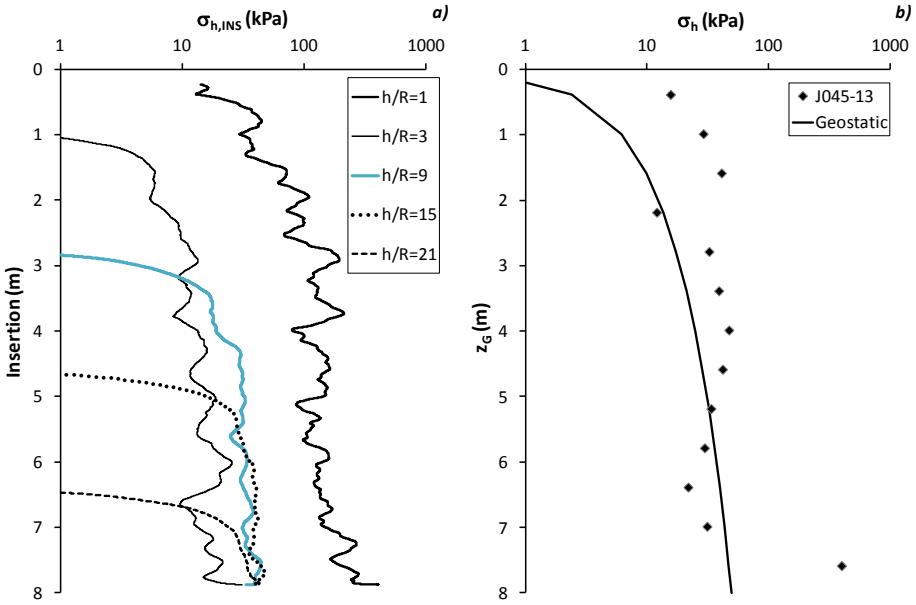

Figure 4.2.1.3. Horizontal stress variation during insertion (a) and at the end of insertion (b) for Case J045-13

Figure 4.2.1.6 reports the ratio between the calculated horizontal stresses at the end of pile insertion at a given depth and the geostatic values at the same depth. The following comments can be made:

- The distribution of horizontal stress at the end of the pile insertion is depending on the soil porosity (or relative density): for loose soil, an increase is observed at shallow depths ranging between z_G/L_p = 0.2÷0.3 (i.e. low confining stress) and close to pile base (z_G/L_p = 0.9÷1.0); for the remaining part of the pile, no changes have been deduced from the analyses;

- For medium dense soil, on the contrary, a substantial increase over the entire pile length is obtained, probably due to the influence exerted by the pile base mechanism not vanishing just above.

Similar results are obtained with shorter piles (L_p/d_p = 6) as shown in Figure 4.2.1.7.

Overall, the findings are consistent with those experimentally obtained by the centrifuge tests (White and Lehane, 2004), already introduced in §1.3.1.

Definitively, it is possible to confirm that the present numerical results are able to reproduce, at least qualitatively, what found by dedicated experiments.

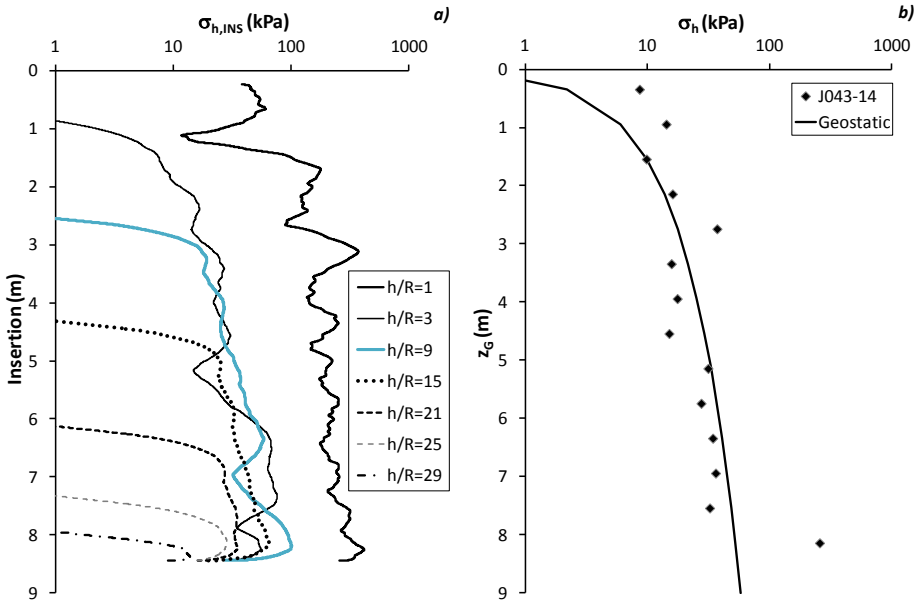

Figure 4.2.1.4. Horizontal stress variation during insertion (a) and at the end of insertion (b) for Case J043-14

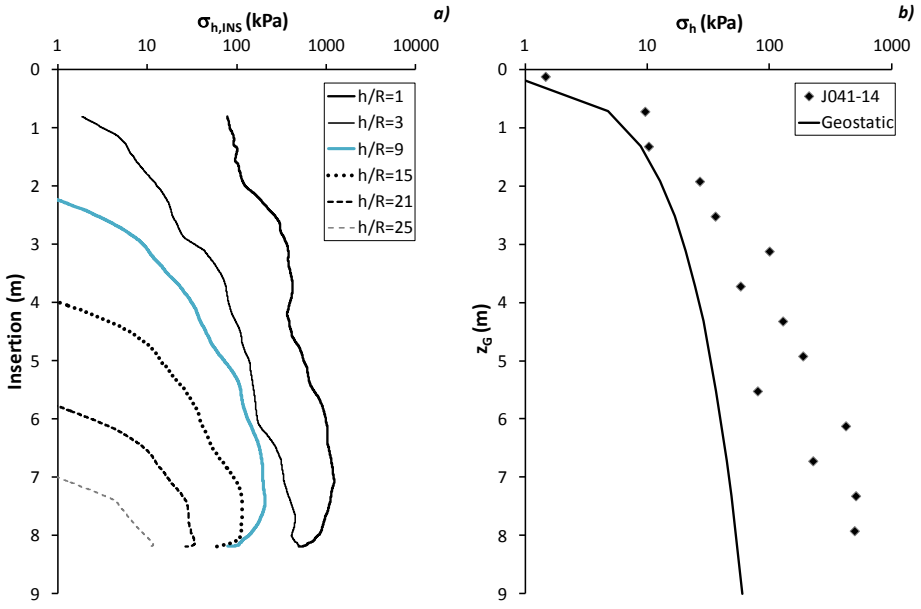

Figure 4.2.1.5. Horizontal stress variation during insertion (a) and at the end of insertion (b) for Case J041-14

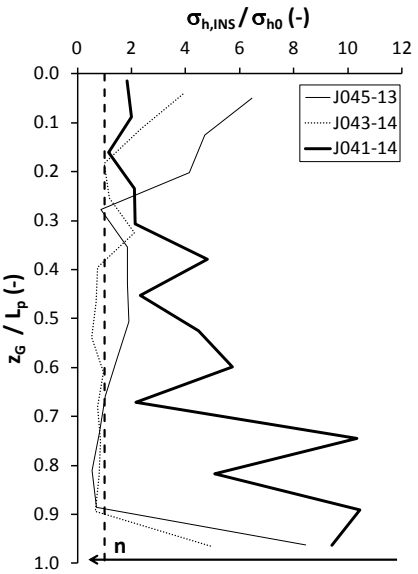

Figure 4.2.1.6. Horizontal stress at the end of insertion for J045-13, J043-14 and J041-14

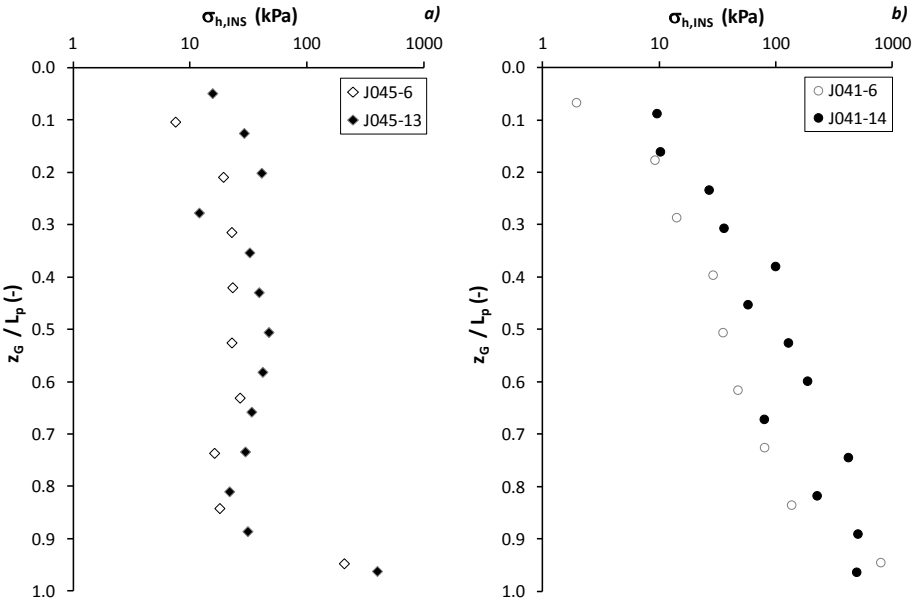

Figure 4.2.1.7. Horizontal stress at the end of insertion at varying embedment for n = 0.45 and n = 0.41

EFFECTS IN THE SOIL MASS IN TERMS OF STRESS CHANGES

In the following figures the stress ratio contours are reported (horizontal stress, Figure 4.2.1.8; vertical stress, Figure 4.2.1.9; mean stress, Figure 4.2.1.10) as calculated in the soil mass at the end of the insertion stage.

In loose soil (cases J045-13 and J043-14), at pile base z = L_p an increase of all the stresses is calculated with respect to the geostatic values. Clearly such an increase tends to become smaller for increasing horizontal distance x. The same applies, although with different values, moving from the surface down to depth. In the middle part of the pile a reduction of the horizontal stresses (that means, smaller than the geostatic value) is observed, similar to what previously observed with reference to the pile shaft.

Such a reduction is also observed in terms of vertical stresses and mean stresses at a distance x ≈ 1 to 2 m, about (1÷3)d_p from pile axis.

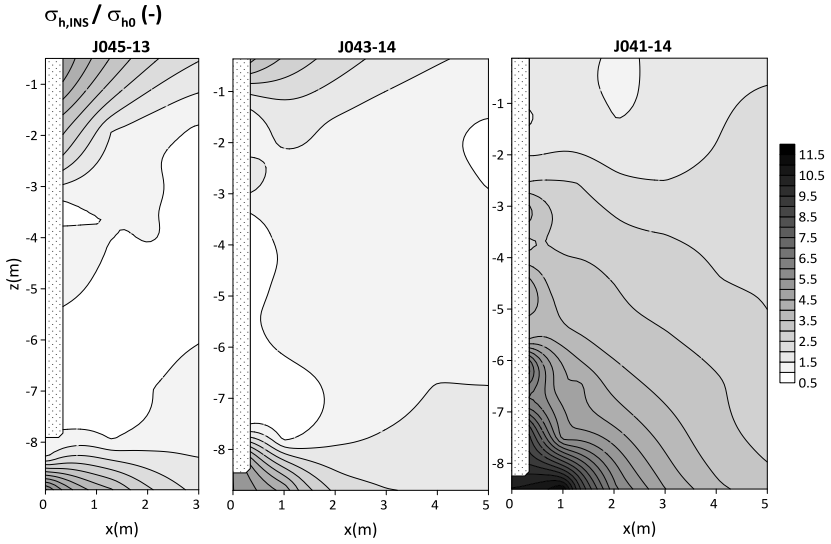

Figure 4.2.1.8. Horizontal stress at the end of insertion for J045-13, J043-14 and J041-14

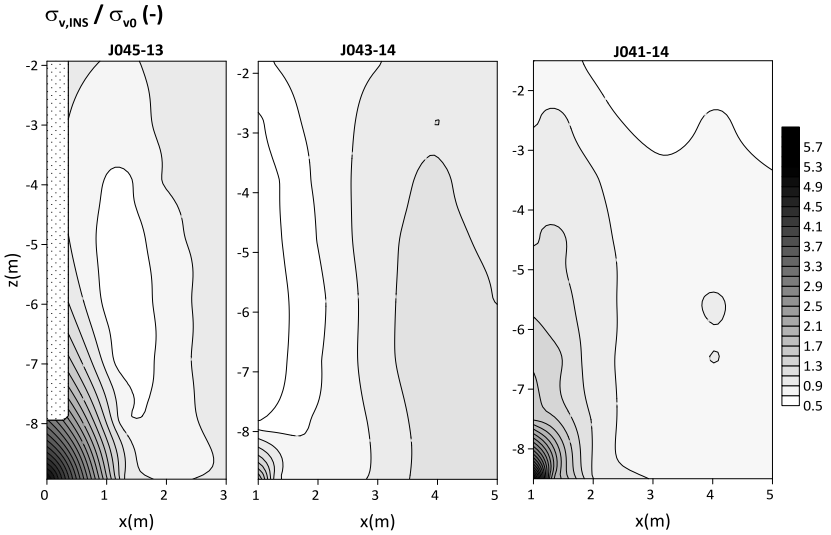

Figure 4.2.1.9. Vertical stress at the end of insertion for J045-13, J043-14 and J041-14

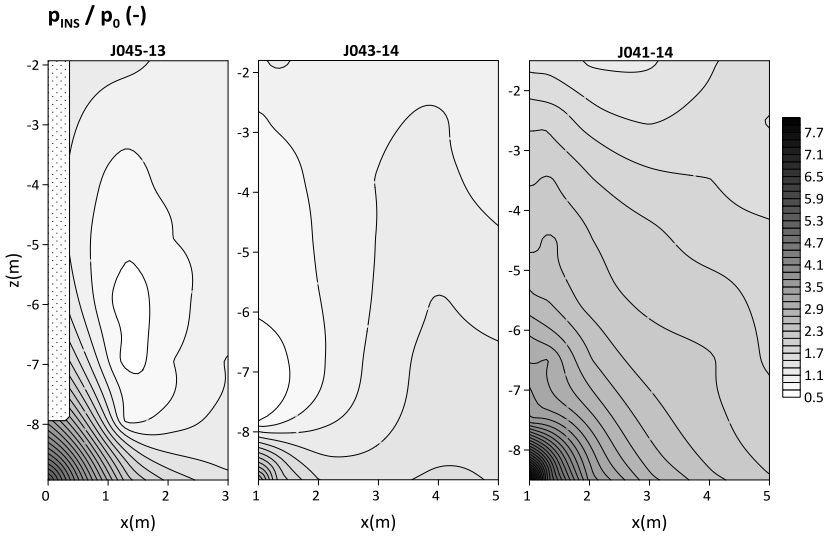

Figure 4.2.1.10. Mean stress at the end of insertion for J045-13, J043-14 and J041-14

In medium dense soil, different results are obtained: no reduction of all the stresses are revealed from the analysis, with the only exception of vertical stress into a limited volume of soil close to surface (Figure 4.2.1.9).

The peak values of the stresses ($\sigma_{h,INS}$, $\sigma_{v,INS}$ and p_{INS}) below pile base at the end of pile insertion are consistent with the results from FEM analyses provided by Dijkstra (2009) and Sheng *et al.* (2006), already discussed in §1.3.3. As for the surrounding soil, these latter do not show the different mechanisms occurring into the three aforementioned zones.

In Figure 4.2.1.11 is reported the variation of $\sigma_{h,INS}$ increment during the insertion, calculated at a radial distance x_{MS} = 1.30 m from pile shaft, in correspondence of two different depths for cases J045-13, J043-14 and J041-14.

For all the cases, the horizontal stress $\sigma_{h,INS}$ increases with the insertion level as far as pile tip is ≈ $2d_p$ above the measurement point. As the pile is jacked past the location, a sharp decrease is noticed and, when the tip is at ≈ $2d_p$ below the point, $\sigma_{h,INS}$ reaches the geostatic stress for loose sand (Cases J045-13 and J043-14) and an asymptotic value larger than the geostatic one for the medium dense sand.

It is clear that the mutual position between the insertion level at which $\sigma_{h,INS}$ assumes the peak value and position of the measurement point is not influenced by soil porosity (or relative density), but it just depends on pile diameter. Specifically, the peak stress value is recorded when the pile is above

the point. This evidence is in contrast with the numerical results reported by Jiang *et al*. (2006) for which the maximum stress level is reached when the pile overcomes the measurement point – see §1.3.3 –.

Definitively, these findings highlight the real capability of numerical analyses to well capture the so called 'friction fatigue' phenomenon (Heerema, 1980) or 'h/R effect' (Bond and Jardine, 1991) .

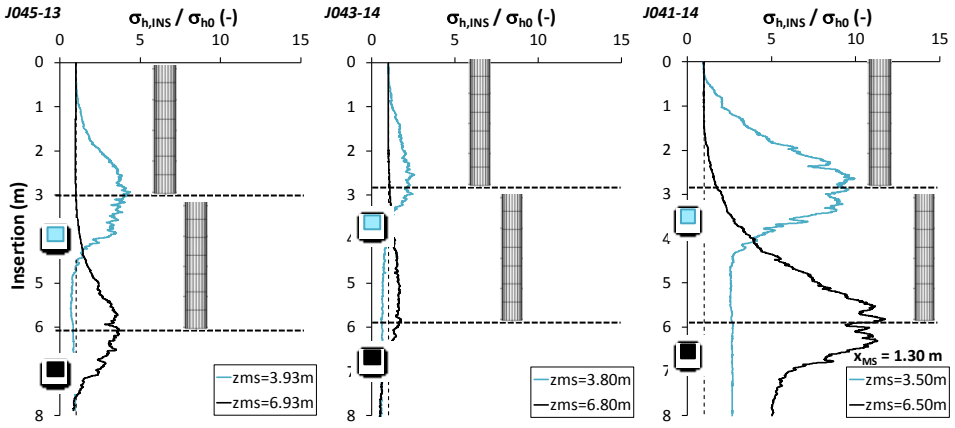

Figure 4.2.1.11. Horizontal stress variation during the insertion at a distance x_{MS} = 1.30 m from pile shaft for J045-13, J043-14 and J041-14

4.2.2. Full displacement piles

Details about the way FDP installation process has been implemented are reported in §3.6. Herein, some selected results are presented in terms of the insertion energy and the effects produced in the soil mass.

INSERTION ENERGY

During the screw penetration, the pushing force and torque are recorded during the analyses. The results are plotted in Figure 3.6.3 against the insertion level.

Van Impe (1994) proposes a formulation for the insertion energy of displacement screw piles as a function of the penetration rate v_{INS} (m/min), the angular velocity ω_{INS} (rev/min), the insertion force F_{INS} (kN), the insertion torque T_{INS} (kNm) and the cross sectional area of pile A_b (m^2):

$$E_{INS} = \frac{F_{INS} \cdot v_{INS} + T_{INS} \cdot \omega_{INS}}{A_b \cdot v_{INS}} \qquad (4.2.2.1)$$

In Figure 4.2.2.1 the obtained results for the installation of two screw piles in sandy soils at different porosities are reported.

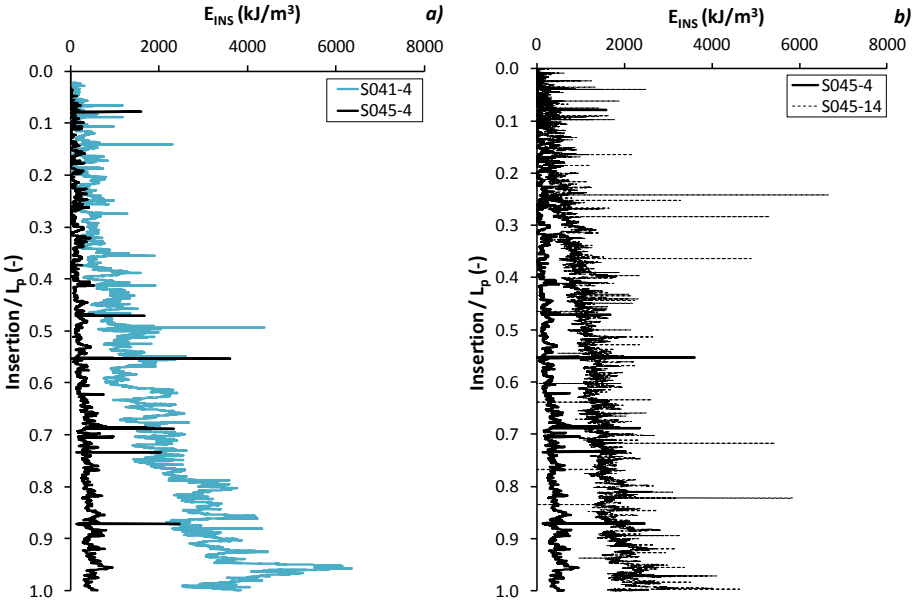

Figure 4.2.2.1. Insertion energy for S045-4, S045-14 and S041-4, from Van Impe (1994)

As expected, the installation energy increases with the insertion level (because of the soil stress increase) but decreases in looser soils.

Bottiau *et al*. (1998) have shown that the energy needed to insert a cone penetrometer during a CPT test can be reasonably assumed equal to the penetration resistance (measured in kNm/m^3 or kJ/m^3). Hence, from CPT profiles reported in §3.4 for different initial porosities, it is possible to calculate the ratio between the insertion energy for the FDP and for the cone as E_{INS}/q_c.

In Figures 4.2.2.2 is reported the values assumed by this ratio against the normalized insertion. In particular, it can be noticed that E_{INS}/q_c is practically independent from porosity and increases with the increasing insertion.

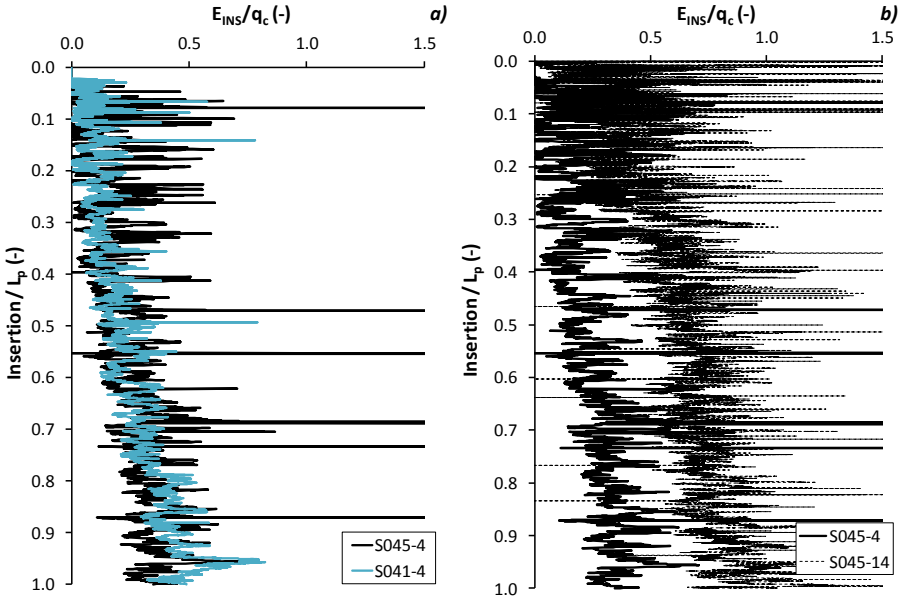

Figure 4.2.2.2. Insertion energy on cone resistance for S045-4, S045-14 and S041-4

EFFECTS AT PILE SHAFT

For the full displacement pile the variation of the horizontal stress during the insertion is calculated, as well. Figures 4.2.2.3a and 4.2.2.4a show the variation of $\sigma_{h,INS}$ calculated at each pile section (Figure 3.6.1) against the insertion level for cases S045-14 and S041-4, respectively.

For section 1 (the perforation, called S1) $\sigma_{h,INS}$ assumes very high values for the first 1 m of penetration, then it start decreasing with the insertion level, till it reaches the geostatic stress for the loose case, whilst for the medium dense sand, it tends to an asymptotic value larger than the geostatic one.

Section 2 (the compaction, called S2) determines for both cases the highest stress increment. For S045-14 the calculated $\sigma_{h,INS}$ is initially increasing with the insertion, then, as the utensil is completely inserted into the soil, it maintains a constant value. For S041-4, instead, $\sigma_{h,INS}$ is continuously increasing and, as expected, with values systematically higher than in the previous case.

On section 3 (the stabilization, called S3) $\sigma_{h,INS}$ is practically constant with depth for both cases S045-14 and S041-4 and higher than the geostatic stress.

Section 4 (the compaction, called S4) determines the same effects in terms of stress change as for S3.

Moreover, Figures 4.2.2.3b and 4.2.2.4b report the horizontal stress distribution at the end of the insertion stage, as a function of z_G. For case S045-14 it can be seen that the highest increase is in correspondence of the utensil body; at shallow depths (i.e. low confining stress) there is no substantial change with respect to the geostatic stress state (with the exception of one point very close to surface) while for depths ranging between 2.5 ÷ 5.5 m a significant reduction of σ_h is observed.

For case S041-4 the only information to be derived from the analysis is the stress increase on the utensil, since the model is very short.

The same results for S045-14 and S041-4 are compared in Figure 4.2.2.5.

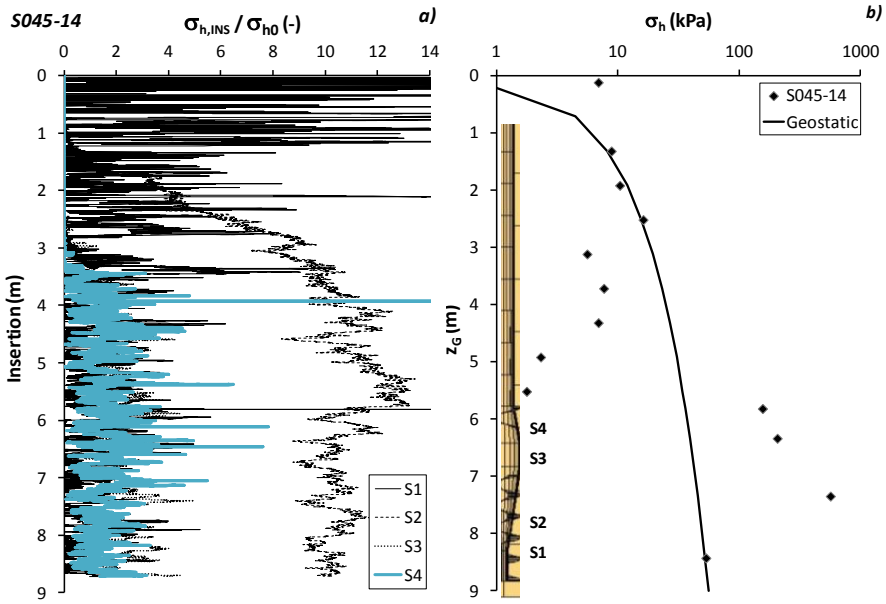

Figure 4.2.2.3. $\sigma_{h,INS}$ variation during insertion (a) and at the end of insertion (b) for Case S045-14

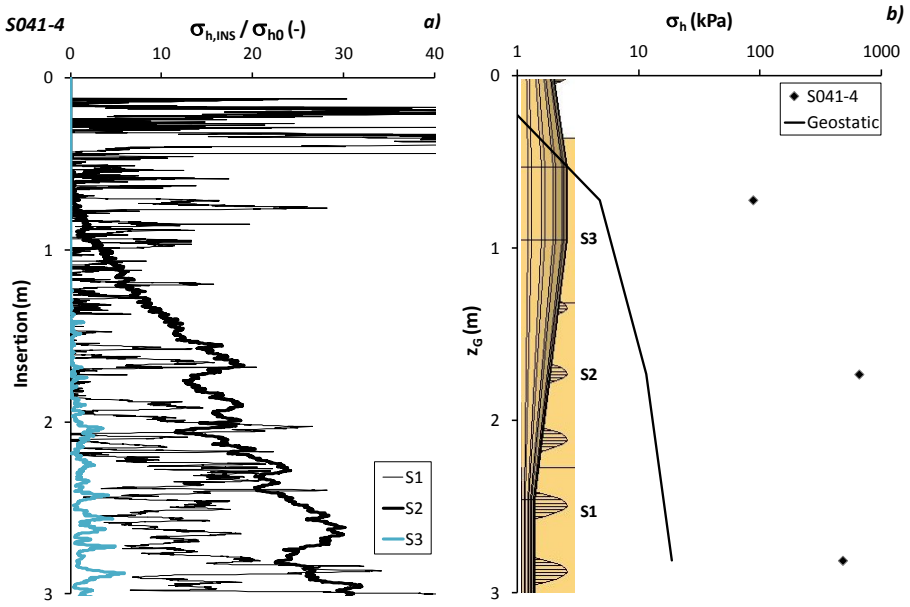

Figure 4.2.2.4. $\sigma_{h,INS}$ variation during insertion (a) and at the end of insertion (b) for Case S041-4

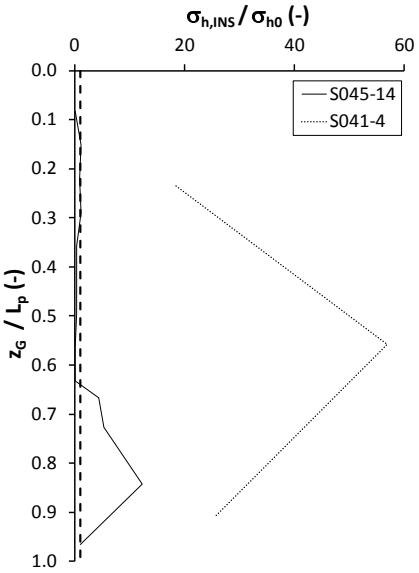

Figure 4.2.2.5. $\sigma_{h,INS}$ variation at the end of insertion for Cases S045-14 and S041-4

EFFECTS IN THE SOIL MASS IN TERMS OF STRESS CHANGES

Herein, some selected results (namely, cases S045-14 and S041-4), in terms of stress distributions at the end of insertion, are reported.

In Figure 4.2.2.3 a)-d) the normalized (to the geostatic values) horizontal stress changes in the planes (x,z) and (y,z) are shown.

As for jacked piles, the insertion causes three stress zones: the first one, around the base, where the horizontal stress is increased; the second one, at shallow depths, where the stress has an amplification nearby surface which reduces at the increasing confinement level; in the middle there is a zone where soil is decompressed.

For S041-4, as expected there is a stress increase higher than for loose sand, which diminishes with the increasing distance from the section, though it maintains higher values than the geostatic. For both cases the peak values are calculated in correspondence of the compaction section; this is consistent with the results from FEM analyses about the insertion of the FDP tool provided by Pucker *et al*. (2012).

The vertical stress variation for case S045-14 (Figure 4.2.2.4a) has a strong reduction at pile shaft, at 3.5 m < z < 6 m, that gradually reduces as the radial distance x from pile axis increases, till it reaches the geostatic values at about x = ± 3 m.

For S041-4 (Figure 4.2.2.4c) a global increase of the vertical stress is observed and, in particular, the peak values are attained in correspondence of the compaction section. The stress amplification gradually reduces towards the boundary of the chamber, maintaining higher values than the geostatic stress.

The normalized mean stress for S045-14, shown in Figure 4.2.2.5 a) and b), has an increase at pile shaft from 7 m < z < L_p, in correspondence of the compaction section. For increasing radial distance from pile axis, p_{INS} reduces, till it approaches the initial values.

Moreover, from z ≈ 3 m to z ~ 6 m there is a strong decompression that spreads towards a distance x ≈ ±2 m. Over this zone p_{INS} gradually increases at the increasing radial distance and reaches the geostatic values at x ≈ ±3 m.

As for S041-4, the mean stress has an amplification along the shaft that diminishes with the increasing distance from pile axis -Figure 4.2.2.5 c) and d)-.

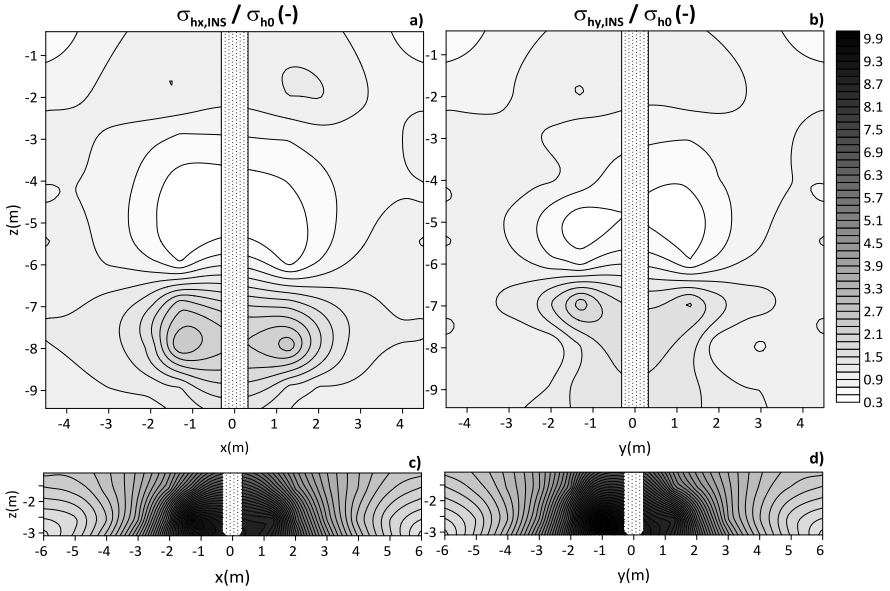

Figure 4.2.2.3. Horizontal stress variation at the end of insertion for S045-14 (a and b) and S041-4 (c and d)

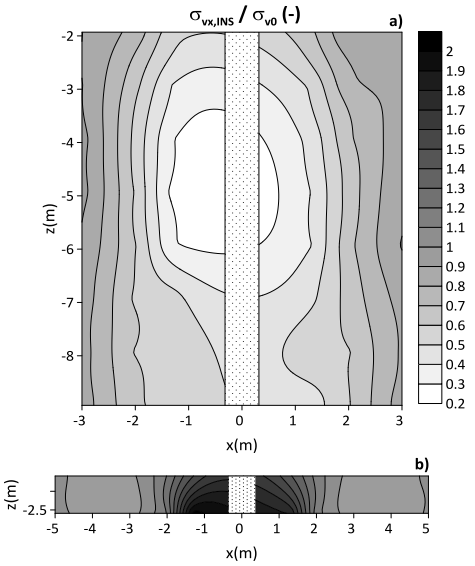

Figure 4.2.2.4. Vertical stress variation at the end of insertion for S045-14(a) and S041-4 (b)

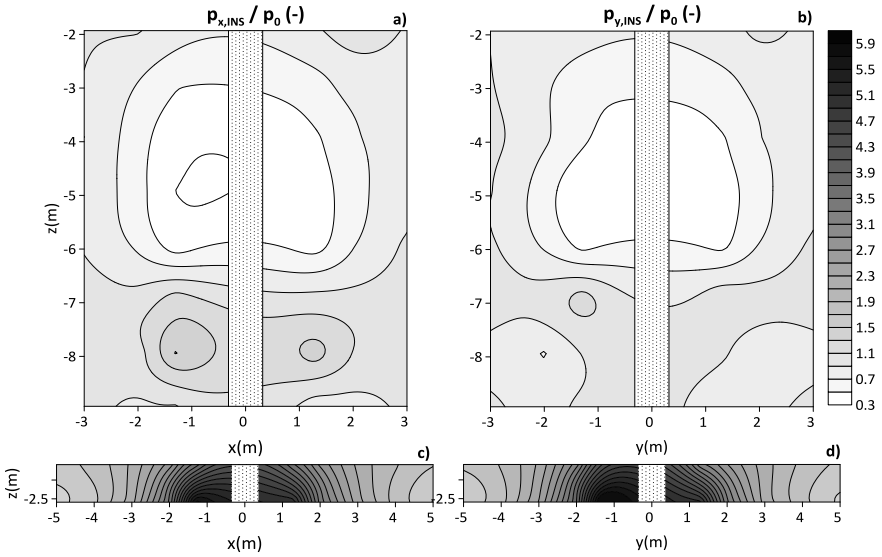

Figure 4.2.2.5. Mean stress variation at the end of insertion for S045-14 (a and b) and S041-4 (c and d)

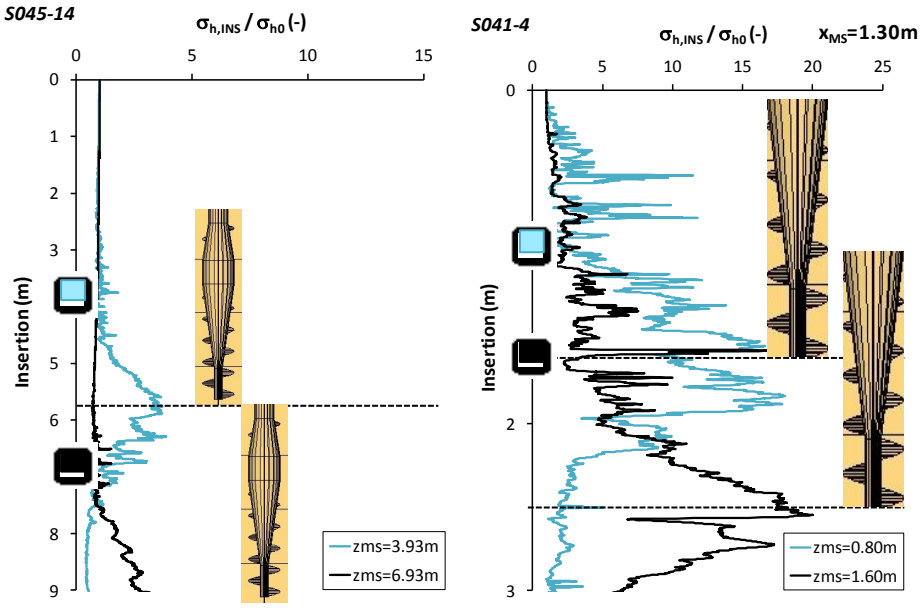

Figure 4.2.2.6. Horizontal stress variation during the insertion at a distance x_{MS} = 1.30 m from pile shaft for S045-14 and S041-4

Figure 4.2.2.6 the horizontal stress measured in the soil at a distance of 1.30 m from the pile shaft for two different levels during the FDP insertion: as it can be seen, there is an evident 'friction fatigue' mechanism, since, as the compaction section passes by the measurement point, the horizontal stress reaches the peak value, which then reduces as the pile penetrates further.

4.2.3. Comments

The insertion of two utensils with different shapes gives rise to different effects, both on pile body and in the surrounding soil.

From the horizontal stress distribution at the jacked and screw pile shaft, shown in Figure 4.2.3.1, it is evident that the two technologies give rise to different mechanisms; in particular, if for a jacked pile there is a compression around the base and at low confining stress, while in the middle there is substantially the geostatic condition, for a screw pile the compression effect is recorded all along the utensil shaft, over which a decompression occurs. Moreover, for both pile types the friction fatigue phenomenon has been verified (Figure 4.2.3.2): they provoke the same peak values of horizontal stress, though the FDP requires a higher level of soil mobilization.

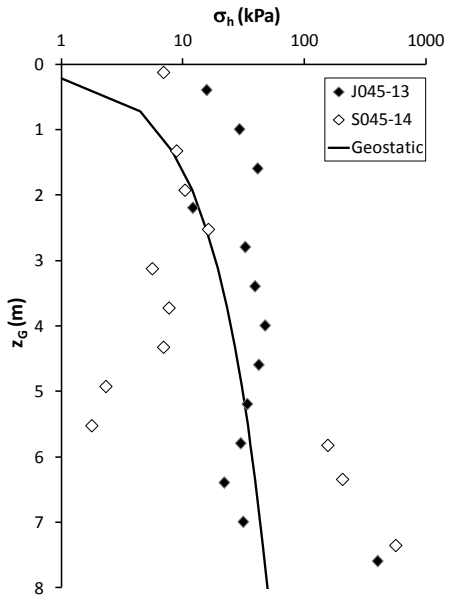

Figure 4.2.3.1. Horizontal stress at the end of insertion for J045-13 and s045-14

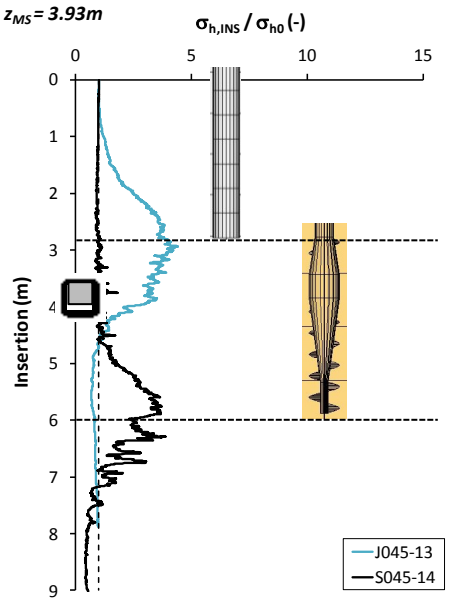

Figure 4.2.3.2. Friction fatigue for J045-13 and S045-14

4.3. End of construction

4.3.1. Jacked piles

At the end of insertion, the stop of jacking corresponds to a reset of forces on pile top. This process gives rise to a tensional relief of the pile, which, as it is loaded again, will exhibit an additional part of resistance due to the residual stress state.

Since this reset phase is considered part of the installation process, it is necessary to be simulated. With this aim, the model pile is lifted up till the sum of base and shaft resistance becomes null. The requested uplifts for pile into loose sand is about 3%d_p, while for the medium dense sand it goes up to 5%d_p. Figure 4.3.1.1a shows the distribution of the normal force N along pile shaft at the end of traction: the residual axial force assumes larger values for the denser case and decreases as the distance from pile base increases.

On the other hand, the variations of the shear stress with h/R for the three cases are reported in Figure 4.3.1.1b, as well. Coherently with the normal force variation, also for the shear stress the highest values are at pile base and

decrease very rapidly with the increasing h/R. In addition, it is possible to notice that from a h/R ≈ $L_p/2$ the ratio τ/τ_{max} is not significantly influenced by porosity.

Eventually, if a lower board of the curve for J041-14 is delineated, in order to not consider the peaks that are substantially due to local effects in the model, it becomes evident that all the data lie in a narrow band, in spite of the different soil initial conditions. All these findings are in a rather good agreement, at least from a qualitative point of view, with the results from traction tests on instrumented piles in centrifuge by Bruno and Randolph (2000).

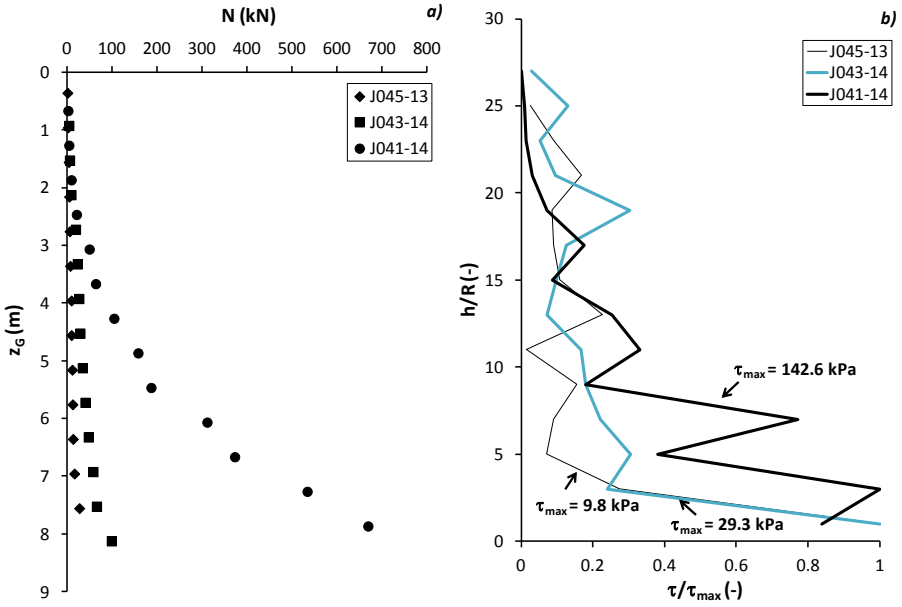

Figure 4.3.1.1. Normal force and shear stress distribution along the pile at the end of the construction

EFFECTS AT PILE SHAFT

The horizontal stress, acting on pile sections at the end of construction, is plotted against z_G for J045-13, J043-14 and J041-14 in Figure 4.3.1.3. The profiles are compared with the horizontal stress calculated by the ICM formulation (by Jardine and Chow 2005, already discussed at §1.2) for a closed-ended jacked pile after the installation. Since the Eq. 1.2.17 requires the profile of the cone penetration resistance q_c, three tests performed at the three

different porosities (reported in §3.4) are considered. The numerical values are in good agreement with the formulation, albeit they have a considerable dispersion (Figure 4.3.1.3), above all the case J041-14, for which the numerical stresses give quite higher values than the empirical formulation for $z_G > 4$ m.

The reasons of this strong scatter principally lie in the local effects occurring in a discrete model; in addition, as aforementioned, the model with n = 0.41 has an initial porosity which decrease with depth, while the operative relative density used into the formulation refers to an average value.

Overall, it is believed that the horizontal stress distribution with depth at the end of construction is in good agreement with the experimental formulation by the *Imperial College*.

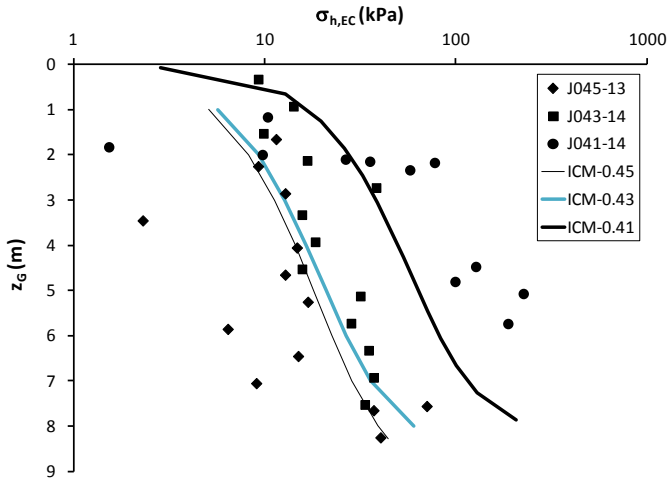

Figure 4.3.1.3. Horizontal stress variation with depth at the end of the construction (EC): comparison with ICM (2005)

EFFECTS IN THE SOIL MASS IN TERMS OF STRESS CHANGES

Figures 4.3.1.4, 4.3.1.5 and 4.3.1.6 show respectively the normalized horizontal $\sigma_{h,EC}$, vertical $\sigma_{v,EC}$ and mean stress p_{EC} distribution at the end of construction for J045-13, J043-14 and J041-14. For the loose models, pile uplift determines a stress relief around pile base and at shallow depths; unlike in the middle the upward displacement induces a slight stress increase, thus reducing the extension of the decompression area (shown at the end of the insertion stage).

As to the medium dense case, a stress reduction (for all $\sigma_{h,EC}$, $\sigma_{v,EC}$ and p_{EC}) occurs at pile base and spreads toward surface, where the stress state is much larger than the geostatic condition, anyway.

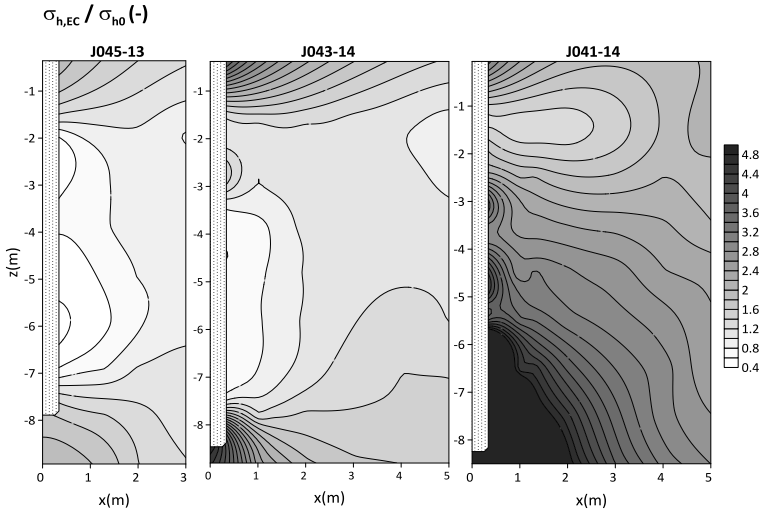

Figure 4.3.1.4. Horizontal stress distribution at the end of construction for J045-13, J043-14 and J041-14

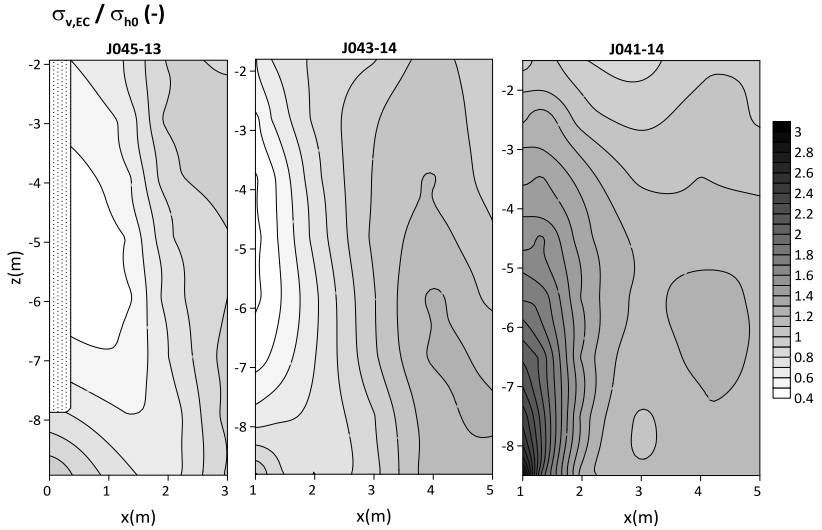

Figure 4.3.1.5. Vertical stress distribution at the end of construction for J045-13, J043-14 and J041-14

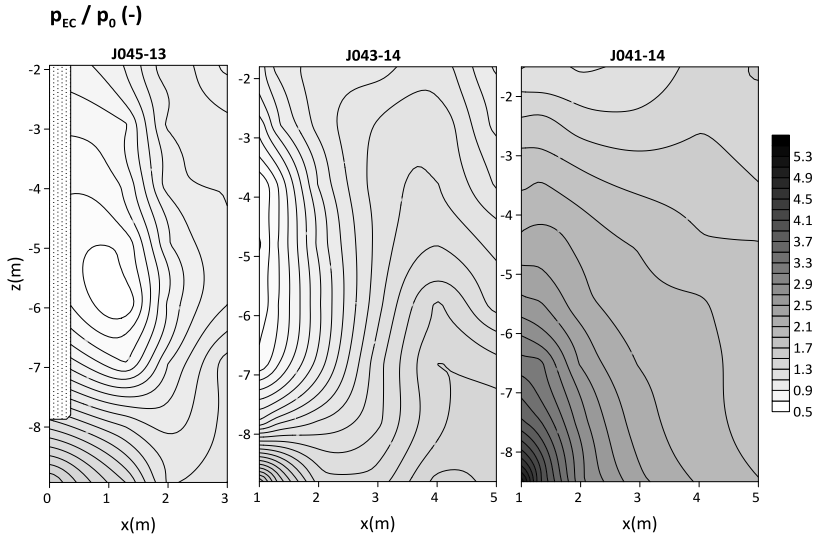

Figure 4.3.1.6. Mean stress distribution at the end of construction for J045-13, J043-14 and J041-14

4.3.2. Full displacement piles

After the insertion, the FDP is extracted by means of a pulling out force and a torque; during this stage the extraction parameters and the effects exerted on the soil state by the extraction are determined, as well.

EXTRACTION ENERGY

The pull out force F_{EX} and the torque T_{EX} during the extraction are plotted against the uplift (normalized to pile length L_p) in Figure 3.6.4. As for the insertion stage, it is also possible to determine the extraction energy as the sum of the contributes by the pull out force, the torque and the pressure exerted by the fluid concrete during the pumping phase (Van Impe, 1994):

$$E_{EX} = \frac{F_{EX} \cdot v_{EX} + \sigma_{conc} \cdot A_f \cdot v_{EX} + T_{EX} \cdot \omega_{EX}}{A_b \cdot v_{EX}} \qquad (4.3.2.1)$$

where A_f is the of the auger flight and σ_{conc} is the concrete pressure. If this latter contribute is neglected, Eq. (4.3.2.1) reduces to Eq. (4.2.2.1) and the extraction energy depends only on the extraction parameters. Figure 4.3.2.1

shows the variation of E_{EX} with the normalized uplift which increases with the decreasing porosity and at the increasing embedment ratio.

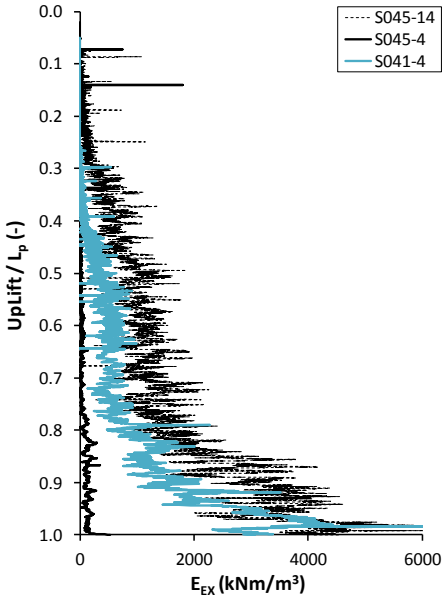

Figure 4.3.2.1. Extraction energy against the normalized uplift

EFFECTS IN THE SOIL MASS IN TERMS OF STRESS CHANGES

Figure 4.3.2.2a and 4.3.2.3 reports the horizontal stress variation calculated in the measurement sphere at the distance x_{MS} = 1.30 m during the extraction for case S045-14, as a function of pile displacement and against time (expressed in numerical step number). It is evident that the extraction process gives rise to a significant stress reduction (σ_h at the end of the stage is almost the half of the geostatic value). As for the medium dense sand (case S041-4), Figures 4.3.2.2b and 4.3.2.4 show that σ_h diminishes and rapidly reaches the geostatic condition.

These numerical results appear to be in contrast with those presented by Van Impe and Peiffer (1997) from DMT measures during the installation of an Omega pile.

Eventually, in Figure 4.3.2.5a-d the mean stress distribution in the whole model at the end of construction (EC) for S045-14 and S041-4 is reported. For the loose model it can be noticed a very strong decompression for x = ± 1 m in

the range $z \approx (L_p/2 \pm 2d_p)$; at the increasing radial and vertical distance from this zone p_{EC}/p_0 gradually increases and tends to geostatic values at $x \approx \pm 3$ m.

As to the medium dense case (S041-4), the mean stress has the geostatic value all along the pile shaft, whilst at the increasing distance x from the pile the stress increase caused by the insertion process appears to be unaltered.

Figures 4.3.2.5, 4.3.2.6 and 4.3.2.7 show the normalized horizontal, vertical and mean stress distribution at the end of construction for S045-14 and S041-4. As aforementioned, the extraction process provokes a global stress reduction all around pile body and, in particular, the strong compression given by the compaction section during the insertion almost gets lost.

Concerning the surrounding soil, from a radial distance $x \approx \pm 3$ m (i.e. $5d_p$) the stress state is not influenced by the tool extraction, for both porosities, with respect to the end on insertion stage.

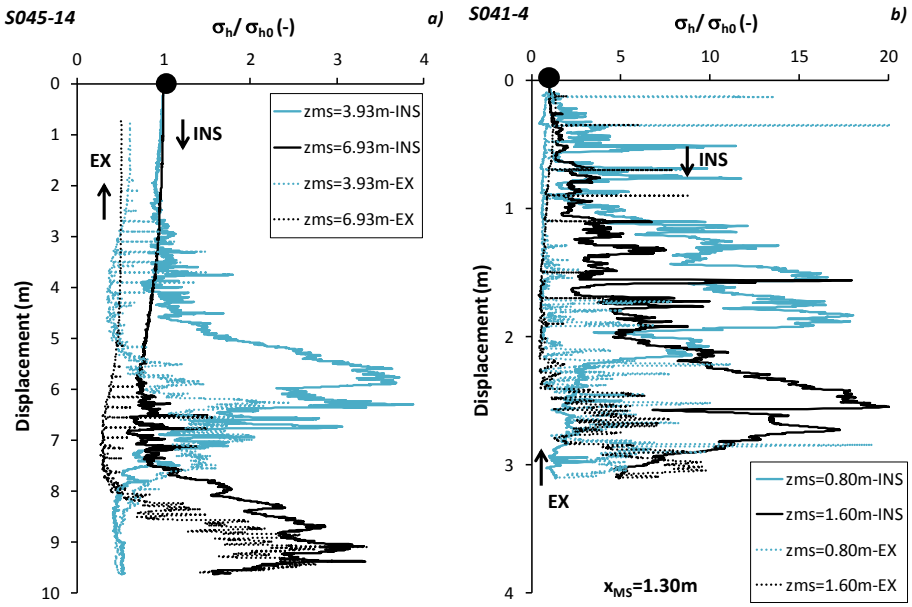

Figure 4.3.2.2. Horizontal stress variation versus pile displacement for the insertion and extraction at a distance x_{MS} = 1.30 m from pile shaft for S045-14 and S041-4

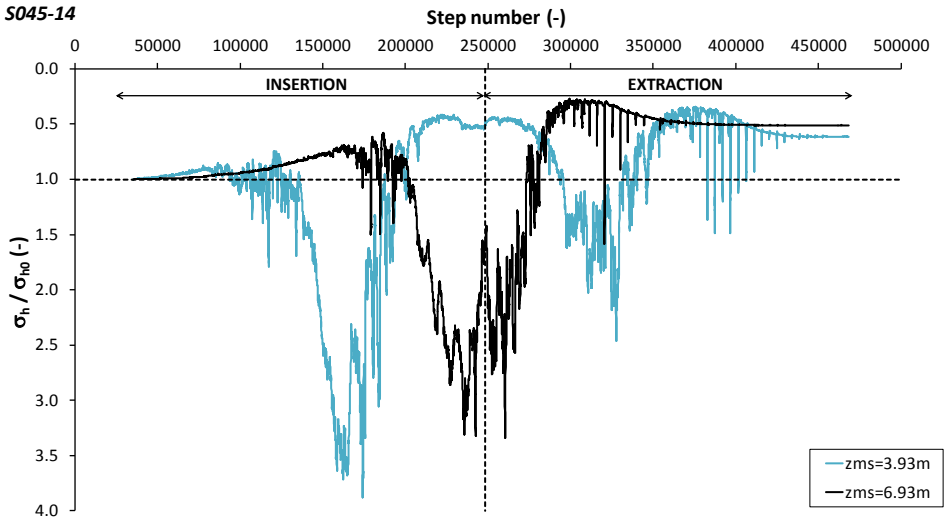

Figure 4.3.2.3. Horizontal stress variation versus step number for insertion and extraction at a distance x_{MS} = 1.30 m from pile shaft for S045-14

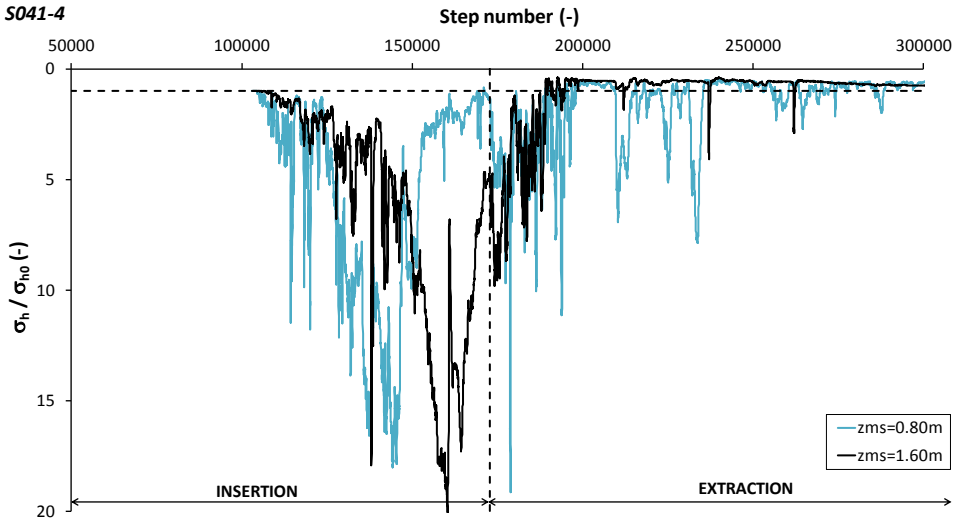

Figure 4.3.2.4. Horizontal stress variation versus step number for insertion and extraction at a distance x_{MS} = 1.30 m from pile shaft for S041-4

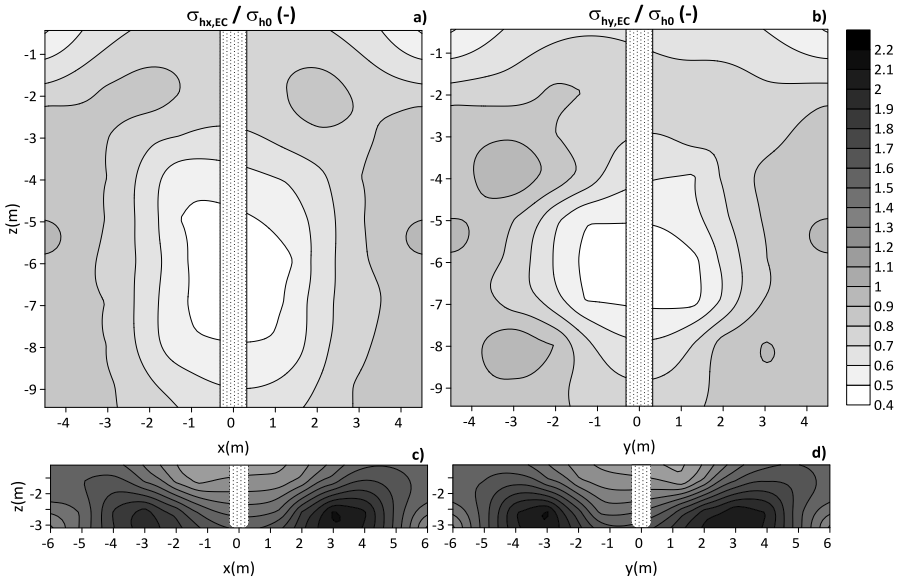

Figure 4.3.2.5. Horizontal stress variation at the end of extraction for S045-13 (a and b) and S041-4 (c and d)

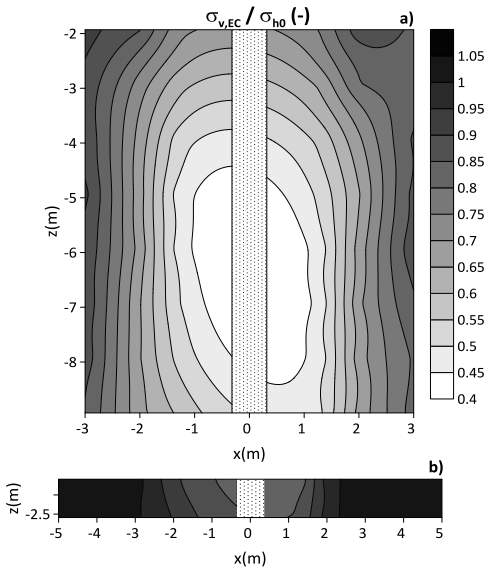

Figure 4.3.2.6. Vertical stress variation at the end of extraction for S045-13 (a and b) and S041-4 (c and d)

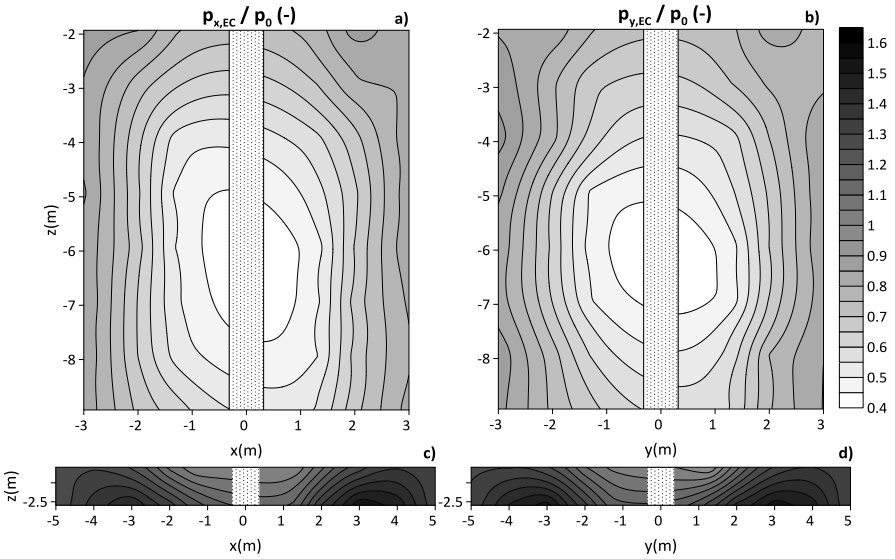

Figure 4.3.2.7. Mean stress variation at the end of extraction for S045-13 (a and b) and S041-4 (c and d)

4.3.3. Comments

For both jacked and screw perforation tools the end of construction reduces the soil stress state. Specifically, the decompression effect provoked by the uplift of the jacked pile is much less significant than that caused by the complete extraction of the screw tool. This is evident from the Figure 4.4.3.1, where the horizontal stress at the end of the construction stage for cases J045-13 and S045-14 (i.e. end of installation) calculated in the measurement regions at the distance x_{MS} = 1.30 m from pile shaft is reported.

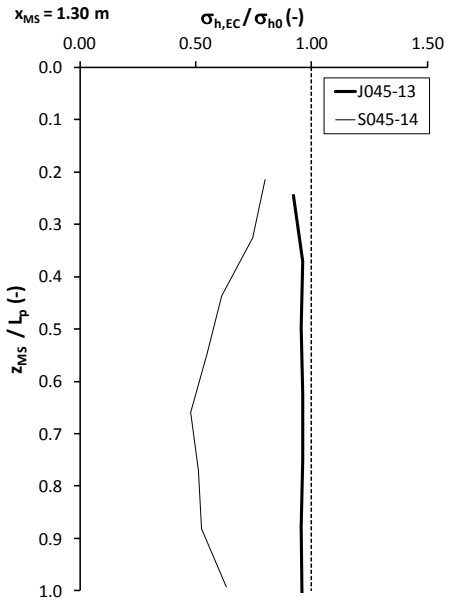

Figure 4.4.3.1. Horizontal stress variation with depth at the end of construction (EC) at a distance x_{MS} = 1.30 m from pile shaft for J045-13 and S045-14

4.4. Loading

4.4.1. Jacked piles

After the installation, all the jacked piles are subjected to an axial load test stopped at a settlement of about the 10% of pile diameter d_p (conventional value for the bearing capacity evaluation).

For this pile type, the 'numerical' load test consists in a further static penetration, carried out by means of an amplification factor for the penetration rate G = 1, in order to do not affect the initial tangent of the load-settlement curve. Figure 4.4.1.1 shows the load-settlement curves (total, base and shaft) for J045-13, J043-14 and J041-14. It is evident that for decreasing porosity the resistances increase: in particular, passing from a very loose soil to a medium dense soil (from n = 0.45 to n = 0.41) the total resistance increases fourfold. The larger contribution to the bearing capacity is from the base; for each case, indeed, it represents the 80% of total resistance.

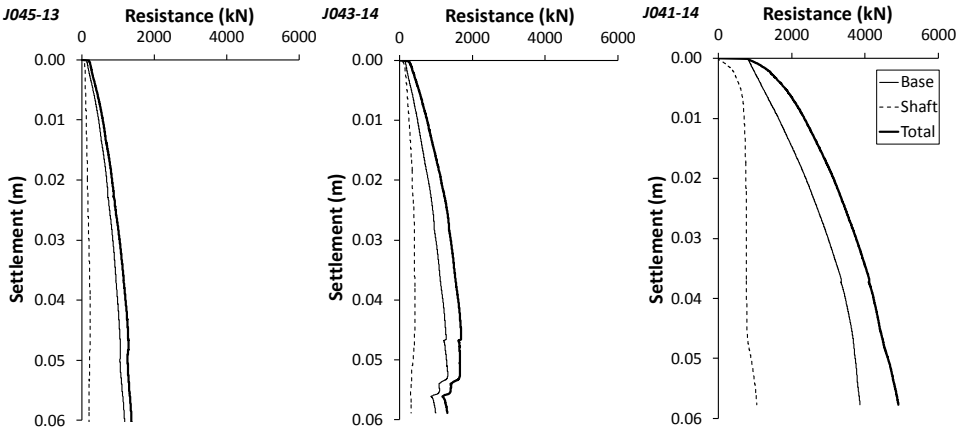

Figure 4.4.1.1. Load-Settlement curves for J045-13, J043-14 and J041-14

Moreover, the base response exhibits a very high initial stiffness, comparable with that at the shaft: this behaviour is principally due to the pre-compression that the installation process generates below pile base (as reported in Figure 4.3.1.4). Although very scarce experimental data are available on this particular aspect, it appears in good agreement with that provided by Viggiani and Vinale (1983) concerning large diameter bored instrumented piles with a preloaded base.

For J045-6 and J041-6 (Figure 4.4.1.2) the aforementioned arguments are even more valid, since they have a lower embedment.

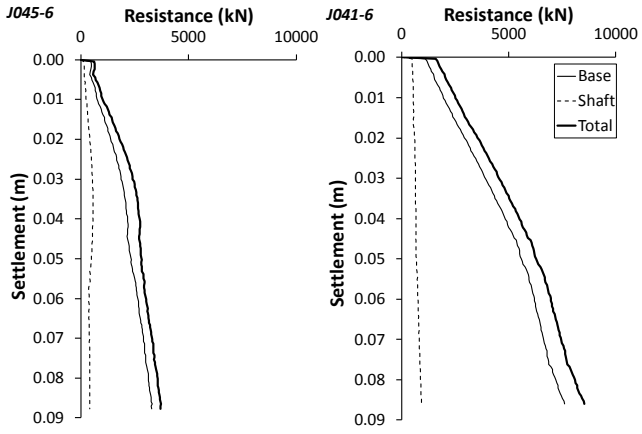

Figure 4.4.1.2. Load-Settlement curves for J045-6 and J041-6

EFFECTS AT PILE BASE

From the load-transfer curves the unit base resistance $q_{b,L}$ corresponding to a settlement equal to 10%d_p, is determined and the end-bearing capacity factor at the end of the loading process $N_{q,L}$ is calculated.

The $N_{q,L}$ values, summarized in Table 4.4.1.1, are lower than $N_{q,INS}$, since they refer to different levels of settlement ($N_{q,INS}$ corresponds to a settlement equal to the whole pile length). Numerical results are compared with the experimental data provided by Chow (1997); these latter hail from in situ loading tests performed on jacked closed-ended piles with slenderness that varies from 18 to 60, into sands with relative density that goes from 25% to 85% (Figure 4.4.1.3). The comparison is limited to only those cases for which D_{Rop} belongs to the experimental range of D_R investigated by Chow.

The $N_{q,L}$ values present the same scattering of the experimental data, albeit they lie on the upper bound. This difference is considered to be due to the much lower embedment ratios of the considered piles which, in addition, present a pre-compression below the base that increases the resistance.

Case	D_{Rop} (-)	$N_{q,INS}$ (-)	$N_{q,L}$ (-)	$q_{b,L}$ (kPa)	$q_{c,av}$ (kPa)	α_c (-)	α_b (-)
J045-6	0.05	64	62	5183	1959	2.5	1.06
J041-6	0.60	200	140	11968	9917	1.3	0.93
J045-13	0.05	55	36	4155	2214	2.5	0.75
J043-14	0.26	70	37	4679	4972	1.6	0.65
J041-14	0.60	131	106	13668	12854	1.3	0.82

Table 4.4.1.1. Summary of base capacity parameters for jacked piles after loading

The unit base resistance $q_{b,L}$ has been normalized to the cone resistance $q_{c,av}$, averaged over a zone of ±1.5d_p, from the CPT profiles for the three considered porosities (see §3.5). Figure 4.4.1.4 shows the comparison of $\alpha_b = q_{b,L}/q_{c,av}$ with the experimental data from Chow (1997).

The Author suggests, as well, a formulation for closed-ended piles where α_b is exclusively depending on the ratio between pile and cone diameters and, in particular, this decreases at the increasing diameters ratio. Unlike the expectations, the influence of the embedment on the numerical α_b values is evident, since it increases at decreasing L_p/d_p.

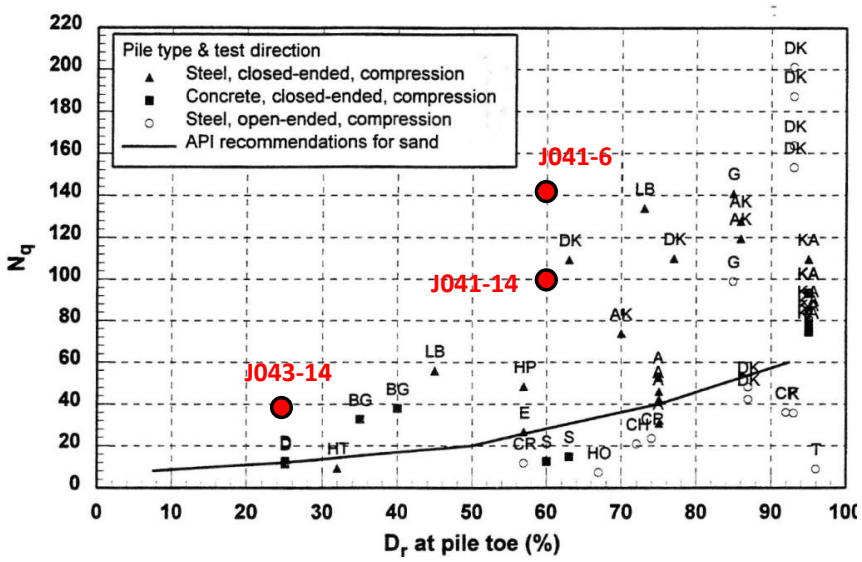

Figure 4.4.1.3. Comparison of numerical $N_{q,L}$ for jacked piles with the experimental data, from Chow (1997)

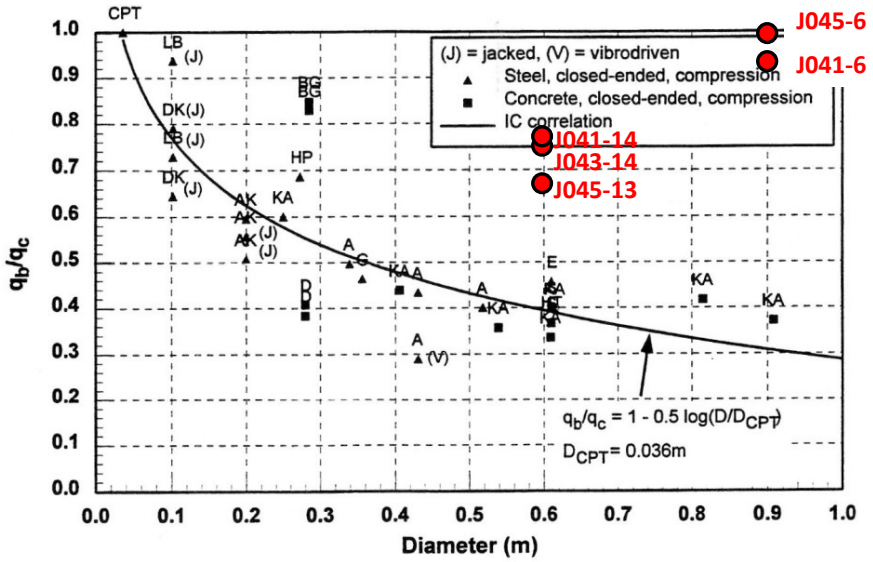

Figure 4.4.1.4. Comparison of numerical α_b for jacked piles with the experimental data, from Chow 1997

Bruno and Randolph (2000) present values of α_b hailing from 56 static pile tests performed in centrifuge at prototype slenderness varying between 3 and 22, for dense and very dense sands. According to their test results, the ratio α_b decreases with the increasing vertical stress acting around pile base (in other words, with pile embedment) and with the increasing relative density. The Authors compare their results with Jardine and Chow (1996), Kraft (1990), de Nicola (1996) and Eslami and Fellenius (1997); in Figure 4.4.1.5 the results from DEM analyses are added to the comparisons among the experimental data.

From this latter check, it is eventually possible to conclude that the numerical α_b are influenced by the embedment ratio, whilst there is not a clear trend with porosity variation.

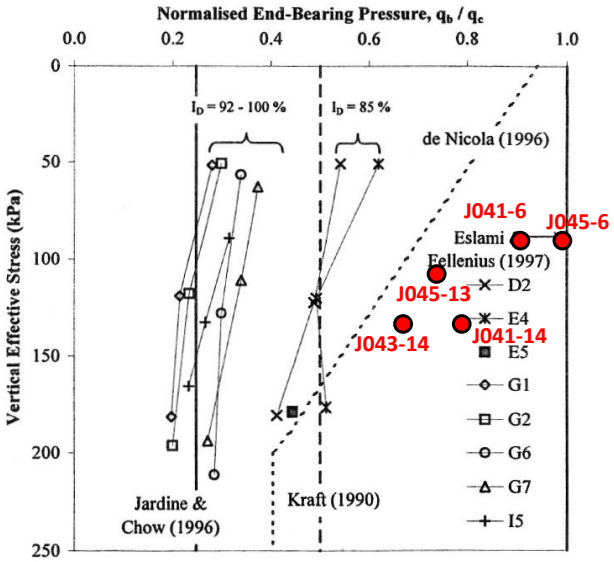

Figure 4.4.1.5. Comparison of numerical α_b for jacked piles with the experimental data, from Bruno and Randolph (2000)

EFFECTS AT PILE SHAFT

Figure 4.4.1.6 shows the horizontal stress variation along pile shaft at the end of the 3 stages: insertion (I), end of construction (EC) and loading (L) for J045-13, J043-14 and J041-14. Only for J045-13 the loading causes a significant stress increase, for the other two cases, indeed, $\sigma_{h,EC}$ and $\sigma_{h,L}$ are rather overlapping. The horizontal stress profile after loading can be normalized to the

initial vertical stress, in order to obtain the earth pressure coefficient variation with depth, K_L. In Figures 4.4.1.7, 4.4.1.8 and 4.4.1.9 the post-loading coefficient along pile shaft for the different cases is reported. K_L is compared with the earth pressure coefficient at rest $k_{0,p}$, calculated for the peak friction angle by Jaky's formulation (1936). Concerning with loose sand, nearby pile top K_L is higher than the earth pressure coefficient at rest $k_{0,p}$ and assumes the peak value. As the confinement stress increases, the increment reduces, since soil volumetric expansion is gradually impeded and, at $z_G \approx 3$ m (about $5d_p$ from surface), it reaches the geostatic condition. For $z_G > 4$ m (about $7d_p$ from surface) the coefficient is even lower than $k_{0,p}$. Eventually, at $z = L_p$, K_L increases, because of the very high stress level below pile base (Figures 4.4.1.7b and 4.4.1.8b).

As for the denser case, J041-14, the entire profile of K_L is affected by the mechanism at pile base, since the pile model has a low embedment ratio. In Figure 4.4.1.9b, indeed, it can be noticed that the stress increment below pile base spreads up towards surface where a larger value of K_L than the geostatic condition is still found.

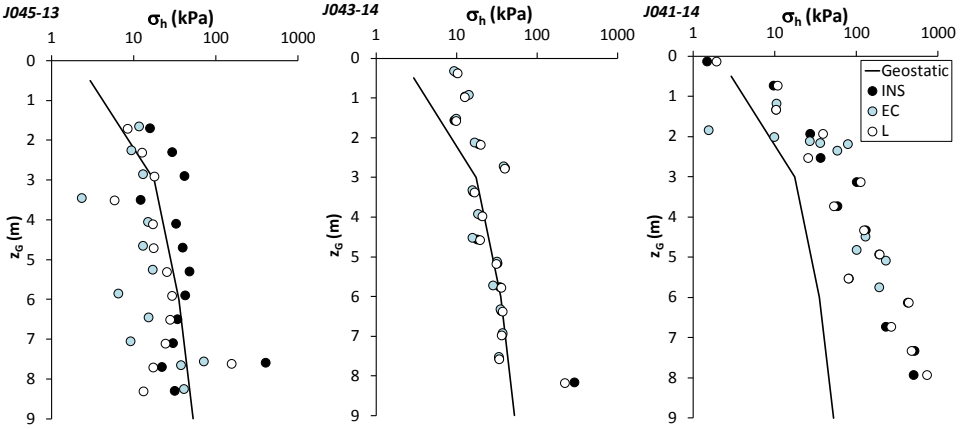

Figure 4.4.1.6. Horizontal stress variation for Insertion (INS), End of Construction (EC) and Loading (L) for different porosities

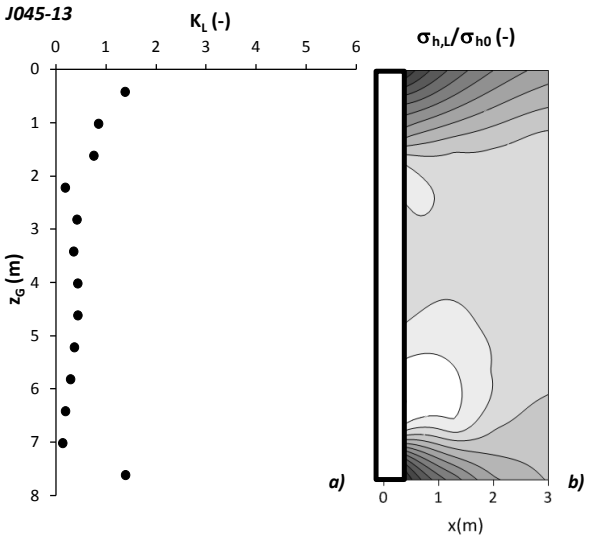

Figure 4.4.1.7. Earth pressure coefficient after loading for J045-13

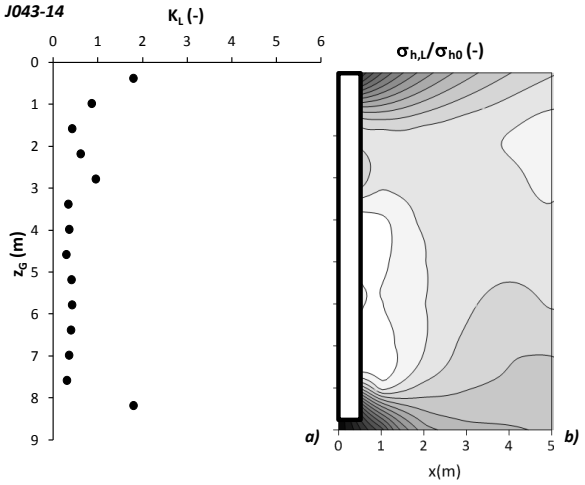

Figure 4.4.1.8. Earth pressure coefficient after loading for J043-14

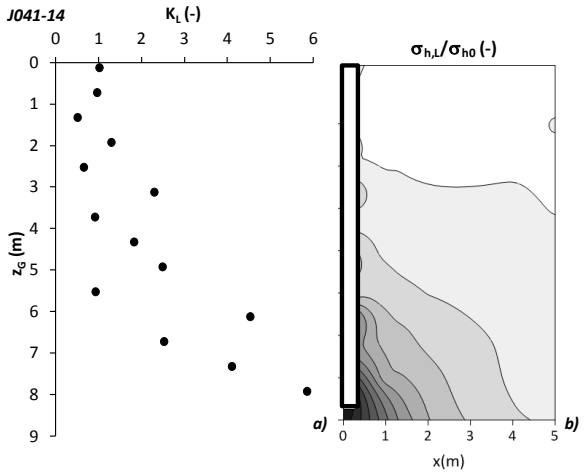

Figure 4.4.1.9. Earth pressure coefficient after loading for J041-14

In order to check the reliability of these values from a qualitative and quantitative point of view, a comparison with the K from the "*Exponential Decay Method*" (by Randolph *et al*. 2003, already discussed in §1.2) for each initial porosity is reported in Figure 4.4.1.10. For J045-13 and J043-14, numerical and theoretical K_L show a quite good matching fro $z_G > 2$ m ($\approx 3d_p$); at low confining stress, indeed, numerical analyses show a significant horizontal stress increment that the theory does not predict. Moreover, at pile base a peak value of K_L is measured, which is out of range with respect to the calculated profile.

For J041-14, unlike the loose sand, K_L indefinitely increases with depth and presents a rather good fit with Randolph et al.'s formulation only for $0 < z_G < 2.5$ m.

Afterwards, the average values of the earth pressure coefficient after loading $K_{L,av}$ along pile shaft for each case and the ratio $K_{L,av}/k_{0,p}$ are summarized in Table 4.4.1.2.

For all the cases $K_{L,av}$ is larger than the initial condition and increases with relative density, consistently with the indications by AGI (1984) and Toolan *et al*. (1990), already discussed at §1.2.

Besides, for J045-6 and J045-13 it is decreasing with pile length, unlikely for J041-6 and J041-14 where it increases with length.

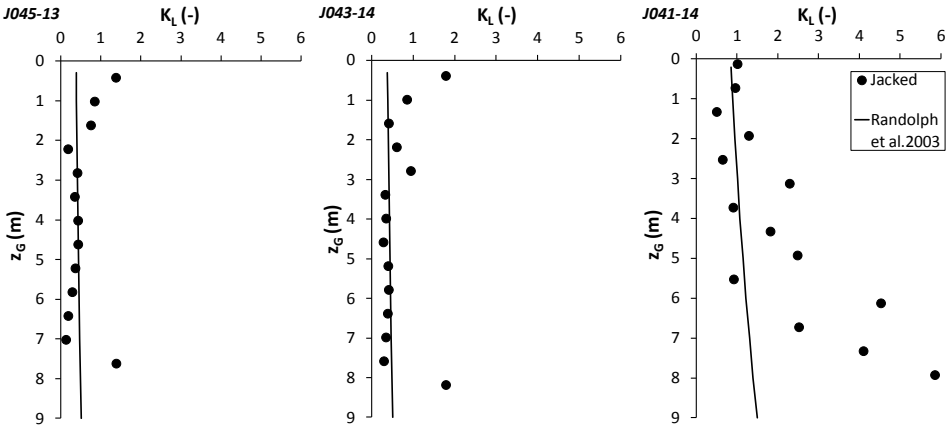

Figure 4.4.1.10. Earth pressure coefficient with depth at the end of loading for J045-13, J043-14 and J041-14

Case	D_{Rop} (-)	$K_{L,av}$ (-)	$K_{L,av}/k_{0,p}$ (-)
J045-6	0.05	1.03	2.3
J041-6	0.60	2.02	6.7
J045-13	0.05	0.43	1.0
J043-14	0.26	0.73	1.8
J041-14	0.60	2.46	8.0

Table 4.4.1.2. Summary of shaft parameters for jacked piles after loading

4.4.2. Full displacement piles

As the extraction is over, the generated pile is subjected to axial loading following the same modality as for jacked piles. In Figure 4.4.2.1 the load transfer curves are reported: for cases S045-4 and S041-4 the base resistance represents the 80% of the end-bearing capacity, whilst for case S045-14 its contributes is about the 70%.

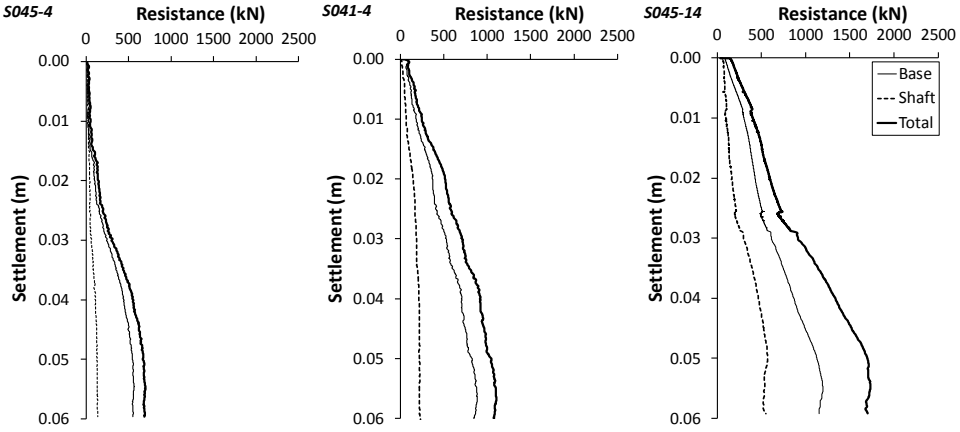

Figure 4.4.2.1. Load-Settlement curves for S045-4, S041-4 and S045-14

EFFECTS AT PILE BASE

In literature there are very few experimental data hailing from loading tests performed on full displacement piles installed into well documented granular soil deposits; therefore, it is not possible to make a direct check of the numerical results reliability for the FDP loading process. For this reason, the bearing capacity factors $N_{q,L}$ and the α_b coefficient (summarized in Table 4.4.2.1) are compared with the experimental data presented by Chow (1997), in order to make a comparison between screw and jacked piles, at least.

In Figure 4.4.2.2 it is shown that $N_{q,L}$ for S041-4 belongs to the experimental dispersion, albeit it has a much lower embedment.

As far as the α_b coefficients concerns, in spite of the observations made for jacked piles in §4.4.1, they maintain a certain rate of dispersion and do not exhibit an evident dependence from the embedment ratio and from relative density (Figure 4.4.2.3).

Case	D_{Rop} (-)	$N_{q,L}$ (-)	$q_{b,L}$ (kPa)	$q_{c,av}$ (kPa)	α_c (-)	α_b (-)
S045-4	0.05	55	1927	1217	2.5	0.63
S041-4	0.60	84	3145	6917	1.3	0.35
S045-14	0.05	32	4085	2312	2.5	0.71

Table 4.4.2.1. Summary of base capacity parameters for FDP after loading

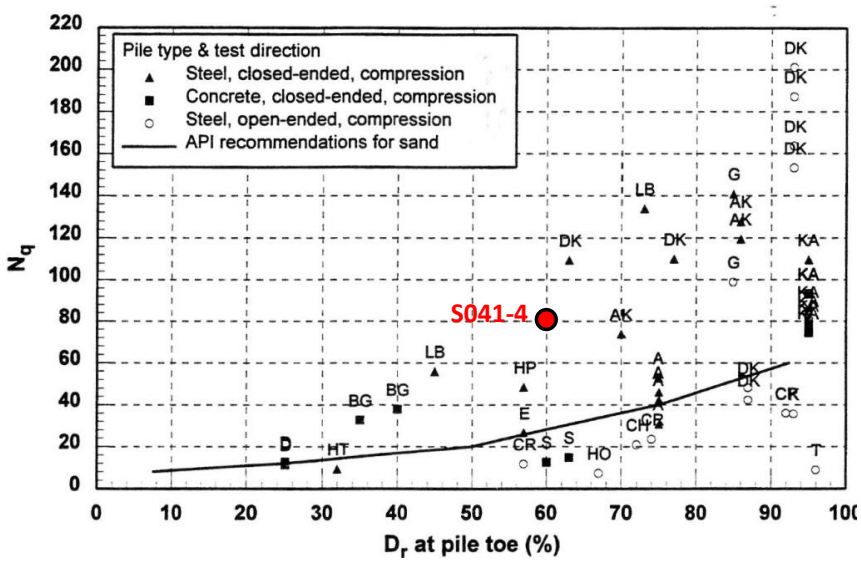

Figure 4.4.2.2. Comparison of numerical $N_{q,L}$ for FDP with the experimental data, from Chow (1997)

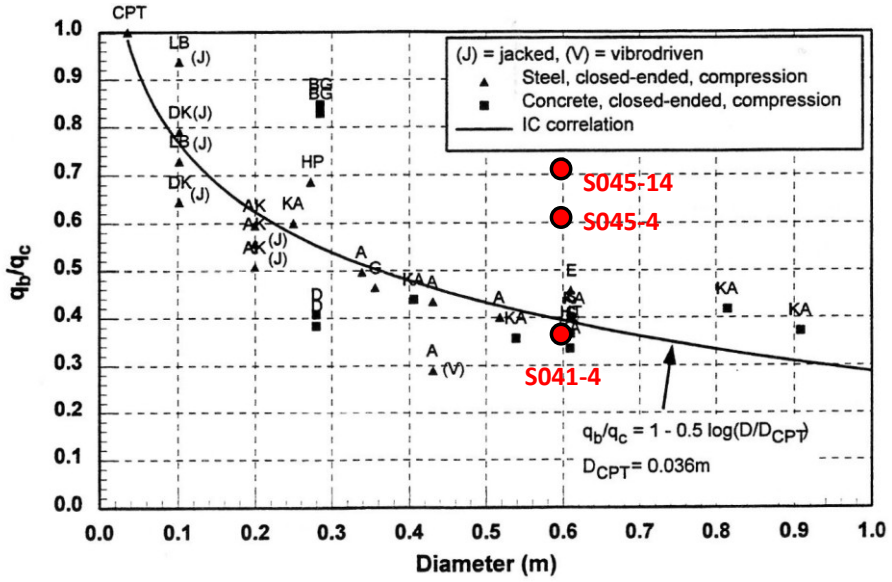

Figure 4.4.2.3. Comparison of numerical α_b for FDP with the experimental data, from Chow (1997)

EFFECTS AT PILE SHAFT

During the extraction stage, the stress state on the sections generated step by step is null. When the pile is then subjected to loading, the only section where the horizontal stress increases significantly is the one adjacent to the base, since the imposed settlement is not large enough to provoke effects that spread up along the whole pile shaft. For this reason, only the average value of the earth pressure coefficient from the shaft resistance value is determined. As it has been already observed for the jacked pile, $K_{L,av}$ values for the FDP (reported in Table 4.4.2.2) are higher than the geostatic coefficient $k_{0,p}$ and have an evident dependence from the relative density and the embedment; in particular, they increase at the increasing relative density and decrease with the increasing confinement level.

Case	D_{Rop} (-)	$K_{L,av}$ (-)	$K_{L,av}/k_{0,p}$ (-)
S045-4	0.05	2.48	5.5
S041-4	0.60	4.00	13.8
S045-14	0.05	0.83	1.9

Table 4.4.2.2. Summary of shaft parameters for FDP after loading

4.4.3. Comments

The loading tests on jacked and screw piles with the same geometry, realized into a very loose sand (J045-13 against S045-14), show that for the screw pile shaft resistance is about the 30% of the bearing capacity, whilst for the jacked the percentage goes down to 20%.

Actually, an even higher difference between the two pile types was expected, since the FDP installation, unlike the jacked pile, has not significantly modified the mean stress below pile base, therefore there is not the pre-compression effect that makes the base response more rigid and larger, as well.

Figures 4.4.3.1 and 4.4.3.2 show the comparison among $N_{q,L}$ and α_b for both jacked piles and FDP with the experimental data. All the numerical results present the same scattering as Chow's database, albeit the FDP exhibits a lower base resistance than the jacked piles.

However, it is recognised that the case studies about FDP are very few, therefore it is not possible to identify any trend, yet.

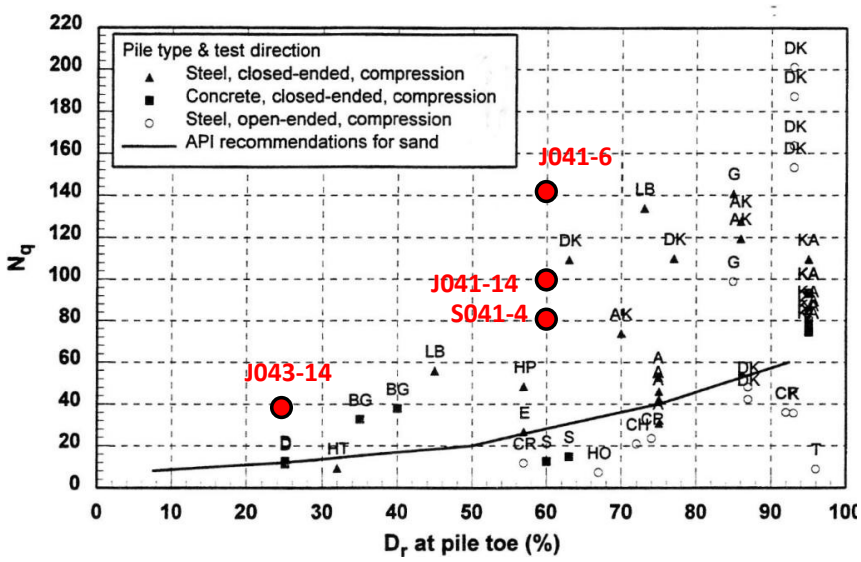

Figure 4.4.3.1. N_q values after loading for jacked piles and FDP, in comparison with the experimental data from Chow (1997)

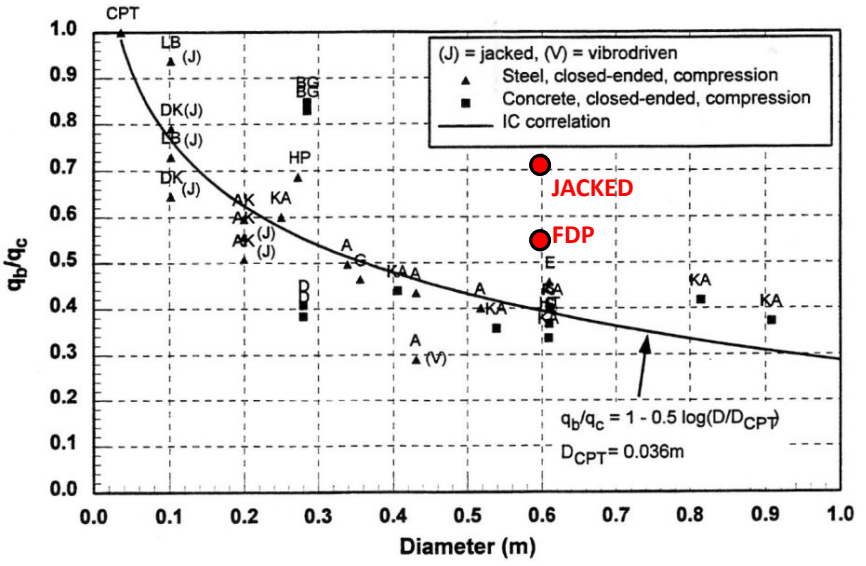

Figure 4.4.3.2. α_b values after loading for jacked piles and FDP, in comparison with the experimental data from Chow (1997)

Concerning the shaft resistance, in Figure 4.4.3.3 all the values of the average earth pressure coefficient, normalized to $k_{0,p}$, for both pile types are reported. As it can be noticed, for loose sands $K_L/k_{0,p}$ decreases at the increasing embedment ratio, in particular, there is no difference between jacked and screw pile. For the medium dense sand, instead, since the lack of numerical results about the FDP model with varying slenderness, it is not possible to make any conclusion.

Eventually, the ratio between the total installation energy and the bearing capacity E/Q_{lim} as a function of the operative relative density for all the cases is determined, in order to compare the different pile types also in terms of cost/benefit ratio.

Since the full displacement pile is installed by the combination of a push force and a torque and the perforation tool has a smooth shape that facilities insertion, its installation should be always more convenient than the jacked piles. Actually, in Figure 4.4.3.4 it is shown that for low operative relative density the full displacement piles are more advantageous, but for increasing D_{Rop} the E/Q_{lim} ratio decreases for jacked piles and increases for FDP. This loss of convenience for the screw piles is given by the fact that the installation process consists of the insertion and extraction stages, therefore the required “cost” energy is the sum of these two contributions.

Nevertheless, at increasing relative density the jacking becomes harder and harder, while the perforation by push and torque for the screw maintains its feasibility.

Definitively, any choice between these two pile types has to take into account these overall considerations.

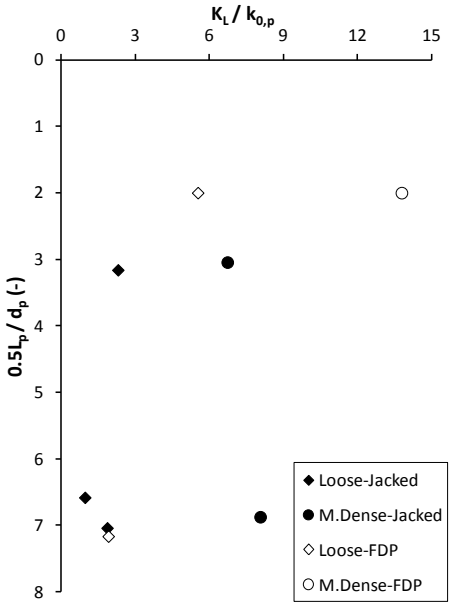

Figure 4.4.3.3. $K_L/k_{0,p}$ values after loading against embedment for jacked piles and FDP

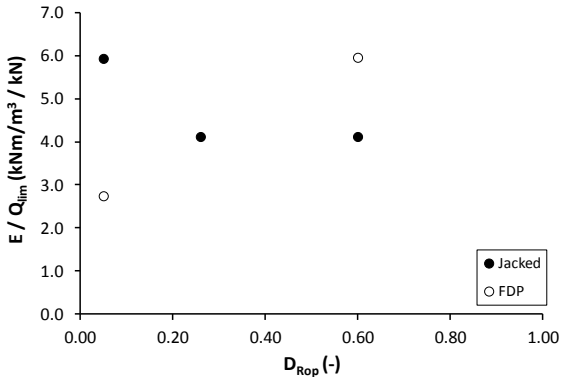

Figure 4.4.3.4. Installation energy on bearing capacity against relative density for jacked and screw piles

CHAPTER 5. CONCLUDING REMARKS AND SUGGESTIONS FOR FUTURE RESEARCH

In the present thesis, the complex problem of the installation and subsequent loading process of displacement piles has been studied using three-dimensional Distinct Element Method (DEM).

Displacement piles have been chosen as object of this work, since they are being increasingly used in the world as foundation elements for structures, in particular, in projects where a fast building construction is required.

Different displacement piles are available in the market, each type being classified according to the specific installation process. They can be divided into two broad categories: jacked tubular closed-end piles, installed under the action of an axial (jacking) load, and screw piles, installed under the combined action of an axial load and a torque. The latter can be further split depending on the particular size and shape of the drilling tools.

In particular, the drilling tool patented by BAUER Maschinen Group was considered, due to a research agreement in force at the present time.

Whatever the pile type, their installation produces a radial displacement of soil greater than the one produced by replacement (bored) piles, particularly in the case of sandy soils, which gain additional stiffness and strength through densification, strictly related to their attitude to suffer volume changes during the pile insertion.

Accordingly, we focused on the effects produced in sandy soils at different initial porosities (or relative densities) by these two pile types (namely, jacked and screw) of different lengths and diameters, trying to highlight the main differences in terms of response to axial loading.

Unfortunately, the computational efforts required for this type of problem are huge, especially for screw piles due to the 3D nature of the problem connected to the shape of the drilling tool. These factors, together with the absence of dedicated loading tests on full scale instrumented piles (initially expected within the research agreement), are the basic cause of the delay in reaching such an ambitious target.

However, a significant step forward has been made if we consider that DEM has been used until now for studying only the insertion of cone

penetrometer, rightly considered as a 'model displacement pile', but with a size completely different (and really smaller) from the full scale pile.

5.1. Concluding remarks

A broad numerical study aimed to checking the reliability of the suggested rules for the analysis of the installation of cone penetrometer in sandy soils has been carried out. On the overall, it could surely be affirmed that the present study confirmed what already known on the subject.

Looking at piles, different rules were found due to the need of calibrating the entire numerical procedure not only to be sure that the pile end-bearing resistance (in the case of CPT, cone resistance) is not affected by the choices for the numerical model, but that such choices do not alter the results in terms of pile shaft resistance (not dealt with in literature).

Table 5.1 summarizes the selected numerical parameters selected as reasonable compromise among computational efforts and precision of the solution.

Soil State	D_{MS}/d_{av}^{*} (-)	R_d (-)	n_p (-)	n_H (-)	α_c (-)	G (-)	Model Type
Very loose	20	15	6	2	2.5	10	Complete - Half
Loose-Med.Dense	20	20	6	2	1.3-1.6	10	Complete - Half

Table 5.1. Summary of the numerical parameters for the installation process

The insertion of a tool in sandy soil determines dramatic changes in the soil state: horizontal and vertical stresses, as well as initial porosity (or relative density), are deeply altered with respect to their initial values.

Looking at soil stresses (of major interests for axial pile resistance evaluation), different scenarios have been detected.

For jacked piles in loose sand, three different 'stress zones' occur close to the pile: close to the pile base and to pile head, a significant increase of the stresses (compression) has been revealed; such an increase tends to vanish moving toward the central part of the pile, sometimes resulting in values lower than the initial (geostatic) stresses. What has just been affirmed is not true if jacked piles are installed in dense sand for which a general increase of the state of stress is observed.

The insertion of screw (FDP) piles in loose sand concentrates, as expected, the increase of the stress (compression) only in correspondence of

the compaction section of the drilling tool. For all the remaining parts, a reduction (decompression) of the stress has been revealed.

At the end of pile construction (load removal at pile head for the jacked pile; extraction of the drilling tool with the contextual pile elements generation for the screw piles), horizontal stresses always reduce, in some cases (loose sand) even nullifying the positive effects produced during the insertion.

The derived design parameters for jacked piles, in terms of end-bearing capacity factor N_q, are in rather good agreement with both theoretical and experimental data. The same applies to the increase of the earth pressure coefficient K with respect to the initial values a rest $k_{0,p}$, at least from a qualitative point of view.

The lack of detailed experimental data for screw (FDP) piles makes impossible to draw similar conclusions. Nevertheless, the comparison with some collected experimental data by other researchers seems to be encouraging.

The two pile types have been also compared in terms of cost/benefit analysis, represented by the ratio between the required installation energy of a given pile and the corresponding axial capacity. It has been derived that screw piles are certainly advantageous in loose sandy soil; for denser soil, the reverse is true, although it has to be considered that screw piles are more simply inserted due to the combined action of thrust and torque.

5.2. Suggestions for future research

Accordingly to what affirmed before, it is quite clear that any efforts should be made to overtake computational limits due to the intrinsic nature of DEM. In this view, it is believed that numerical approaches based on coupling DEM and FDM (Finite Difference Method) should be really promising.

Of particular relevance is the possibility to numerically explore the effects played by different screws: there is no need to say that different shape and size of the perforation tool will certainly determine different effects on the surrounding soil, thus on the subsequent pile response to axial loading. The availability of well-established numerical procedure to deeply investigate these aspects could be of great help for piling companies, often searching for a solution without any rational approach but simply driven by intuition (thus not repeatable) or, even worst, by blind attempts.

As typical in Geotechnical Engineering, the development of a database containing in situ test results (performed before and after pile installation) and

pile load test results can greatly help the prediction capability and the consistency of possible design methods, taking into account different insertion tools (especially for screw piles). The load tests should be carried out at pile head settlements not lesser than 10% of the pile diameter; the piles should preferably be instrumented (at the minimum, base and shaft resistances should be evaluated separately) and the test site should be well characterized.

Results from pile installation and loading modelling, as here discussed, in conjunction with well designed full scale load tests and systematic monitoring of pile installation, will lead to meaningful advances in the design and practice of displacement piles.

REFERENCES

American Petroleum Institute RP-2A. *Recommended Practice for Planning, Designing and Constructing Fixed Offshore Platforms*, Washington, DC, 1993.

Associazione Geotecnica Italiana. *Raccomandazioni sui pali di fondazione*. Roma, 1984.

Arroyo M., Butlanska J., Gens A., Calvetti F., Jamiolkowski M. Cone penetration test in a virtual calibration chamber. *Géotechnique,* Vol.61 No.6, 525-531, 2011.

Baldi G. et al. Laboratory validation of in-situ tests. *AGI Golden Jubilee Volume for XI ICSMFE*, San Francisco, 217-239, 1985.

Baldi G., Belloti R., Jamiolkowski V. M. and Lo Presti M. Modulus of sands from CPT's and DMT's. In 12th *ICSMEF*, Rio de Janeiro, 165-170, 1989.

Basu P., Loukidis D., Prezzi M. and Salgado R. Analysis of Shaft Resistance of Jacked Piles in Sands, *International Journal for Numerical and Analytical Methods in Geomechanics*, Vol.35 No.15, 1605-1635, 2011.

Beretzantzev V. G., Kristoforov V. and Golubkov V. Load bearing capacity and deformation of pile foundations. *Proceedings of the Fifth International Conference of Soil Mechanics and Foundation Engineering,* Paris, Vol.2*,* 11-15, 1961.

Bolton M. D. The strength and dilatancy of sands. *Géotechinique*, Vol.36 No.1, 65-78, 1986.

Bond A. J, Jardine R. J. Effects of installing displacement piles in a high OCR clay, Géotechnique, Vol.41 No.3, 341–63, 1991.

Bottiau M., Meyus I. and Callens S. Screw-in energy measurement for on-site control of the bearing capacity of Omega piles. *Proceedings Of 7th International Conference on Piling and Deep Foundations*, Vienna, Balkema, 1998.

Boulon M. and Foray P. Physical and numerical simulation of lateral shaft friction along offshore piles ins sand. In *3rd International Conference on Numerical Methods in offshore Piling*, *IFP-LCPC* Nantes*,* 127-146, 1986.

Briaud J. L. and Tucker L. Piles in sand: a method including residual stress. *Journal of Geotechnical Engineering*, Vol.110 No.11, 1666-1680, 1984.

Bruno D. and Randolph M. F. Centrifuge modelling of driven piles in dense sand. *Research report No. G:1471*, The University of western Australia, Department of Civil and Resource engineering, Geomechanics Group, 2000.

Bustamante M. and Gianeselli L. Pile bearing capacity predictions by means of static penetrometer CPT. *Proceedings of the 2nd European Symposium on Penetration Testing, ESOPT II, Vol. 2,* Balkema*,* Rotterdam, 493-500, 1982.

Butlanska J., Arroyo M., Gens A. A Virtual Calibration Chamber CPT on Ticino Sand. *2nd International Symposium on Cone Penetration Testing,* Huntington Beach, CA, 217-224, 2010.

Calvetti F. Limitations and perspectives of the Micromechanical Modelling of Granular Materials. *Mathematical and Computer Modelling*, Vol.37, 485-495, 2003.

Calvetti F., Viggiani G., Tamagnini C. A numerical investigation of the incremental behaviour of granular soils. *Rivista Italiana di Geotecnica*, *Special Issue on Mechanics and Physics of Granular Materials,* Vol.37 No.3, 5-23, 2003.

Calvetti F. Discrete modeling of granular materials and geotechnical problems. *Eur. J. Env. Civ. Engng 12*, No.7-8, 951-965, 2008.

Carter J. P., Booker J. R. and Yeung S. K. Cavity expansion in cohesive-frictional soils. *Géotechnique*, Vol.36, 349-353, 1986.

Chow F. C. *Investigations into displacement pile behaviour for offshore foundations*. PhD thesis, Imperial college, London, 1997.

Collins I. F., Pender M. J. and Wang Yan. Cavity expansion in sands under drained loading conditions. *Int. J. Numer. Analy. Meth. Geomech*, Vol.16 No.1, 3-23, 1992.

Colombi A. *Physical modelling of an isolated pile in coarse grained soils*. PhD thesis, Università di Ferrara, 2005.

Cundall P. A. and Strack O. D. L. Discrete numerical model for granular assemblies. *Géotechnique*, Vol.29 No.1, 47-65, 1979.

Cundall P. A. Distinct element models of rock and soil structure. In E. Brown (ed), *Analytical and Computational Methods in Engineering Rock Mechanics*, 1987.

Darrag AA, Lovell CW. A simplified procedure for predicting residual stresses for piles. *Proceedings of the 12th International Conference on Soil Mechanics and Foundation Engineering*, Rio de Janeiro, Brazil, Vol. 2, 1127–1130, 1989.

De Cock F. and Imbo R. Atlas screw pile: A vibration-free, full displacement, cast in place pile: Design and construction of Auger cast piles. *Transportation research record*, No. 1447, 49-62, 1994.

de Nicola A. *The performance of pipe piles in sand*. PhD thesis, University of Western Australia, Nedlands 6907, Australia, 1996.

Dijkstra J. *On the Modelling of Pile Installation*. PhD thesis, Technische Universiteit Delft, Delft, 2009.

Eslami A. and Fellenius B. H. Pile capacity by direct cpt and cptu methods applied to 102 cases histories. *Canadian Geotechnical Journal*, Vol.34 No.6, 886-904, 1997.

Falagush O., McDowell G. and Yu H.-S. Discrete element modelling of cone penetration tests in granular materials. *Geotechnical and Geophysical Site Characterization 4* – Coutinho & Maine (eds), Taylor and Francis Group, London 2013.

FHWA. Drilled Shafts: Construction Procedures and LRFD Design Methods. *U. S. Department of Transportation Federal Highway Administration*, NHI Course N. 132014

Fioravante V. On the shaft friction modelling of non-displacement piles in sand. *Soils and Foundations*, Vol.42 No.2, 23-33, 2002.

Fleming W. G. K., Weltman A. J., Randolph M. F. and Elson W. K. *Piling Engineering*. Taylor and Francis, 1992.

Gavin K. G and O'Kelly B. C. Effect of friction fatigue on pile capacity in dense sand. *Journal of Geotechnical and Geoenvironmental Engineering*, *ASCE*, Vol.133 No.1, 63-71, 2007.

Gibson R. E. Correspondence. *J. Inst. Civ. Engrs*, Vol. 34, 382-383, 1950.

Houlsby G. T. and Hitchman R. Calibration chamber tests of a cone penetration in tests. *Géotechnique*, Vol. 38 No.1, 39-44, 1988.

Itasca. *PFC2D 3.10 Particle Flow Code in Two Dimensions, Theory and Background volume* (Third ed.). Minneapolis, Minnesota, 2004.

Itasca. *PFC3D Particle flow code in three dimensions V3, User's guide*. Minneapolis: Itasca Consulting Group, 2005.

Jaky J. Stability of earth slopes. *Proceedings of the First International Conference on Soil Mechanics and Foundation Engineering Vol. 2,* Cambridge, MA, 125-129, 1936.

Jamiolkowski M., Lancellotta R., Lo Presti D.C.F., Pallara O. Stiffness of Toyoura sand at small and intermediate strain. *Proceedings. XIII ICSMFE*, New Delhi, India*,* 1994.

Jamiolkowski M., Lo Presti D. C. F., Manassero M. Evaluation of relative density and shear strength of sands from CPT and DMT. *Soil behaviour and soft ground construction, ASCE Geotechnical Special Publication* 119, 201-238, 2003.

Jardine R. J., Lehane B. M. and Evereston S. J. Friction coefficients for piles in sands and slits. In *Offshore site investigation and Foundation behaviour*, *Soc. For Underwater Technology*, Vol.28, 661-677, 1992.

Jardine R. J and Chow F. C. New design methods for offshore piles. *Marine Tech. Directorate*, London, *MTD96/103,* 1996.

Jardine R. J., Chow F. C., Overy R. and Standing J. *ICP design methods for driven piles in sands and clays*. Thomas Telford Ltd, 2005.

Jiang M. J., Yu H.-S. and D. Harris. Discrete element modeling of deep penetration in granular soils. *Int. Journ. Anal. Methods in Geomechanics*, Vol.30 No.4, 335-361, 2006.

Kishida H. Ultimate bearing capacity of piles driven into loose sand. *Soils and Foundation*s, Vol.7 No.3, 20-29, 1967.

Kraft L. M. Computing axial capacity in sands for offshore conditions. *Marine technology*, Vol.9, 61-92, 1990.

Kraft L. M. Performance of axially loaded pipe pile in sand. *Journal of Geotechnical Engineering*, Vol.117 No.2, 272-296, 1991.

Kulhawy F.H. Limiting tip and side resistance: Fact or fallacy, in *Proceedings of Symp. On Analysis and Design of Pile Foundations*, *ASCE* Spec. Conf., San Francisco, 80–98, 1984.

Lehane B. M. *Experimental investigations of pile behaviour using instrumented field piles*. PhD thesis, Imperial College, London, 1992.

Lehane B. M., Jardine R. J., Bond A. J. and Frank R. Mechanisms of shaft friction in sand from instrumented pile tests. *Journal of Geotechnical Engineering*, *ASCE,* Vol. 119 No. GT1, 19-35, 1993.

Lehane B. M. and Jardine R. J. Shaft capacity of driven piles in sand: A new design approach. In *7th International Conference on the behaviour of offshore structures*, 21-36, 1994.

Lehane B. M. and White D. J. Lateral stress changes and shaft friction for model displacement piles in sand. *Canadian Geotechnical Journal*, 42: 1015-1029, 2005.

Lo Presti D. *Mechanical behaviour of Ticino sand from resonant column tests*. PhD thesis, Politecnico di Torino, 1987.

Mandolini A., Russo G. and Viggiani C. Pile foundations: experimental investigations, analysis and design: state of the art report. *Proceedings of the 16th International Conference on Soil Management and Geotechnical Engineering*, Vol.1, Osaka, 2005.

Meyerhof G. G. The ultimate bearing capacity of foundations. *Géotechnique*, Vol.2 No.4, 301-332, 1951.

Meyerhof G. G. Bearing capacity and settlement of pile foundations. *ASCE Journal of Geotechnical Engineering*, Vol.102 No.GT3, 197-228, 1976.

Neely W. J. Bearing capacity of augercast piles in sand. *Journal of Geotechnical Engineering*, *ASCE*, Vol.117 No.2, 331-345.

O'Sullivan C. *Particulate discrete element modelling. A Geomechanics Perspective*. Spon Press, 2011.

Peterson R. W. Penetration resistance of fine cohesionless soils. *Calibration Chamber Testing*, *Elsevior Science Publishing Company – A. B. Huang Editor* - 315-328, 1991.

Poulos H. G. and Davis E. H. Pile foundation analyses and design. John Wiley and Sons, New York, 1980.

Poulos H. G. Pile behaviour – theory and application. *29th Rankine Lecture of the British Geotechnical Society*, *Géotechnique*, Vol. 39 No.3, 365-415, 1989.

Poulos H. G., Carter J. P. and Small J. C. Foundations and retaining structures: research and practice. *Proceedings of the Fifteenth International Conference on Soil Mechanics and Geotechnical Engineering*, Vol.4, Istanbul, 2527-2606, 2001.

Pucker T. and Grabe J. Numerical simulation of the installation process of full displacement piles. *Computer and Geotechnics*, 45, 93-406, 2012.

Randolph M. F. and Murphy B. S. Shaft capacity of driven piles in clay. *OTC Report 4883. Proceedings of the 17th Annual Offshores Technology Conference*, Vol.1, Houston, TX, 371-378, 1985.

Randolph M. F. Science and empiricism in pile foundations design. *Géotechnique*, Vol.53 No.10, 847-875, 2003.

Randolph M. F., Dolwin J. and Beck R. Design of driven piles in sand. *Géotechnique*, Vol.44 No.3, 427-448, 1994.

Rowe P. W. The stress-dilatancy relation for static equilibrium of an assembly of particles in contact. *Proc. R. Soc. London*, *Ser. A*, *A269*, 500-527, 1962.

Royis P. and Doanh T. Theoretical analysis of strain response envelopes using incrementally non-linear constitutive equations. *Int. Journ. Anal. Methods in Geomechanics*, 22, 97-132, 1998.

Salgado R., Mitchell J. K. and Jamiolkowski M. Cavity expansion and penetration resistance in sand. *J. Geotech. Geoenviron. Eng.*, Vol.123 No.4, 344-354, 1997.

Salgado R. and Prezzi M. Cavity expansion pressure and penetration resistance in sand. *International Journal of Geomechanics*, *ASCE*, Vol. 7, 251-265, 2007.

Schmitt A. and Katzenbach R. Bored and screwed pile, continuum and discontinuum approaches. *Numerical Modelling of Construction Processes in*

Geotechnical Engineering for Urban Environment, Taylor and Francis Group, London, 2006.

Sheng D., Wreggers P. and Sloan S. W. Improved numerical algorithms for frictional contact in pile penetration analysis. *Computers and Geotechnics*, Vol.33, 341-354, 2006.

Tomlison M. J. PILE DESIGN and CONSTRUCTION PRACTICE. 4th edition, E & FN SPON An Imprint of Chapman & Hall, 2004.

Toolan F. E., Lings M. L. and Mirza U. A. An appraisal of API RP2A recommendations for determining skin friction of piles in sand. In *Proceedings of 22th Offshore Technology Conference, Houston, Texas*, Vol. OTC 6422 No.4, 33-42, 1990.

Uesugi M. and Kishida H. Frictional resistance at yield between dry sand and mild steel. *Soils and Foundations*, Vol.26 No.4, 139-149, 1986.

Van Impe W. F. Influence of screw pile installation parameters on the overall pile behaviour. *Workshop "Piled Foundations: Full Scale Investigations, Analysis and Design"*, *Napels*, 1994.

Van Impe W. F and Peiffer H. Influence of screw pile installation on the stress state in the soil. *Design of Axially Loaded Piles – European Practice*, D. C. Legrand, Rotterdam, Balkema, 3-19, 1997.

Vesic A. S. Tests on instrumented piles, Ogeechee River site. *J. Soil Mech. Fdn. Endng Div. Am. Soc. Civ. Engrs*, Vol. 96 No.SM2, 561-584, 1970.

Vesic A. S. Expansion of cavities in infinite soil mass. *Journal of the Soil Mechanics and Foundations Division*, *ASCE*, Vol. 98, No. SM3, 265-290, 1972.

Viggiani C., Mandolini A. and Russo G. *Piles and Pile Foundations*. Spon Press, 2012.

Viggiani C. and Vinale F. Comportamento di pali di pali trivellati di grande diametro in terreni piroclastici. *Rivista Italiana di Geotecnica*, Vol.23 No.2, 59-84, 1983.

White D. J. and Bolton M. D. Observing friction fatigue on a jacked pile, in S.M. *Centrifuge and Constitutive Modelling: Two extremes, Rotterdam: Zwets and Zeitlinger*, Springman (ed), 347–354, 2002.

White D. J. and Lehane B. M. Friction fatigue on displacement piles in sand. *Géotechnique*, Vol.54 No.10, 645-658, 2004.

Yu H. S. and Houlsby G. T. Finite cavity expansion in dilatants soils: Loading analysis. *Géotechnique*, Vol.41 No.2, 173-183, 1991.

Zhou J., Jian Q., Zhang J., Guo J. Coupled 3D discrete-continuum numerical modeling of pile penetration in sand. *Journal of Zhejiang University – SCIENCE A*, Vol.13 No.1, 44-55, 2012.

Zhu H., Zhou Z., Tang R. and Yu A. Discrete particle simulation of particle systems: Theoretical developments. *Chemical Engineering Science*, Vol.62 No.23, 5728-5770, 2007.

ACKNOWLEDGEMENTS

I sincerely would like to give thanks to professor Alessandro Mandolini, who gave me the chance to live such an important and uplifting life experience. I thank him for having always believed in me, exalted me in times of weakness and dampened me in those of excessive fervour. Through his passion and determination he increased, day by day, the love for my work.

I thank professor Francesco Calvetti, who taught me the "art" of modelling and helped me to face with calm and serenity the gruelling adventure in Lecco.

The research presented in this Thesis has been developed also with the contribution of BAUER-ITALIA s.r.l. and ICOTEKNE S.p.a.; their support is gratefully acknowledged.

With great affection I'd like to give thanks to my friends/colleagues/roommates of the "legendary room 11": Antonella, Raffaele, Luca, Beniamino, Pietro, Ylenia, who, in the brief and intense years gone by, shared with me long days of work, laughters and blues.

A special thank goes to Ylenia, who helped me over time with tenderness and obstinacy in the moments of trouble I went through.

I thank Marilisa, my ever best friend, who unfailingly accompanied me in this path of life.

I thank my family: Luigi, Marina, Antonio, Maria, for having always trusted me, supported my each life decision with confidence and respect, giving me the necessary serenity of mind to cope with such a great challenge.

Last but not least, with all my heart, I'd like to thank Vincenzo, my life partner, for loving me with care and constant support and for having made my personal challenges his own.

Francesca